An experimental investigation of the structural evolution of trans-critical fluid interfaces

Georgios Kasapis

A thesis presented for the degree of
Doctor of Philosophy

THE UNIVERSITY
of EDINBURGH

Institute of Multiscale Thermofluids
University of Edinburgh
United Kingdom
May 2, 2023

Declaration

I declare that the thesis has been composed by myself and that the work has not been submitted for any other degree or professional qualification. I confirm that the work submitted is my own, except where work which has formed part of jointly-authored publications has been included. My contribution and those of the other authors to this work have been explicitly indicated below. I confirm that appropriate credit has been given within this thesis where reference has been made to the work of others.

The work presented in section 1.2.2, sections 2.3.2 and 2.5.1, section 3.3 and Chapter 4 were previously published in Physics of Fluids as "A study of Novec 649$^{\mathrm{TM}}$ fluid jets injected into sub-, trans- and super-critical thermodynamic conditions using planar laser induced fluorescence and elastic light scattering diagnostics" by Georgios Kasapis (student and author of this declaration), Shangze Yang, Zachary Falgout and Mark Linne (supervisor of this thesis). This study was conceived by all of the authors. I carried out data curation, investigation, formal analysis, software development, data visualisation and supported experiment conceptualisation, methodology and validation.

The work presented in Chapter 5 was previously published in Experiments in Fluids, vol. 63, no. 8, p. 137 as "Reflectivity of diffuse, transcritical interfaces" by Shangze Yang, Georgios Kasapis (student and author of this declaration) and Mark Linne (supervisor of this thesis). This study was conceived by all of the authors. I carried out setting up the experiment and acquired the data.

KASAPIS Georgios	Date

Abstract

This thesis applies simultaneous laser diagnostics to steady, rotationally symmetric, laminar jets of fluoroketone injected into a high-pressure and high-temperature vessel with the goal to unambiguously identify interface transitions under trans-critical conditions, for the first time. The chamber was filled with nitrogen and the ambient thermodynamic conditions were varied from subcritical, to transcritical, to supercritical levels, relative to both the pure injectant and the binary mixture that ultimately developed in the chamber following injection. The laminar jet presents a clear interface that can be studied optically and its evolution was monitored under different test cases. Vapour-liquid equilibrium calculations for the binary mixture helped establish conditions that would identify the mixture as supercritical. This was necessary owing to the effect that mixing has on the critical properties of the mixture (relative to its constituents) and to design the test cases. Consistent with previous reports, it was found that the addition of nitrogen resulted in a rapid increase of the critical pressure of the mixture. The calculated phase envelopes reported here demonstrate the highly non-linear nature of mixing effects for the given binary mixture. Two main laser diagnostic techniques were employed: 1) Planar Laser Induced Fluorescence (PLIF) and 2) Planar Elastic Light Scattering (PELS). The former was used to obtain images of the mixture spatial distribution and the latter to monitor the strength of the interface. The diagnostics were applied simultaneously, thus allowing the comparison of interface strength and flow morphology at the same physical location and point in time. Using the average flow velocity at the nozzle, based on the known mass flowrate, and data from the elastic scattering signal, temporal estimates of the fluid interface destruction were calculated. Imaging results have shown that under all test cases a jet could be seen via PLIF, but a PELS signal was not always recorded. By knowing when a fluid interface was present or not, the PLIF images could be analysed in light of such information. Further, with the use of thermocouples 2-D temperature maps were obtained in the plane of injection. The temperature results presented further information about the heat transfer process of transcritical, laminar jets and, depending on the adopted definition of a supercritical fluid, indicated regions where the fluid was more likely to be supercritical. Cooling of the jet under the most demanding test case considered may have been an observation of pseudo-boiling effects (and their significance) due to injection near the Widom line. Investigation of intermittent, interface scattering observed even under supercritical cases revealed that the reflectivity of the fluid interface could potentially persist even beyond significant broadening of the interface. This meant that a decay of the interface scattering signal to zero would not necessarily coincide with the destruction of the interface, and some scattering could still be observed in supercritical cases where no interface is considered to be present. Magnified PLIF experiments were also done to obtain higher-fidelity images and density maps. These provided more information on fluid flow features and mixture distribution.

Lay Summary

In the project to be described, fluid jets injected into a chamber under very high pressures and temperatures were studied. Why was this of interest? To begin with, it is known that climate change is a serious threat to life on Earth and so reducing harmful emissions is, or at least should be, of high priority on the global agenda. Unfortunately, there exist some areas, such as shipping and aviation, that pose significant challenges when it comes to de-carbonisation. This means that it will take time, potentially on the order of many decades, before alternative, renewable means of powering these industries can be adopted on a commercial scale. In the meantime, any research that can help to improve the efficiency of Internal Combustion Engines (ICEs), widely used in the aforementioned industries, would contribute toward mitigating damage to the environment.

Modern engines operate at much higher pressures and temperatures than older versions of ICEs. This is because classical thermodynamics teaches that an ideal heat engine (e.g. Carnot cycle) can achieve a higher efficiency by increasing the highest temperature in the cycle. As operating pressures and temperatures have been rising, the ambient conditions into which fuel is injected in the combustion chamber have been nearing the thermodynamic critical point for some types of fuels found in industry. This is particularly common in rocket engines where fuels are generally simpler substances (e.g., liquid hydrogen). If the fuel exists in liquid form prior to injection (quite common since this exploits the higher density to store more fuel in less volume) it may potentially transition to a supercritical fluid state during the injection and mixing processes. A supercritical fluid is any fluid that exists above its critical point. This point is quite crucial (for reasons to be explained) and is typically given by a unique combination of one temperature and one pressure value. These values are substance-specific and constant. One of the main reasons this point is so crucial is because beyond this point surface tension, an important fluid property, is destroyed.

While surface tension exists the mixing between fuel and oxidiser in the combustion chamber is driven by atomisation (the fluid breaks into huge numbers of small droplets) and then evaporation (between each fuel droplet and surrounding gas). When surface tension ceases to exist there is no longer a fluid interface and so no evaporation occurs. The mixing mechanism changes and this is not as well understood as evaporation. It is therefore necessary to study such injections, known as transcritical injections, when the fluid may transition from subcritical to supercritical, and to develop theory and understanding of the underlying mechanics. This will in turn enable computational fluid dynamics and perhaps design engineers to improve the design of future engines (that are even more likely to experience such transitions) and help improve their efficiency even further. By doing so, harmful emissions can

potentially be reduced and the design of future engines with alternative fuels (such as hydrogen) can be better informed.

In this work, experiments were performed using simultaneous laser diagnostics on steady, laminar fluid jets injected into a high-pressure and high-temperature vessel. The aim of this work was to observe interface changes as the thermodynamic conditions were changed. Therefore, the chamber ambient thermodynamic conditions were varied from subcritical (low temperature and pressure) to supercritical (high temperature and pressure) levels. The laminar jet presented a clear interface that was studied optically. Planar Laser Induced Fluorescence (PLIF) and Planar Elastic Light Scattering (PELS) were the two main laser diagnostic techniques employed. PLIF was used to obtain images of the mixture distribution inside the body of the vessel, while PELS simultaneously monitored the strength of the interface. Further, 2-D temperature maps in the plane of injection were obtained and magnified. PLIF experiments were also done to acquire higher-fidelity images and density maps. As such a combination of diagnostics was used to obtain a holistic picture under conditions when there was no defined interface and provide insight into the process of transcritical injection. Finally, further investigation of intermittent scattering of light under (supercritical) cases when this was not expected, revealed that the reflectivity of the fluid interface could potentially persist even in supercritical cases.

Acknowledgements

I feel very fortunate to have been blessed with the support of many wonderful people during the past four years.

First and foremost, I would like to thank my supervisor, Professor Mark Linne, for all his teachings, insight and wisdom. Over the course of my PhD, Prof. Linne has been a continuous source of support and knowledge that have made this challenging path easier to walk. His calm approach to problem solving and positive outlook when encountering challenges have helped guide me through this journey. I am especially appreciative of his willingness to work hands on in the laboratory and to face problems together. The many stories he has shared from his own personal experiences have been very instructive and I have learned a lot from them. I consider myself lucky to have worked under the supervision of Prof. Linne and hope that we can collaborate on such interesting research topics in the future.

Secondly, I would like to thank postdoctoral researchers Dr. Zachary Falgout and Dr. Shangze Yang for all their help. Zachary designed and built the experimental setup used for this project, and allocated much of his time to educate me in its intricacies, so that I can take the lead upon his departure from the University of Edinburgh. Shangze's hard work in the lab helped us overcome some of the biggest obstacles we came across. The time he spent both in the lab working and in the office analysing and discussing was pivotal for the success of this project. Credit also goes to my second supervisor, Dr. Lars Christian Riis Johansen. Lars, on many occasions, offered technical expertise and advice in the lab. I am very thankful for his contribution and help during the course of this experimental campaign.

I am indebted to all the people working at the small research facility for sprays, especially Dr. Brian Peterson, Dr. Anthony Ojo and PhD students Yifan Liang and Hibbah Akhtar who offered their assistance many times and with whom I shared pleasant and interesting conversations. Special thanks go to Dr. David Escofet-Martin who, on numerous instances, invested part of his time to work with me on the experimental setup and for his eagerness to discuss issues and share ideas.

The help of Professor Piero Colonna from the Technical University of Delft, and Dr. Teus van der Stelt at Asimptote, in performing vapour-liquid equilibrium calculations and discussing experimental results is also greatly appreciated.

During this project I have received much needed support from many technicians at

the university, be it from the mechanical and electrical workshops or elsewhere. Their assistance helped make these experiments possible.

Finally, I would like to thank my family for their love, support and generosity. They have always been there for me to offer comforting words, advice or simply to listen. For this I am forever grateful.

Dedication

To my parents, Marios and Tatiana, whose love has been a beacon of hope during difficult times and to my late grandfather Georgios I. Kasapis, whose name I carry, who left this world for a better home during my PhD. Though he will not attend my graduation in body, I am sure he will in spirit.

Contents

List of Figures

List of Tables

Chapter 1

Introduction

The aim of the project presented in this report can be summarised as follows: Experiments were conducted to study the evolution of a fluid interface, and its breakdown, during the injection of two fluids (Nitrogen and fluoroketone) into a chamber where the ambient conditions exceeded the thermodynamic critical line of the mixture, potentially causing a transition to a super-critical state, with the goal to extract data, both qualitative and quantitative, that could then be leveraged by CFD engineers, with the ultimate goal to improve the efficiency of Internal Combustion Engines (ICEs) and limit harmful emissions to the environment.

The opening section of this chapter recognises and re-iterates the need to move away from fossil fuels and their combustion due to the adverse impact that this has on Earth's climate. However, it is then shown that there is a significant time requirement to the solution of power generation in heavy transport, such as aviation. Trans-critical fuel injection is identified as an area of combustion that will likely become more relevant in the future, as engine operating pressures and temperatures are pushed higher, in search for improved thermodynamic efficiency. Advancing the current knowledge and understanding of trans-critical injection is essential to enable such improvements. In light of this point, a brief review of relevant thermodynamics is subsequently given in an attempt to clarify what trans-critical injection is and under which conditions it occurs. A treatment of the relevant thermodynamics is given in Chapter 2. It is important to note that there is still uncertainty surrounding the subject and whether or not it actually occurs in certain types of engines. In rocket engines it is perhaps more clear that it does, as fuels similar to pure substances (or at least mixtures that are less complicated and with a lower number of constituents) are used. In other applications that make use of complex mixtures (e.g. diesel engines), however, there can be ambiguity [1]. A review of prior research conducted on trans-critical injection is given next, presenting key findings and discussing commonly used diagnostics.

1.1 Human induced climate change

It is by this point well established that human activities have a net negative effect on Earth's climate. The latest IPCC report [2] explains the causes of this problem clearly and is the go-to technical document for a description of the main climate change phenomena. A prominent factor driving climate change is the emission of waste gases such as carbon dioxide, that contribute to the greenhouse effect. They originate from various sources, such as combustion for power generation. This applies to virtually all ICEs used in road vehicles, shipping, electrical power stations and jet engines that burn hydrocarbon fuels. Electrification and renewable energy sources are two current global trends in technology that are being utilised to eliminate the world's dependence on fossil fuels and minimise harmful emissions. Unfortunately, unlike the automobile industry which seems to be making important strides towards becoming fully electric, these technological trends are not readily implemented in areas such as aviation, shipping, and space.

The aviation sector currently contributes about 2.4% of the world's CO_2 emissions, but its impact towards global warming is greater, at an approximate 4% [3]. Even though the aviation industry's contribution towards global warming is small in comparison to the rest of the transport sector, it is not negligible and must be addressed. According to a 2021 report published by the National Renewable Energy Laboratory of the U.S Department of Energy [4], the first commercial, fully electric aircraft that can transport up to 186 passengers (a significantly lower capacity than civil aircraft of today), is expected to join the market sometime between 2040-2050. Furthermore, a study [5] on the potential of electrifying the civil aviation sector has shown that achieving high payloads and long travel ranges on fully battery powered aircraft remains a challenge and the possibility of their implementation in the near future is limited. Energy density is a major issue. Conventionally powered planes grow lighter as they consume fuel, but battery powered ones have to carry their starting weight for the entirety of their journey. Reducing the amount of flights around the world is an option to limit emissions but stopping them all together is not. The reason is that transport by air is often the most practical solution and is typically the method of choice for very high-value products. Transport by air accounts for 35% of global shipments by value (not volume) [6]. It is also essential for time-critical transport, especially of perishables such as vaccines.

The challenges encountered in aviation are similar to those in marine shipping and together these two industries form arguably the greatest obstacle in de-carbonising the transport sector [7]. Similar to aircraft, cargo ships do not have the luxury of frequent refuelling and must carry more than enough fuel for their journey. The CMA CGM Benjamin Franklin, a large cargo ship, could complete a typical journey on 33 million pounds of conventional fuel, but would need a 1.6 billion pound battery equivalent to go electric [8]. This is true because batteries cannot match the energy density of conventional liquid hydrocarbon based fuels. The weight requirement is too high and batteries are, therefore, not a viable solution currently. It is easy to see how the issue of weight extends to the space industry as well, with immense power requirements at lift off. With an emphasis on weight optimisation going into the design of space shuttles to allow them to reach orbit, it is difficult to imagine them being powered by batteries any time soon.

The heavy transport problem will not be solved quickly; it will likely take several decades. In the meantime, commercial aircraft and ocean vessels will continue to generate emissions. It is then necessary to advance gas turbine and marine engine efficiency and, in doing so, limit damage to the environment as much as possible. The

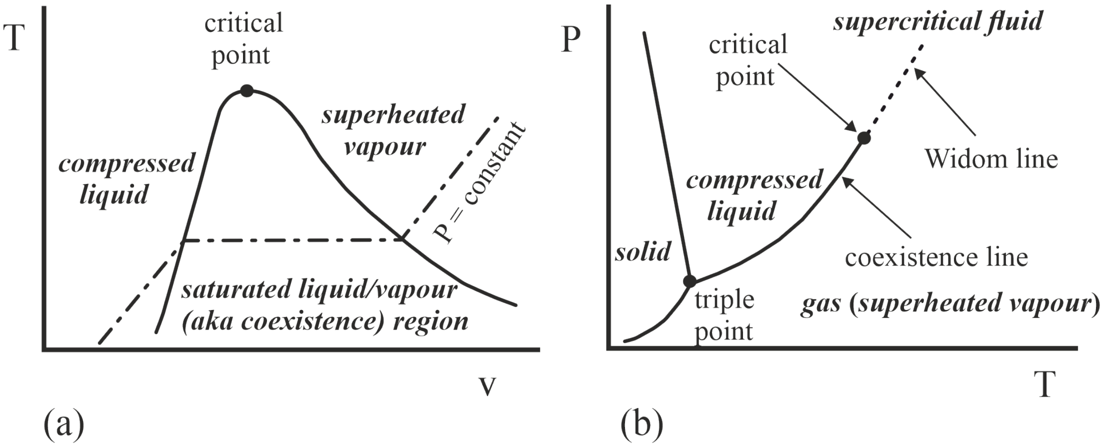

Figure 1.1: Thermodynamic diagrams for a pure substance (a) Temperature against specific volume (b) Pressure against temperature

challenge is that most combustion engines are already significantly more efficient than when they were first introduced. The Trent XWB is one of the latest iterations of the Trent family of jet engines by Rolls Royce and it is already 15% more fuel efficient than the original Trent engine [9]. With the 'low hanging fruit' having already been collected, identifying potential room for improvement becomes a challenge in and of itself. By going to higher operating pressures, trans-critical jets are likely to become more commonplace in combustion engines. Consequently, there will be challenges in designing engines that may have to cope with different mixing mechanisms between fuel and oxidiser due to trans-critical phenomena. The work presented here attempts to improve the current understanding of such aspects of high-pressure jets and a review of relevant, prior work is given in the following sections.

1.2 Transcritical injection: Review of previous work

1.2.1 Brief overview of supercritical fluids and relevant concepts

In this section, a short description of supercritical fluids is given in preparation for the upcoming discussion of relevant literature. A more expanded review of supercritical thermodynamics is given in the following chapter.

Figure 1.1 depicts thermodynamic diagrams (Temperature-specific volume, $T-v$, and pressure-temperature, $P-T$) for a pure substance. Any pure substance can exist as a solid, liquid or gas. In the $P-T$ diagram (Figure 1.1 (b)), the compressed liquid and superheated vapour regions are separated by the coexistence line. This line connects all of the thermodynamic states where a pure substance exists as two phases, liquid and vapour, in equilibrium. It terminates at the critical point where the liquid and vapour states become identical. This point is generally given in terms of a critical temperature, T_c, and a critical pressure, P_c, and is unique for each pure substance. The $T-v$ diagram in Figure 1.1 (a) contains the well-known vapour dome, wherein liquid and vapour can coexist. The critical point is seen as an inflexion point on the

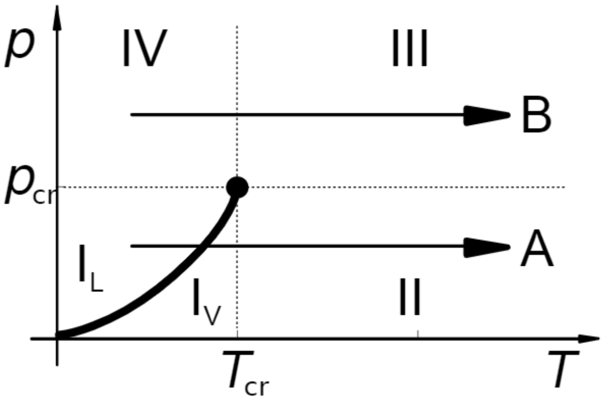

Figure 1.2: Four-quadrant portrayal of the fluid state space. [10]

$T-v$ diagram. To its left is the saturated liquid and to its right the saturated vapour line. On a $P-T$ diagram these two separate lines converge to the same (coexistence) line; the coexistence line depicts the vapour dome from the side.

At the critical point, a substance's physical properties exhibit significant changes. The latent heat of vaporisation becomes null and so does the surface tension. On the other hand the heat capacity becomes infinite and so does the thermal conductivity. Density can be subjected to large gradients near the critical point and critical opalescence may be observed, a phenomenon that makes a substance appear milky due to changes in its optical properties at the critical point. Furthermore, supercritical states, i.e. states that exist above the critical point, are characterised by higher diffusion rates and higher solubility. In fact, this is partly why supercritical CO_2 has been successfully applied commercially for decaffeinating coffee, tea and for the extraction of essential oils.

Here it should be noted that there are differences in opinion when it comes to defining the conditions for a fluid to be considered supercritical. Perhaps the most commonly cited requirements (for a pure substance) is that the fluid should be brought to a state that has both a pressure and temperature that are above the respective critical values. However, as Banuti [10] points out, different authors have adopted different conventions. Figure 1.2 shows the four quadrants typically identified on a pure substance's thermodynamic state diagram. According to Banuti, authors have chosen different combinations of quadrants to indicate when a substance is supercritical including: 1) II,III and IV, 2) II and III, 3) III with IV considered transcritical. Thus, there is still an ongoing debate on what the most appropriate set of requirements is.

On the $P-T$ diagram (Figure 1.1 (b)) a line can be seen extending from the critical point as a continuation of the coexistence line. This is known as the Widom or pseudoboiling line, typically constructed by connecting maxima of the isobaric specific heat capacity at supercritical pressures. Whereas the coexistence line separates liquid and gas states, the Widom line separates liquid-like and gas-like states. A phase change that crosses the coexistence line involves vapour-liquid equilibrium. Crossing the Widom line does not generate two phases but it does result in observable changes in physical properties. Because of its similarities to a sub-critical phase change, going from a liquid-like to a gas-like state by crossing the Widom line has been dubbed as a “pseudoboiling” process.

It is clear that a substance’s physical behaviour, e.g. the mechanism by which it mixes with other substances, may change fundamentally, if its thermodynamic state crosses a threshold such as the critical point or Widom line. Due to trends in the design of modern engines, it is possible for such a change in physical behaviour to occur during operation. Hence, it is important to understand such changes to be able to characterise, predict and better inform the design of future engines.

1.2.2 High pressure fuel injection

Manufacturers have been developing engines that operate at high combustion chamber pressures and temperatures, generating high efficiency levels and hence low CO_2 emissions. Modern gas turbines can operate with chamber pressures from 20 - 60 bar, while Diesel engine chambers can span from 10 - 50 bar. Some of these conditions are above the critical point for some fuels, and a subcritical fuel jet could potentially become transcritical once injected. A genuinely supercritical jet in a high-pressure and high-temperature background gas has no surface tension. Evaporation from a subcritical interface is replaced by diffusion through a distributed, supercritical mixing region. Under supercritical conditions, therefore, no drops are formed and the fuel jet entrains the surrounding gas more like a dense gas jet.

To add complication, a mixture of compounds will have entirely different critical points (pressure P_c and temperature T_c) than each of the pure substances that form the mixture. The mixture critical point depends on the mixture fractions, and it is not straightforward to estimate, especially if more than two components are present. Fossil fuels have many components and in the main, they may not become supercritical, but planned alternative fuels are similar to single-component fuels, many of them with low critical points, and they are more likely to transition [11]. Moreover, the term “supercritical” denotes an equilibrium state, which may not be reached within the available mixing time in an engine [12, 13]. This thermodynamic transition would thus proceed in parallel with mixture formation and combustion.

Supercritical injection is known to occur in rocket motors, where it has been the subject of investigation for some time [13–15]. That case is somewhat more tractable, however, because a pure fluid (e.g. hydrogen) is injected into another pure fluid (e.g. oxygen), with at least one of them already in a supercritical state. This is an important simplification both experimentally and with regard to analysing the acquired data. Because of this simplification, and because of their applicability in the space sector, many early studies published on the topic of transcritical injection concerned themselves with rocket engines and the injection of fuel under relevant conditions. Overall, there have been many injection studies into high pressure and temperature environments over the past 50 years. A review of some of the most important of these will be helpful to contextualise the work presented in this thesis.

1.2.3 1970-2006: Early work

Much of the work done on fluid injection into high pressure environments, in the period up to 2006, was conducted by two research institutions: the German Aerospace

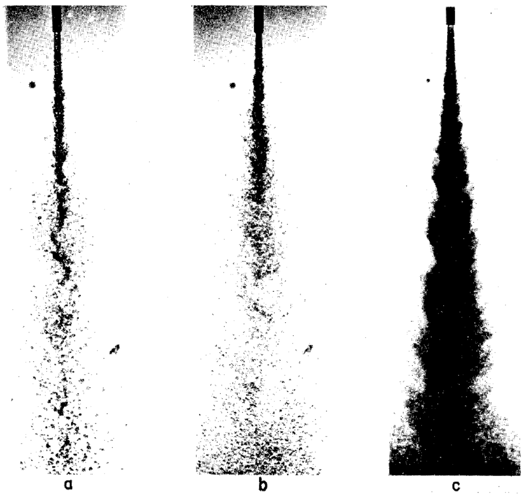

Figure 1.3: Influence of gas composition on jet behaviour (injection velocity = $370\,\mathrm{cm/s}$, chamber pressure = $1100\,\mathrm{psig}$ ($76\,\mathrm{bar-g}$), environmental temperature = $22\,^{\circ}\mathrm{C}$, partial pressure of CO_2 = a) $0\,\mathrm{psi}$ b) $550\,\mathrm{psig}$ ($38\,\mathrm{bar-g}$), $900\,\mathrm{psig}$ ($62\,\mathrm{bar-g}$) [17]

Centre (DLR) and the Air Force Research Laboratory (AFRL) in the USA. According to the 2006 review paper by Oschwald [16] that compared results obtained by these bodies independently, the two most commonly used diagnostics up to that point were shadowgraphy and spontaneous Raman scattering. This was the case for studies by other researchers as well. Shadowgraphy proved to be a reliable and useful technique for visualising large scale changes to the overall fluid field and qualitatively analysing jet injection, both with and without a co-flow. Raman scattering was used in an effort to extract quantitative information, such as to obtain a density map of the jet and surrounding mixing layer from which temperature could then be calculated via the application of a suitable equation of state.

Possibly the earliest study that used shadowgraphy to investigate a liquid jet injected into a chamber where the thermodynamic conditions were close to or exceeded the critical properties of the pure fluid was published in 1971 by Newman and Brzustowski [17]. Using a high-pressure chamber with optical windows and embedded cartridge heaters they investigated the injection of turbulent, liquid carbon dioxide jets into a vapour environment that consisted of CO_2/N_2 mixtures at various compositions. Using back-lighting, they obtained photographs that allowed visualisation of the jet and enabled comparisons to be made between the observed structures under different injection conditions. They investigated the effects of increasing the chamber pressure from sub- to near- to supercritical levels while keeping the chamber temperature at a supercritical level and vice versa.

Newman and Brzustowski observed significant morphological differences as they changed conditions. For example, droplet sizes and jet core length changed as they varied the chamber pressure. The droplet size generally decreased at higher chamber pressures (higher gas-to-liquid density ratio) and a shortening of the main jet was observed at supercritical conditions. Note that supercritical conditions were defined in terms of the pure fluid being injected (mixture effects on the critical point were not considered). Perhaps the most striking change was seen by varying the ambient composition, reported in terms of partial pressure of CO_2. A selection of images is shown in Figure 1.3. Going from sub-figure 'a' to 'c', the partial pressure, and hence gas composition, of CO_2 in the chamber is increased at constant chamber pressure and temperature. The trend is towards a finer gaseous spray, with a significantly larger spreading angle. The experimental results of this study are valuable as they demonstrate the impact that high pressures and temperatures can have on fluid jets. The experimental data of this early study come with certain limitations: no quantitative data were obtained and the spatial resolution of the imaging system did not allow fine details to be easily observed.

Supercritical injection studies were not common in the time period 1971-1990. The next major studies were both published as reports by the US Defence Technical Information Centres. In 1992, Birk et al [18] investigated high velocity ($100 - 240$ m/s), reacting monopropellant sprays being injected via circular orifices (typically 0.5 mm diameter) into nitrogen. The injectants were in a liquid state prior to injection, and several different working fluids were considered, including water, ethanol and nitromethane. The nominal chamber conditions were 500 °C and 33 MPa, although for the water spray studies an exception was made with one experiment being conducted at room temperature. Overall, the chamber conditions were at least moderately, and in some cases significantly, above the pure component critical properties.

They collected spectroscopic data from the flame emission created under some of the flow test cases (many of them were seeded to enhance flame luminosity), together with gas temperatures and chamber pressures at timescales relevant to flame propagation (approximately 2 s). For flow visualisation, both high-speed cinematography and colour video were obtained using a 10 W copper vapour laser as a strobe. With regard to the water sprays, even at the highest chamber conditions, atomisation persisted, with large water droplets forming following injection. However, for the cases of nitro-methane and ethanol the authors reported that no droplets could be seen in the images. The critical properties of these two substances, 315°C , 6.3 MPa and 243°C, 6.4 MPa respectively, were significantly lower than the ambient nitrogen state, more so than for the water jets.

In the review article by Bellan [14], the author points out that no explanation on the difference of behaviour is given in the report by Birk et al. Although this cannot serve as a definite explanation, it should be noted here that Vapour Liquid Equilibrium (VLE) calculations presented later on in this thesis have shown that the addition of nitrogen to different types of substances can potentially have a serious impact on the critical properties of a mixture. Given that all three jets considered above were injected into nitrogen, this may explain, or be one potential factor to explain why, atomisation was observed in water sprays but not in nitro-methane and ethanol. The water-nitrogen mixture might in fact be characterised by much higher critical properties.

The next study by Birk et al [19], published in 1995, aimed at further investigating the jet core, with the hope of resolving its internal structure. Flash X-ray experiments and light scattering in the visible range, recorded with an intensified-CCD camera, were used to image the jet. Both full cone and annular jets were studied and the working fluid chosen was methyl iodide, owing to its favourable critical properties

($P_c = 7.366\,\mathrm{MPa}$ and $T_c = 528\,\mathrm{K}$), which could be exceeded experimentally, and its high X-ray absorption cross-section. In this study, the chamber thermodynamic conditions were controlled using two different methods. The first method fed high-pressure nitrogen from a reservoir to the chamber, whilst the other involved injecting into post-combustion products of Hydrogen/Air/Argon mixtures. They concluded that the jet core is not well defined but instead consists of a region of high liquid-to-vapour volumetric concentration.

Density distribution measurements via Raman scattering published later (e.g., [20]) supported this finding and in fact showed that under certain conditions a drop in density could be observed as soon as the jet entered the chamber. These results established the absence of a dense potential core that Banuti [21] explained by introducing a thermal disintegration mechanism. This explanation was necessary as the mechanical break-up mechanism of jets under shear forces could not be used to explain the density distribution already seen upon exit from the nozzle.

Birk et al. [19] further established that the structure of the core changes substantially when comparing evaporating and non-evaporating sprays. The term 'evaporating' was used to refer to chamber conditions that were supercritical compared to pure methyl iodide and the applicability of the term is debatable. Part of the problem is that the range of vapour-liquid equilibrium across all possible concentrations is not known; therefore, it is unclear whether the mixture would have in fact been supercritical or not. Nonetheless, consistent with observations in the ethanol jets of the previous study, helical instabilities were observed to develop downstream for the case of the full cone jets. According to their results, the length of the jet core when it finally transitions to a helical structure decreases with ambient gas pressure and density. However, the core penetration reached a minimum length at some pressure level (which may or may not have been a critical pressure of the mixture), and then increased with higher pressure. A possible explanation given was that the core temperature obtained its critical value near the orifice, which in turn slowed the process of atomisation, potentially generating a greater jet core break-up length.

A commonly cited set of experiments that further contributed to this field was performed by Mayer et al. [22, 23]. They conducted experiments using cryogenic injectants, such as liquid oxygen or nitrogen, into a pressurised chamber. In those experiments they investigated a variety of configurations including:

- Injection of a fluid jet with and without a co-flow
- Injection of a fluid jet into its own vapour and into other gases
- Injection into sub-critical and super-critical pressures

Both studies attempted to establish the effect of pressure on the mixing characteristics between fuel and ambient gas under realistic rocket engine conditions through flow visualisation. Their data were obtained via single-frame imaging, schlieren imaging and high-speed cinematography. Their observations revealed mechanistic changes in the way the injectant mixed with the surroundings as the chamber ambient conditions were varied from sub- to super-critical conditions (for conditions relative to the pure injectant). The classical spray formation regime was no longer valid at very high

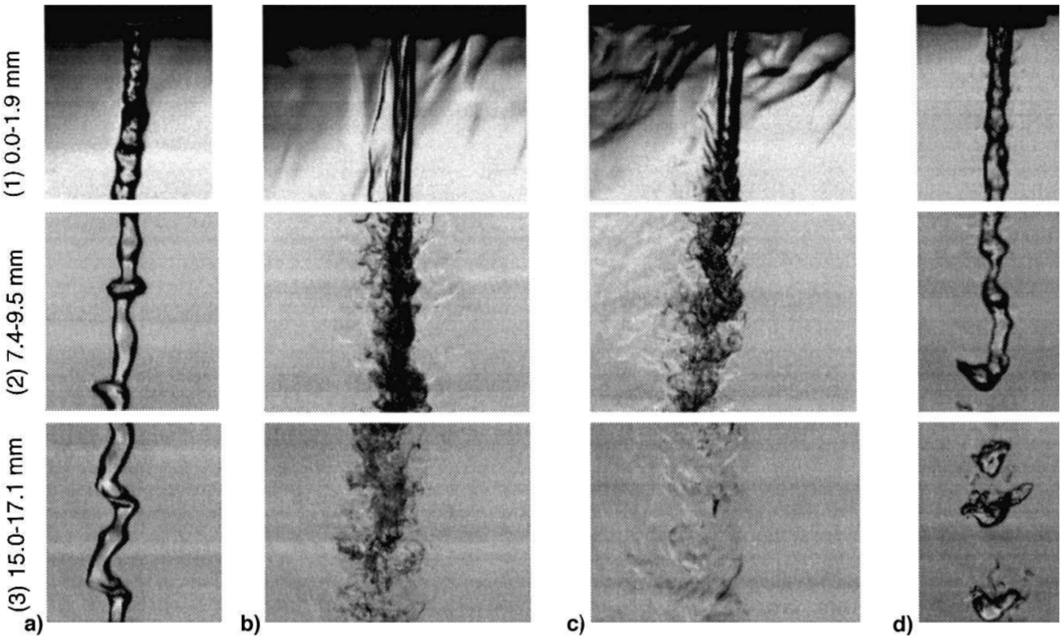

Figure 1.4: Subscale LN_2 injection into a pressurised chamber. Horizontal rows correspond to distance from the injector tip. Vertical columns correspond to different experimental conditions as follows: a) Into subcritical N_2 at 2.8 MPa, $p/p_{crit} = 0.83$; b) into near critical N_2 at 3.5 MPa, $p/p_{crit} = 1.03$; c) into supercritical N_2 at 6.9 MPa, $p/p_{crit} = 2.03$; and d) into a $N_2/O_2 = 3.9$ mixture at 6.9 MPa, $p/p_{crit} = 2.03$. [taken from [23]]

pressures and was instead substituted by a diffusive gas-like mixing process. Many of the test cases in the experiments by Mayer et al. attempted to re-create realistic operating conditions of a rocket engine, typically resulting in a turbulent flow due to high injection velocities of the fluids involved. For fluid interface studies, however, such demanding conditions can obscure finer details. Hence, a subscale study was also done with much lower velocities (aiming towards a laminar jet) as well as a smaller injector diameter. Images from this study are shown in Figure 1.4.

Sub-figures 'a-c' in Figure 1.4 depict liquid nitrogen injected into its own vapour. At subcritical pressure the injectant develops surface waves a short distance past the injector. Further downstream, these instabilities are amplified, with the main body of the jet exhibiting somewhat sinuous motion. Nevertheless, the jet remained intact. In contrast, nearing the critical pressure, and then exceeding it, caused the structure of the flow to transition into a form that resembled a gaseous jet instead of a column of liquid. Interestingly, the sheets of fluid seen propagating near the nozzle (owing to a manufacturing imperfection) in sub-figures 'b' and 'c', can be attributed to a diminishing surface tension force. They cannot, however, be used to precisely locate its destruction.

The results clearly demonstrate the effect of pressure on the fluid structure, and consequently on the mixing mechanism. An interesting finding is illustrated by sub-figure 'd', which is for liquid nitrogen injected into a mixture, rather than its own vapour. There is a discrepancy regarding the nature of this mixture in the paper between the figure caption and the description provided in the main body. The former says oxygen was added and the latter says it was helium. Whatever the case was, the images clearly demonstrate that mixing effects had a profound impact on the fluid state and mixing mechanism as surface tension effects made a return (this topic is explored in more detail in Chapter 2 where vapour-liquid equilibrium of mixtures is discussed). Further experimentation showed that pressure had to be increased to a level significantly above the pure component critical pressure for surface tension to vanish again.

It is common practise today to report on trans-critical studies using 'reduced' quantities, i.e. dividing various properties by their corresponding critical value that is specific to the given substance. This is good practise for studies where only one substance is involved and it is certainly not erroneous in mixture studies either. If the way in which a reduced property is calculated is clear, there is no issue; it is simply a way of reporting it. What can be misleading, however, is the notion that because the chamber pressure and temperature are above the critical properties of the **pure** fluid being injected, that the mixture is supercritical. This ignores mixing effects that can cause the critical point of a mixture to differ significantly from either of its constituents. In Chapter 2, it is shown that this variation can be highly non-linear. Hence, it should be noted that the reported reduced pressure of 2.03 for sub-figure 'd' is relative to the pure nitrogen critical pressure and not of the mixture in the chamber.

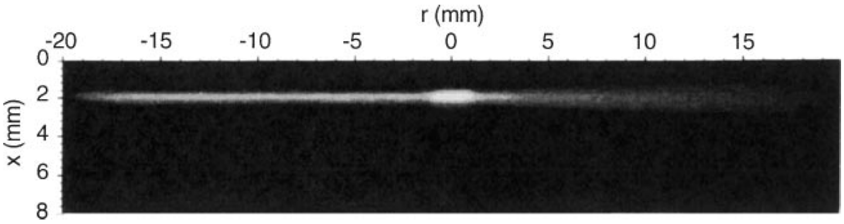

Figure 1.5: Example Raman signal from [24]

Oschwald and Schik [24] studied cryogenic nitrogen jets (without co-flow) via Raman scattering, applied in 1D. They measured density along lines perpendicular to the jet axis (an example is shown in Figure 1.5) and then offset the measurement location along the jet centre-line. Through the application of an equation of state they could convert the density profiles to temperature. Figure 1.6 shows the normalised peak density for each radial profile at each axial location and for the low pressure cases (this refers to the ambient pressure and was still supercritical at $4\,$MPa with a reduced pressure of 1.17). Based on their measurements they concluded that, all other things being constant, a lower injection temperature leads to longer dense core penetration. This is consistent with the findings of this thesis and can be seen for supercritical pressure (relative to the pure fluid) by comparing Planar Laser Induced Fluorescence (PLIF) images from test cases 5 and 6 (Figures 4.7 and 4.8) and for subcritical pressure by comparing PLIF images from test cases 1 and 2 (Figures 4.3 and 4.4).

The difference in density profiles was less pronounced in the higher pressure test cases done at $6\,$MPa, dubbed A6, B6, and C6, where all other experimental variables were unchanged from the low pressure cases. This may be explained by the higher reduced pressure and by noting that the injection temperatures are fairly close to the

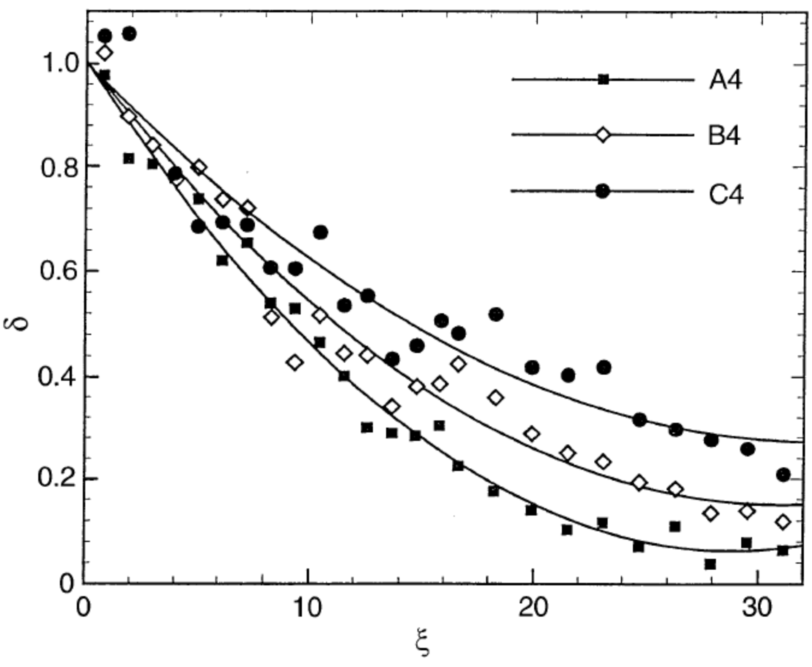

Figure 1.6: Normalised maximum of the density profiles for the 4 MPa cases. The term δ represents the normalised density and ξ is the distance from the injector normalised by the nozzle diameter. Injection temperatures are 140 K, 118 K and 100 K for cases A4, B4 and C4, respectively [24].

pseudo-boiling line. As Banuti [25] demonstrated, the non-linear effects of crossing the pseudo-boiling line decrease in magnitude as the substance is brought to higher reduced pressures (eventually becoming negligible beyond a reduced pressure of 3). However, it should be noted that the injection temperature in the Raman scattering study by Oschwald and Schik was measured 20 mm upstream of the injector and the fluid feed line did not have active temperature control. This lack of control could have introduced a ΔT error to the true injection temperature. During this thesis work, this temperature error was found to be significant and warranted a calibration process, something done by other studies as well (e.g., Figure 4 in [20]). Additionally, when close to the pseudo-boiling line, heat transfer in the injector can generate large changes in density, and hence errors, due to the non-linear response of density to a temperature rise [21].

Chehroudi et al. [26] further contributed to the literature of transcritical flows with a set of experiments published a few years later. Both nitrogen and oxygen were injected into a chamber that was filled with various fluids. In the case of nitrogen, it was injected in a liquid state into a chamber filled with gaseous nitrogen at 300 K (above the critical temperature, $T_c(N_2) = 126.2$ K). The chamber temperature was kept constant but the chamber pressure was varied from well below the critical pressure to well above it. Shadowgraphy was employed to observe morphological changes in the jet as conditions were varied. As the pressure was scanned from low to high, what started as a typical turbulent spray transitioned into a dense gas jet as the chamber went above the critical pressure. Images published in that study demonstrated similar

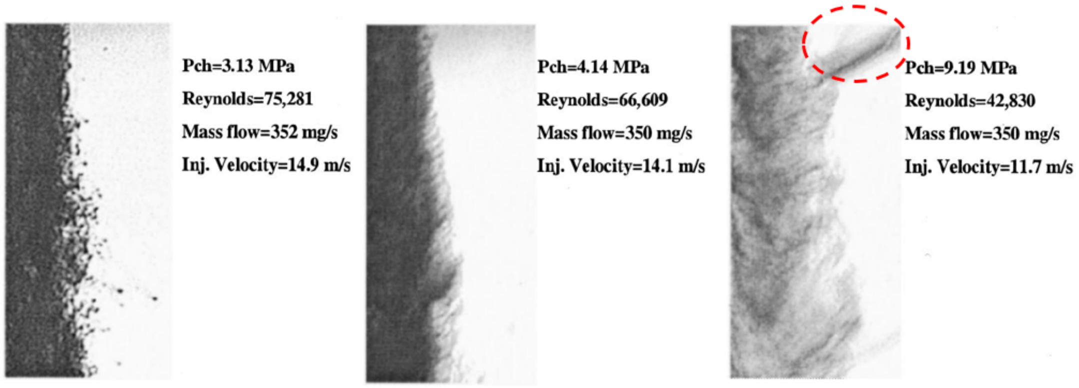

Figure 1.7: Software magnified images of the jet at its outer boundary showing the transition to the gas-jet-like appearance, starting at just below the critical pressure of the injectant. Images are at a fixed supercritical chamber temperature of 300K. The red circle indicates a sheet of fluid travelling away from the jet core, caused by a weakening of surface tension [26]

structural changes as the ones reported by Mayer et al. Figure 1.7 is a selection of relevant, magnified images that clearly demonstrate the move away from classical spray atomisation towards gas-like mixing as the chamber is made to exceed the critical pressure.

Interestingly, though no remark is made in the paper, in the high-pressure shadowgrams a sheet of fluid (indicated by the red circle in Figure 1.7) can be seen emanating near the nozzle, in line with what was observed in the injection experiments by Mayer et al.[23]. These sheets could often be an indication of weakening surface tension. Chehroudi et al. go beyond discussing morphological changes qualitatively and attempt to characterise changes in the jet growth rate. Furthermore, they discuss the transitions between the various regimes of atomisation as the chamber pressure is varied. A conclusion was reached that attributed the ‘suppression’ of the full atomisation regime (the fluid begins to assume a gas-like state instead of entering this regime) to the disappearance of surface tension and its associated property of latent heat. It is important to mention that in that study only turbulent jets were considered, with Reynolds numbers in the range of $25,000 - 75,000$.

In 2003, Mayer et al. [20] published a combined experimental and computational study. They performed Raman measurements on a cryogenic nitrogen jet (2.2 mm diameter) into its own vapour to extract quantitative data in the form of jet spreading angles and density. They complemented these findings with results from modelling the jet, and built on the work of Oschwald [24] by applying a 2D Raman scattering diagnostic. This time, a careful calibration process of the injection temperature was conducted in a separate experimental campaign. They noted that the only active temperature control in the cryogenic jet delivery system was installed at the storage tank, which is why heat transfer to the jet inside the feed-line raised its temperature. Radial density results, normalised by the centre-line density value at the injector, are shown in Figure 1.8.

Some of the test cases indicated a dense potential core at injection. In many others, however, there was a complete absence of such a core and instead the density

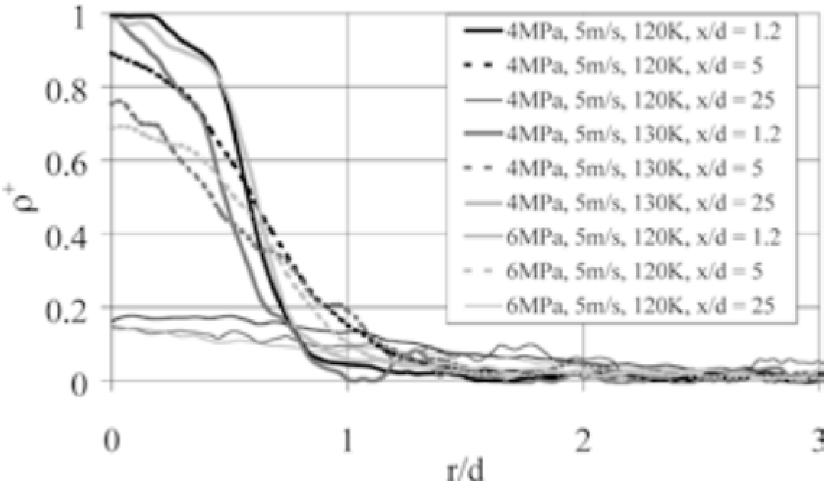

Figure 1.8: Density measurements radially of the jet centre-line at various axial locations, for test cases 3,4 and 11 [20]

was observed to drop immediately following injection. Banuti [21] analysed the data by Mayer et al. and proposed a thermal disintegration mechanism that could explain the absence of a dense potential core at injection. This mechanism is initiated by approaching and crossing the Widom line (pseudoboiling line) and could take place within the fluid delivery tube, if heat transfer took place there. The analogous, averaged density measurements of this thesis, presented in Figure 4.11, show a dense potential core close to the nozzle for all cases, even at injection conditions close to the Widom line (test case 6). Despite the data near the nozzle being adversely affected by laser sheet absorption (this is discussed in more detail in Section 3.3.2), the jets appeared dense in all cases at the edge, before absorption effects became noticeable. Density was modelled using super-Gaussian profiles (also discussed in Section 3.3.2) and it is the fitted models that are presented in Figure 4.11, which are idealised and hence show a perfect potential core near the nozzle. It should be noted, however, that the jet velocities and diameter were significantly higher in [20] than for the test cases considered in the work described here. Furthermore, there was no active temperature control in the feed-line used by Mayer et al., in contrast to the experiments reported in this thesis. Thermal disintegration depends on heat transfer across the fluid feed-line which may have been more significant in [20] than in the experiments reported here.

1.2.4 Limitations

Shadowgraphy

Shadowgraphy has been challenged as an inappropriate technique for the study of a trans-critical interface. The argument made by Harstad and Bellan [27] is that the diffusive mixing region that replaces the much thinner (by comparison) fluid interface once surface tension is lost, still exists at a length scale that is much smaller than the spatial resolution of an imaging system. A recent study by Lamanna et al. [28] cited a number of problems with regard to high resolution shadowgraphy and in general supported the assertion of Harstad and Bellan. The latter argued further that the change of the index of refraction through the diffusive mixing layer could generate a shadowgram image that would appear similar to an intact fluid interface.

Raman scattering

The Raman scattering signal can be low in intensity which poses experimental challenges. It is possible to increase the exposure time to accumulate signal and improve its ratio to background noise but this prevents resolving the flow in the time domain. In addition, it was reported [16, 20] that Raman measurements can suffer from stimulated and plasma emission. Since these are more prominent in subcritical jets, Raman measurements were found to be most useful in supercritical jets.

It should also be noted that measurements of the same quantities, in particular jet spreading angle and length of dense potential core, reported via these two diagnostics have suffered from non-negligible differences. For example, the jet spreading angle measured through shadowgraphy would only be in agreement with the Raman scattering results when the jet width measured by Raman was defined to be twice the full-width at half-maximum (from density measurements) [16]. However, this method of achieving agreement between the measurements was not found to be universal.

Despite the limitations of these techniques, they have been, and still are, valuable tools for flow visualisation and analysis. Nevertheless, recent studies have expanded their approach to include additional diagnostics such as laser induced fluorescence (for molecules that do fluoresce) and elastic scattering.

1.2.5 2006-2022: Recent studies and advancements

As mentioned previously, many of the early studies focused on rocket engines. The simpler mixtures they considered helped to eliminate certain challenges, such as complicated mixture phase diagrams caused by the presence of many components, together with difficult to achieve critical conditions. Recent studies have included situations involving more complex liquids, like hydrocarbons, that are less straightforward especially under conditions relevant to engines (e.g., Diesel). In recent years, fluoroketone has been chosen as a fuel surrogate by various research groups. Examples of research utilising fluoroketone can be found in [29–31] and the work completed during this thesis [32, 33]. To explain this trend, some information about fluoroketone as a substance is given in the following paragraph, with Chapter 2 providing further details about its thermodynamics.

Even though fluoroketone is not a hydrocarbon, it has the advantage of low critical properties ($P_c = 18.8$ bar and $T_c = 169\,^{\circ}$C in pure form) that are favourable for fundamental studies of thermodynamic interface transitions. Its high fluorescence yield simplifies the application of PLIF by eliminating the need for a tracer and related, potential complications with regard to VLE estimations and alterations of the flow dynamics. Fluoroketone is chemically stable and will not pyrolyse while under study like most hydrocarbons. This is important as pyrolysis creates a mix of species that would then alter the critical properties of the injectant and resulting mixture. Furthermore, fluoroketone is a suitable thermodynamic surrogate because it has similar characteristics to the light ends of hydrocarbon fuels and potential alternative fuels. Many fuels from both of these categories are more susceptible to thermodynamic transition due to their lower critical properties. It should also be noted that fluoroketone, with the exception of posing a threat to aquatic life if not disposed of responsibly, is harmless and safe to work with. Unfortunately, its molecules are complex and therefore difficult to model in molecular dynamics simulations.

A research group at the University of Florida studied jets of fluoroketone issuing into high pressure and temperature nitrogen. They used PLIF to image the jet for test cases that varied from fully sub-critical to fully super-critical. From the relationship between the fluorescence signal and number density they were able to obtain mass density and density gradient maps [29, 34]. They also performed experiments combining PLIF with shadowgraphy [35]. According to that study, both diagnostics agreed on most morphological aspects, such as the presence of surface instabilities, and mechanistic changes, e.g. transition to gas-gas mixing upon achieving a supercritical state. There was discrepancy, however, in the measurement of the jet spreading rate when compared with previous studies. This was attributed by the authors to the fact that the imaging techniques were different; the shadowgraphy signal is integrated over the entire jet whereas the PLIF signal is obtained from a single plane (slice) across it.

Following those studies, DeSouza and Segal [36] obtained further quantitative results and investigated the impact that the momentum and velocity ratio (between flow and co-flow) had on the jet core length, break-up mechanism, and spreading angle. The results achieved by these studies are significant for various reasons. They are an addition of quantitative data under challenging thermodynamic conditions of interest, which are uncommon in this field of research. Additionally, they report on the spectroscopic properties of a commercially available fluoroketone [37, 38] which facilitates research by other groups.

Dahms and co-workers [39] experimented with n-dodecane jets injected at engine-relevant conditions into vitiated air. They subsequently studied various binary mixtures, such as n-dodecane with nitrogen [40] and n-decane with hydrogen [41], primarily through modelling. In all these studies, an equation of state and VLE calculations were used to locate thermodynamic states and phase co-existence conditions for the binary mixtures of interest. Linear gradient theory was then applied to model the internal structure of the gas-liquid interface and report classical, two-phase interface thickness estimates. Moreover, in their experimental study [39], they imaged the jets via long distance microscopy to confirm that the flow structure was indeed fundamentally different under the two test cases considered (one at low temperature and one at high temperature). From their results they speculated that in modern diesel engines a supercritical, dense fluid mixing layer no thicker than 30 nm would replace the liquid-gas interface across which fuel evaporates. The interface thickness under the two test cases considered in that study are shown in Figure 1.9.

The Knudsen number, denoted Kn, is given by λ/L, and was defined using the interface thickness as the characteristic distance, L, with λ in this context being the mean free path of molecules. In later work [42], a general, non-linear gradient theory was developed to model the structure of the fluid interface with increased fidelity. Additionally, a Knudsen number criterion was derived to predict when temperature gradients would penetrate into the interface. Classical, two-phase interfaces are typically thought of as being infinitely thin and isothermal (i.e. no temperature gradient

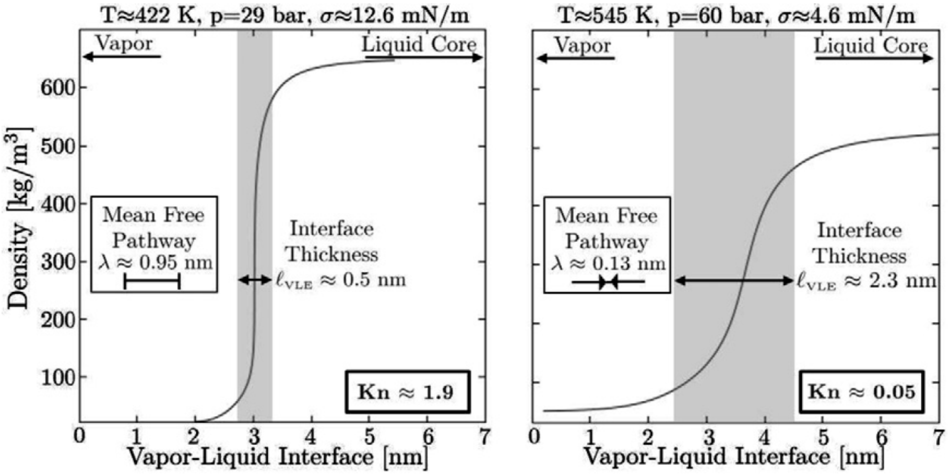

Figure 1.9: Vapour–liquid interface density profiles and thicknesses for the low-temperature (left) and high-temperature (right) interface states, calculated using Linear Gradient Theory. Corresponding mean free pathways λ are shown for reference. According to the applied Knudsen-number criterion, the high-temperature interface falls within fluid mechanic continuum length scales ($Kn < 0.1$) [39].

across the interface). It is interesting to note that the calculated broadening of the interface by a factor of nearly 4.6 is accompanied by a more gradual drop (factor of about 2.7) in surface tension. Analysis of results obtained in this thesis, to be discussed in more detail in Chapter 5, suggested that a similar trend may potentially be observed in the reflectivity of the fluid interface. The analysis indicated that the broadening of a fluid interface is followed by a gradual drop, and not a spontaneous destruction, of the reflective properties of the interface. While these two trends cannot be directly correlated in the context of this report, they nevertheless offer some insight into the mechanisms of interface destruction under engine-relevant conditions.

Developing greater insight into the structure of the fluid interface is needed to better understand the mechanics of thermodynamic transition. To date however, there have been no experimental observations probing the internal structure of a trans-critical interface during injection under engine-relevant conditions. Nevertheless, the research community has found ways to monitor other quantities that allow for an implicit study of such interfaces. It is possible, for example, to observe macroscopic phenomena whose origins can be linked back to the existence of an interface. Muthukumaran and Vaidyanathan [43, 44] were able to monitor axis switching of an elliptical fluoroketone jet because that process is a function of surface tension. Once the critical point is exceeded and transition takes place, surface tension disappears and so axis switching will cease. In the experiments reported here, the macroscopic phenomenon that was monitored was interface scattering. Elastic scattering is linked to the existence of an interface and is orders of magnitude stronger than other processes that scatter light, such as Rayleigh scattering. In a subsequent study [30], Muthukumaran and Vaidyanathan investigated round liquid jets using shadowgraphy and performed stability analyses to demonstrate that the jet breakup mechanism was significantly different under supercritical conditions. This was consistent with reports from previous imaging studies. Here, PLIF was not used owing to signal attenuation issues associated with the fluoroketone's strong absorption cross section, a challenge that was also present in the work of this thesis.

Despite PLIF's increased use in recent studies shadowgraphy has also seen continued application, especially for cases where the working fluid does not fluoresce (e.g., n-dodecane) and mixing with a tracer is undesirable. Manin et al. [45] at Sandia National Laboratories, used high-speed long distance microscopy to study jets of n-dodecane injected under high pressure and temperature. A short-pulse, high repetition rate LED source was used in combination with a high-speed CMOS camera to resolve the development of fluid structures (e.g., ligaments) in the time domain. Falgout et al. [11] investigated three pure fuels (butanol, dodecane and hexadecane) and Diesel jets using a combination of shadow and ballistic imaging diagnostics. The latter is a line of sight method that can avoid issues of multiply scattered photons (off-axis) by extracting high-quality photons using a series of filtering operations (temporal, spatial, and polarisation-based) from lower-quality background photons. This enables it to image structures (e.g., a jet core) that are surrounded by turbid media such as a dense fog of droplets and/or ligaments. In those experiments the jets issued from a single-hole injector into ambient air under three test cases. For butanol, the images indicated clear morphological changes between case 1 (subcritical)and case 3 (supercritical) as it appeared to have become miscible. Dodecane did not display such pronounced changes, but the images did suggest a weakening of the interface. In the case of hexadecane, ligaments could still be observed that indicated surface tension remained significant. The commercial Diesel fuel did not appear to have undergone any significant changes.

Work by Crua et al. [12] (in collaboration with part of the aforementioned team at Sandia) produced high-resolution shadowgrams for fuel injection into high-pressure and high-temperature vitiated air. This set of experiments has become a benchmark in the development of theory of transcritical fluid injection. To achieve the desired thermodynamic conditions, combustion of a pre-burn mixture was used. The resulting conditions were higher than the required test case, which was ultimately achieved by allowing time for the system to cool down to the desired level. Three different alkane fuels were injected with the optical system obtaining both images and videos of the jets. Once the fuel flow had been shut off, droplets could be seen trailing the main jet. Very high spatial resolution shadowgraphy was then performed on these drops that trailed the injection process. Based on these high-speed and high-resolution image sequences, three regimes of mixing were conceptualised: classical evaporation, transitional mixing, and diffusive mixing. These are depicted in Figure 1.10.

Most of the work reviewed thus far has been experimental, but computational work has also proved to be invaluable in the effort to understand transcritical injection. As an example of how numerical studies can build on experimental results, Mo and Qiao [46] setup Molecular Dynamics (MD) simulations to study the same alkane fuels as Crua et al. They were interested in the evaporation characteristics of these alkanes, which they modelled as films. Ambient nitrogen was used to create sub-critical and trans-critical cases. Crua et al. had recorded and categorised thermodynamic states in their experiments (i.e., based on whether mixing was evaporation or diffusion-dominated) and Mo and Qiao were able to use those data to define a

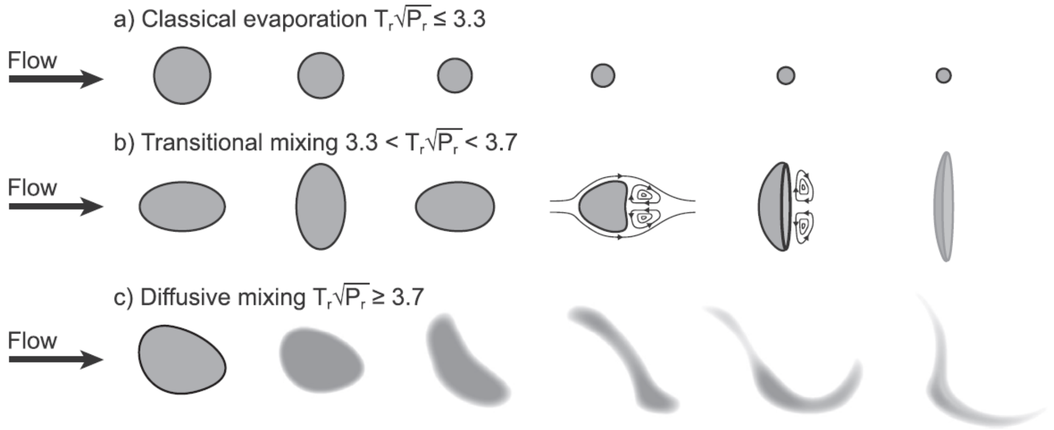

Figure 1.10: Conceptual model of droplet mixing regimes: a) Classical evaporation b) Transitional mixing and c) Diffusive mixing. P_r and T_r are the reduced pressure and temperature based on the pure injectant properties [12].

dimensionless transition time for each of the fuels. To achieve this, contours of the transition time (normalised by the lifetime of the liquid film) were plotted on Pressure-Temperature diagrams. They then noted which contour separated evaporation and diffusion based mixing. One of the main challenges of MD simulations is that they are often restricted to small geometries, typically in the nanometer scale, owing to their high computational cost. Scaling laws were developed as part of this study in an effort to enable the comparison with macroscopic systems.

Besides computational expense, numerical modelling in the near-critical region faces other challenges, such as highly non-linear behaviour of physical properties that can affect accuracy. This is part of the reason why computational fluid dynamics simulations have seen limited application in the design cycle of rocket engines, restricted to secondary verification studies rather than being utilised as primary design tools [47]. Nevertheless, there have been many advancements in the field that have helped establish numerical work as an important part of transcritical research. Much of the pioneering work on thermodynamic models for high pressure flows has been published by Bellan's group who have performed numerical simulations of supercritical mixing layers [48] and have helped to develop much of the theory of modelling for supercritical mixing [49, 50].

Recently, Xiao et al. [51] opted to perform an MD-simulation based study of evaporating fluid droplets under sub- and supercritical conditions. They built on the work of Mo et al. [46] by considering n-dodecane droplets (as these are of "greater practical significance" [51] compared to films) into ambient nitrogen gas. They have argued that many experiments are forced to use droplets in the millimetre length scale which have non-negligible convection forces associated with them, something not encountered in practise in sprays that have much finer droplets. MD simulations are able to avoid this and other issues present in experiments or modelling approaches in the continuum-scale. Their results showed that the droplet lifetime decreased under all ambient conditions with increasing temperature and pressure, which was expected and in agreement with previous reports. Based on a methodology proposed by Mo et al. [46], they used the local mixture critical point, taken from published experimental VLE data, and plotted temperature as a function of n-dodecane mixture fraction at different times. The time at which the critical point was exceeded was then taken to be the time of transition. Example results are depicted in Figure 1.11.

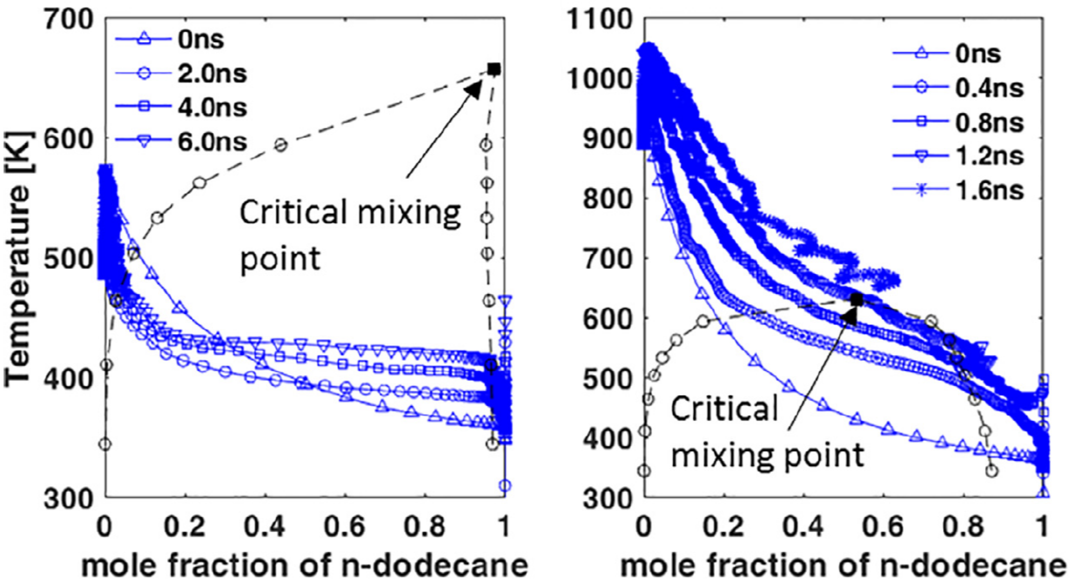

Figure 1.11: Temperature against n-dodecane mole fraction. Left image: Ambient conditions were set at $T_r = 0.91$ and $P_r = 1.21$ with no transition occurring. Right image: Ambient conditions were set at $T_r = 1.67$ and $P_r = 5.96$ with transition observed after 1.2 ns [51].

A German consortium has been studying transcritical phenomena using a variety of diagnostics and experimental configurations. For example, they have investigated highly under-expanded fuel jets issuing into a high pressure and temperature chamber. In search of quantitative data to characterise transcritical phenomena, they have employed Laser Induced Thermal Acoustics (LITA), which is a form of induced grating spectroscopy. LITA was used to perform speed of sound measurements in under-expanded fuel jets, first of n-hexane [52] and subsequently of a fluoroketone [31], injected into ambient nitrogen. In both studies the pure injectant existed in a supercritical state prior to injection into the reservoir, but it was injected into sub-critical conditions as the nitrogen was at room temperature and ambient [31] or near-ambient pressure [52]. The measurement locations were at least 55 nozzle diameters downstream of injection, were the conditions would not have been supercritical. The LITA signal generally consists of a decaying exponential, related to thermal diffusivity, with a superimposed sinuous component, the time period of which can be directly related to the local speed of sound (LITA is generally applied as a point measurement). Moreover, an adiabatic mixing model was used to characterise the mixture formation (concentration) at the measurement locations.

The same group have also performed experiments using droplets [53, 54]. For a review on their work on high-pressure fuel drops see Lamanna et al. [28]. Multiple fluids were investigated (e.g, acetone, n-pentane, n-heptane etc.) with a range of initial diameters from 0.8 to 2.0 mm. Similar to other experiments, the drops were released into ambient nitrogen under high pressure and temperature. This group has, in addition, employed shadowgraphy to monitor flow and droplet morphology. Given the argument of Harstad and Bellan against using shadowgraphy for transcritical interface studies, interface scattering was also monitored concurrently to overcome this issue. Interface scattering was thought to require an intact interface. However, recently published reflectivity analysis on interface scattering results obtained during this thesis work [32] has shown that the reflectivity of a fluid interface may not go to zero as the surface thickens and surface tension diminishes. This point is discussed further in Chapter 5. Nevertheless, interface scattering can provide a metric for the strength of an interface and its broadening even if the destruction of reflectivity does not coincide with the surface tension becoming null. Lamanna et al. [28] used a technique they refer to as ‘front-lighted shadowgraphy’, and simultaneously detected scattering from an interface under all test cases considered (the drop residence time was around 0.5s). One limitation, however, present in released droplet experiments, is that the initial droplet conditions must be sub-critical owing to the need for surface tension to exist at a sufficient level to suspend, and then release, the drop in a stable and controllable manner. In early work, the same group applied calibrated Raman imaging to the drop wake, to provide some of the earliest quantitative mixing results for fuels under these conditions [55].

Gerber et al. [56] have discussed results from a supercritical fuel jet issuing into a shock tube and into a high-pressure, room-temperature chamber. Their jets were characterised by high compressibility and turbulence while their shadowgrams often depicted under-expanded jet structures with well-known shock patterns. The jets were also illuminated with a laser sheet and Gerber et al. monitored the elastically scattered signal. Owing to the presence of shock structures, elastic scattering was observed at locations that indicated a transition out of the supercritical state. They were localised because following shock structures would return the jet to a supercritical state.

Klima et al. [57] have applied Raman spectroscopy to jets of ethanol injected into nitrogen. They were interested in exploring two different routes of mixture formation. One path would cross through the two-phase region of the binary mixture and one would circumvent it such that mixing only involved a single phase (i.e., supercritical mixing). VLE of the binary mixture of ethanol and nitrogen informed their test cases, but the authors noted that the injection process is transient and VLE served to orient them towards the right direction. The aim was to obtain the overall mixture fraction of ethanol, the fraction of ethanol in the liquid phase as well as the liquid temperature and report all of these together at engine relevant conditions. Results of that study showed that in many of their higher pressure and temperature cases, ligaments could be observed indicating that a single-phase mixing path was not actually seen (with the exception of some of the lowest overall concentrations of ethanol, less than 20%). This was true despite the fact that the ambient temperature was significantly higher than the mixture critical temperature for the given isobar. It should be noted, however, that the fuel injection temperature was not actively monitored. The nozzle tip temperature could be controlled within 243 and 373 K both of which are significantly lower than the estimated mixture critical temperature (approximately 500 K).

Considering the background just discussed, a summary of which is given in Table 1.1, the project presented here has the overarching goal of further developing the current state of knowledge of liquid/gas interface development during a thermodynamic transition from a sub-critical to a supercritical state. In pursuit of this goal, several research objectives are defined. The first is to monitor flow morphology (through PLIF imaging), mixture distribution (by scaling the intensity counts in the images) and fluid interface strength (via interface scattering) simultaneously. In this way both transient and averaged data can be visualised and compared. This will further allow the identification of transition locations (where interface strength was near zero) and enable key flow features near them to be examined. Additionally, the transient data could also be observed side-by-side (through video recordings) to see if any correlation can be observed between transient phenomena. The second objective is to leverage the steady and repeatable nature of the test cases (to be defined later) so that further information (e.g., averaged temperature data) from additional experimental campaigns not run simultaneously can be added to the overall data set. These two research objectives involve the application of a combination of diagnostics and use multiple sources of data to piece together a more complete picture of the interface transition process than has previously been achieved. The third research objective is to use the data obtained in further analysis (reflectivity modelling, evaluation of images, temporal estimates) in search of important findings regarding the nature of transition.

A steady, rotationally-symmetric laminar fluid jet was the flow structure studied. Fluoroketone [Novec649$^{\mathrm{TM}}$ by 3M, $CF_3CF_2C(O)CF(CF_3)_2)$] was chosen as the working fluid, for reasons already discussed, with jets injected into steadily-flowing, high-pressure and high-temperature nitrogen. The use of binary mixtures simplified VLE calculations. The choice of a laminar jet is justified as it presents a well-defined interface from the start of injection. Further advantages arise because a laminar jet: 1) obviates the need to follow transient drops, 2) temperature can be measured with physical probes (e.g., thermocouples) because the system is steady and reproducible, and 3) it allows the option of injecting the fluid in an already supercritical or near-supercritical state, as there is no need to maintain surface tension at the start. PLIF and Planar Elastic Light Scattering (PELS) diagnostics are used here to provide more quantitative data than does shadowgraphy.

Note that a laminar jet does not generate the internal re-circulation region found in a realistic injector. This fact could limit the application of such findings to more traditional transcritical sprays. The aim of this work was not to imitate a realistic injection scenario, however, because realistic sprays do not provide unambiguous access to an evolving interface. This work is more basic than work that relies upon sprays.

Table 1.1: Summary of experimental conditions for selected papers discussed in the literature review. The listed information refers to example experiments, and not the entire range of conditions in each publication. Reduced pressures and temperatures refer to the chamber conditions relative to the pure injectant.

Reference	Type	Fluids	P (bar)	P_r	T (K)	T_r
Birk et al. [18]	Spray	H_2O into N_2	280-330	1.27-1.5	293-803	0.45-1.24
Birk et al. [19]	Jet	CH_3I into N_2 (or mixtures of)	64.8-137.9	0.88-1.87	293-623	0.55-1.18
Chehroudi [26]	Jet	LN_2 into gaseous N_2	31.3-91.9	0.93-2.74	300	2.38
Crua et al. [12]	Spray/drops	$C_{12}H_{26}$ into vitiated air	19.8-104.4	1.1-5.8	703.8-1184	1.1-1.8
Dahms et al. [39]	Jet	$C_{12}H_{26}$ into vitiated air	29-60	1.6-3.33	440-900	0.66-1.37
DeSouza and Segal [36]	Coaxial jet	Fluoroketone with N_2 co-flow into N_2	17.8-23.7	0.97-1.29	370-388	0.84-0.88
Falgout et al. [11]	Jet	C_4H_9OH	30-60	0.67-1.33	450-900	0.80-1.60
		$C_{12}H_{26}$		1.65-3.3		0.68-1.37
		$C_{16}H_{34}$		2.11-4.23		0.62-1.25
Lamanna et al. [28]	Drops	C_5H_{12} into N_2	20-60	0.59-1.78	0.95-1.11	445-520
Manin et al. [45]	Jet	$C_{12}H_{26}$ into vitiated air	5-79	0.28-4.36	440-1200	0.67-1.82
Mayer et al. [23]	Jet	LN_2 into N_2 or N_2/He	28-69	0.83-2.03	250	1.98
Mayer et al. [20]	Jet	Cryogenic N_2 into gaseous N_2	39.6-59.6	1.18-1.78	Ambient	-
Muthukumaran and Vaidyanathan [43]	Jet (elliptical)	Fluoroketone into own vapour or N_2	1-36	0.05-1.39	300-494	0.68-1.12
Newman and Brzustowski [17]	Jet	Liquid CO_2 into N_2/CO_2 mixture	63-91	0.856-1.228	295	0.97
Oschwald and Schik [24]	Jet	Cryogenic N_2 into N_2	40-60	1.2-1.8	298	2.36
Segal and Polikhov [29]	Jet	Fluoroketone into N_2	1.4-34.3	0.05-1.86	293-472	0.66-1.07

Chapter 2

Theoretical Background

The Vapour-Liquid Equilibrium (VLE) states for a binary mixture of fluoroketone and nitrogen were calculated using the commercial program FluidProp and the Perturbed Chain-Statistical Associating Fluid Theory (PC-SAFT) Equation of State (EoS). These revealed under which conditions the mixture could be considered to be super-critical and were therefore used as the basis to establish the experimental test cases. In what follows, a review of pure substance thermodynamics is given accompanied by a summary of the main equations used to calculate the VLE states. This forms the basis for the next section that extends to calculations for binary mixtures. Then, validation of the chosen thermodynamic model is presented followed by the Pressure-Temperature (PT) diagram for the fluoroketone/Nitrogen binary mixture. Limitations of VLE calculations are briefly discussed before finally moving on to the project outline and experimental test cases that were designed based on the VLE states calculated here.

2.1 Thermodynamics of pure substances

The discussion in this section applies to pure, simple and compressible (PSC) substances, which make it easier to communicate thermodynamic concepts. 'Pure' refers to the fact that the substance contains only a single type of atom or molecule. The substance has a uniform chemical composition and this does not vary. 'Simple' means that surface and body-force effects from external sources are absent. 'Compressible' means that the volume of a fixed mass can vary.

2.1.1 Sub- and super-critical phase change

A PSC substance can exist in one, or a combination, of the three basic states of matter: solid, liquid and gas. In which of these phases a substance exists depends on its thermodynamic state, which is itself defined through a set of variables, such as temperature, pressure, entropy etc. A diagram depicting the state of matter at which a given substance exists as a function of thermodynamic variables is known as a phase diagram. Since for a PSC substance the thermodynamic state can be fixed using only two, independent and intensive variables, it is possible to create a 2D map of all the thermodynamic states by plotting, as an example, a graph of temperature, T, against specific volume, v. A generic example applying to PSCs is shown in Figure 2.1a, split into several key regions that are common across all such substances. These include the compressed liquid, superheated gas/vapour and saturated liquid-vapour, also referred to as the vapour dome, regions. The vapour dome is enclosed by a curve whose point of inflexion at the top is the critical point, typically quoted in terms of two co-ordinates known as the critical pressure, P_c, and temperature, T_c. For a pure fluid, the critical point is unique and its co-ordinates are substance specific and constant. The portion of the curve running down the left side from the critical point is the saturated liquid line and the portion to its right is the saturated vapour line. The locus of points enclosed by the dome represents all the thermodynamic states where the substance exists in two distinct phases that are in equilibrium with each other. These can equivalently be visualised as a single line in a PT phase diagram, such as Figure 2.1b, extending from the triple point (the single and unique state of a pure substance where all three basic states of matter coexist in equilibrium) up to the critical point. To avoid confusion it should be noted here that this line is known by several different names such as binodal, co-existence and vapour-pressure line. Each point on the binodal is a VLE state that exists at a certain saturation temperature, the value of which can vary along the line. This is equivalent to saying that it is possible to boil water at temperatures other than 100°C, if the ambient pressure is varied. However, for each specific value of saturated temperature only one value of saturated pressure is possible; the pair is unique. Hence, inside the vapour dome the two are no longer independent of each other and one additional variable, such as the specific volume, is needed to fix the thermodynamic state. This value of specific volume will be a weighted average between the two phases with the weight attached to each phase being the molar fraction, i.e. the percentage of the substance that exists in each of the two phases. Note that all points on the saturated liquid and saturated vapour lines lie on the binodal and so the terms may be used interchangeably.

Going from compressed liquid to superheated vapour involves a phase change process (boiling). If this is done while the state of the substance is kept below the critical point then it is necessary to cross through the dome. In this way, a phase change takes place with two distinct phases in coexistence. Separating the two phases is an interface, across which there is a discontinuity in physical variables, for example density. This interface is maintained by the surface tension of the liquid, and for material to leave the liquid phase and enter the vapour phase requires evaporation across the interface. At a given saturation temperature, the "length" of the horizontal line connecting saturated liquid and vapour points is, loosely speaking, representative of the magnitude of this discontinuity and of the strength of the fluid interface as it is related to the latent heat of vaporisation that is in turn associated with surface tension. As the saturation temperature is raised, by increasing the ambient pressure, this line becomes shorter and eventually crushes down to a single, critical point where the density of both phases converges to the same value and they become indistinguishable. At this point, the fluid interface is destroyed and the surface tension associated with it becomes null. All phase changes that take place below the critical point are referred to as sub-critical and will always involve VLE. In contrast, a phase change process above the critical point bypasses the saturated liquid-vapour region and therefore does

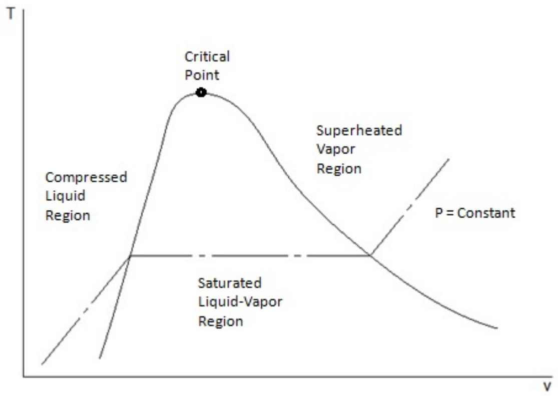

(a) Temperature against specific volume diagram for a PSC substance

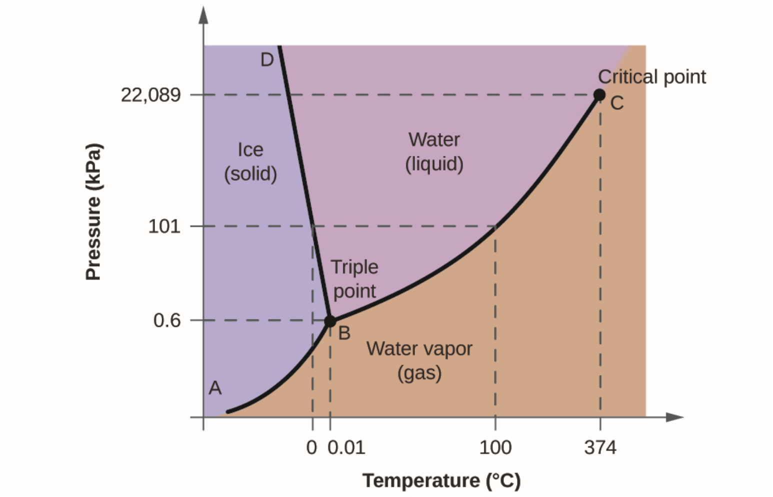

(b) Pressure against temperature graph for water

Figure 2.1: Example phase diagrams. Both diagrams are creative commons images

not exhibit phase coexistence, instead it is a continuous process. This means it does not exhibit jump discontinuities in the values of physical variables and all such phase change processes are referred to as super-critical. Similarly, all thermodynamic states below the critical point are sub-critical and those above are super-critical. It should be noted that both the Widom (aka pseudo-boiling) and Frenkel lines argue that super-critical phase changes are not entirely continuous. Both these lines serve to split the supercritical region into different sectors, with structural transitions taking place as the substance's thermodynamic state is made to cross them, similar to the binodal. The Widom line is defined as the set of "supercritical maximal thermodynamic correlation lengths" [25, 58] and is an extension of the binodal line separating the supercritical regime into a liquid-like and gas-like region. Various methods for its construction are suggested in the literature but a commonly used one is based on connecting maxima of the specific isobaric heat capacity. The Frenkel line is not an extension of the binodal but rather stems from it, extending into the supercritical region and separating it into a 'rigid' liquid regime, able to sustain shear stresses, and a 'gas-like' fluid region. The transition across the Frenkel line is related to particle dynamics and is closely linked with molecular motion. The line marks a threshold, which depends on temperature, where the 'solid-like oscillatory motion ceases' [59], from which point only the gas-like ballistic component of molecular motion remains [60]. For simplicity these are not discussed further here.

The discussion made up to this point suggests that as long as the substance is made to exceed its critical point, as shown in the $T - v$ diagram, then it would have transitioned to a super-critical state. In Figure 2.1a, this can be done by simply bringing the substance to a temperature higher than T_c. In the literature, however, it is perhaps more commonly stated that both P_c and T_c have to be exceeded.

What has so far been discussed concerns, for the most part, VLE states. In general, it is impossible for VLE to occur during a phase transition process so long as one property, be it temperature or pressure, is **maintained** at a higher value than its corresponding critical value. Work by authors such as Bellan [49] defines the super-critical regime as one where multiple phase coexistence is not possible and this is the approach taken here as well. As mentioned previously, other authors have adopted different conventions, and the controversy regarding the definition of a supercritical fluid has not yet been fully resolved. It is acknowledged that, according to the definition adopted here, high-pressure (above the critical pressure) very-low temperature regions of the phase diagram would be considered super-critical even though they would practically correspond to the liquid state. To avoid experimenting under such conditions, the test cases considered in this project were designed to stay close to the coexistence and Widom lines (to be defined below) by considering high pressures and temperatures. The proximity of the test cases to the pure fluid Widom line can be seen in Figure 2.8. Where other pieces of work require both the temperature and pressure to be surpassed for the substance to be considered super-critical, it is partly to avoid the compressed liquid region and to ensure physical properties are intermediate to those of gaseous and liquid states. Even then, however, in the limit of very high temperature and a pressure level marginally higher than the critical pressure, a dense gas-like state would be achieved, which is a similar issue. Irrespective of which definition is adopted, the significance of VLE data remains as they allow the calculation of the critical point.

2.1.2 Vapour-liquid equilibrium

The theory presented here follows the sequence and development presented in Chapter 6 of the book on thermodynamics by Reynolds and Colonna [61]. Full derivations of equations and more in depth discussion can be found there. Here a more condensed version is presented.

A system is said to be in equilibrium if its state does not change with time. For a pure substance that exists in a single phase this means that over the volume it occupies it is entirely homogeneous. For a system that consists of two phases separated by an interface, each phase must be homogeneous within itself but it is also necessary to apply certain restrictions at the interface. The fluid interface is here assumed to be infinitely thin. Consider a closed, isolated system that consists only of a pure fluid. 'Closed' means that the system cannot exchange mass with its surroundings and 'isolated' that it cannot exchange energy. For such a system the conditions for VLE are

$$T^L = T^V \tag{2.1}$$

$$P^L = P^V \tag{2.2}$$

$$g^L = g^V \tag{2.3}$$

The terms T, P and g refer to the temperature, pressure and the specific Gibbs energy, respectively. The superscript L indicates that the value of the property is taken at the liquid phase while V indicates the vapour phase. The specific Gibbs energy is defined as $g \equiv h - Ts$, where h and s represent the specific enthalpy and entropy, respectively. The three equations above demand that the liquid and vapour phases exhibit thermal, mechanical and diffusive equilibrium. The isothermal condition ensures there is no heat transfer and the isobaric (equal pressure) condition eliminates bulk, pressure-gradient driven fluid motion and compression/expansion. The specific Gibbs energy on a molar basis is sometimes referred to as the chemical potential and equating this property in both phases prevents bulk fluid diffusion. These conditions apply in the macroscopic scale, where values of these properties are obtained by taking averages over a large volume and long time period; orders of magnitude longer than the timescales of microscopic fluctuations that all of these properties naturally exhibit. For a closed system in VLE, any liquid that evaporates becomes vapour and vice versa, since no other mass exchange is allowed and there are no chemical reactions. Due to this, it can be shown that at equilibrium $dG = 0$, where G is the Gibbs energy, i.e. the extensive (not specific) property.

Eq. 2.3 can be recast in the form, $g^L - g^V = 0$, and solved numerically at constant T to calculate the corresponding saturation pressure, or the other way around. Unfortunately, at low pressures, such as in the ideal gas limit, the specific Gibbs energy can take very large values which can render numerical solvers unstable. To remedy this, an auxiliary function called fugacity (f) is introduced and defined as

$$f \equiv P \, \exp\left[\frac{g(T,P) - g^{IG}(T,P)}{RT}\right] \tag{2.4}$$

R being the gas constant and the superscript IG indicating the value is for an ideal gas. The fugacity has units of pressure and it is a measure of how much a substance deviates from the ideal gas case. For low pressures, where molecular interactions can be neglected (minus elastic collisions), the fugacity takes on the same value as the pressure predicted by the ideal gas EoS

$$P = \frac{RT}{v} \tag{2.5}$$

It is convenient, then, to define the fugacity coefficient as the ratio of the fugacity (a pressure term that applies to a real gas) to the ideal gas pressure equivalent at the same temperature and specific Gibbs energy

$$\phi \equiv \frac{f}{P} \tag{2.6}$$

The fugacity coefficient $\phi \rightarrow 1$ as $P \rightarrow 0$ (ideal gas limit), unlike the Gibbs function that tends to very large values, and which can present numerical instabilities. The condition for VLE can also be expressed as

$$\phi^L = \phi^V \tag{2.7}$$

From here an analytical expression for ϕ that can then be solved for the saturation pressure is needed . In anticipation of what is to be shown next, another term will be defined here, called the compressibility factor, Z, defined as

$$Z \equiv \frac{Pv}{RT} \tag{2.8}$$

This takes the value of 1 for an ideal gas and is a measure, similar to the fugacity, of how properties deviate from those predicted by the ideal gas law. This term is incorporated in the following ‘template’ expression from which an analytical form of ϕ can be obtained

$$\ln \phi = \frac{1}{RT} \int \left[\frac{RT}{v} - P \right] dv - \ln Z + (Z - 1) \tag{2.9}$$

From here, a volumetric EoS, in the form of $P(T, v)$, can be substituted for the P term in Eq. 2.9. One option is the Van der Waals EoS

$$P = \frac{RT}{v - b} - \frac{a}{v^2} \tag{2.10}$$

where P, R, T and v are the pressure, gas constant, absolute temperature and specific volume, respectively. The terms a and b are substance specific constants that are related to the critical properties and given by

$$a = \frac{27}{64} \frac{R^2 T_c^2}{P_c} \tag{2.11a}$$

$$b = \frac{1}{8} \frac{R T_c}{P_c} \tag{2.11b}$$

If the Van der Waals EoS is chosen then the following equation is obtained

$$\ln \phi = \ln \left[\frac{v}{v-b} \right] - \frac{a}{vRT} - \ln Z + (Z-1) \tag{2.12}$$

By first noting that the VLE condition Eq. 2.7 can also be written as $\ln \phi^L = \ln \phi^V$, Eq. 2.12 can be solved initially using a guessed value of P, to calculate $\ln \phi$ in both phases and then iterate until they are equal. The value of pressure that satisfies this condition is termed the saturation pressure at the given temperature. This is repeated for different values of temperature along the binodal. The result of this computation is the construction of the curve in Figure 2.1a enclosing the saturated liquid-vapour states.

To facilitate visualisation of how this would work in a real application, an example solution is illustrated in Figure 2.2. The calculation is for ammonia, for the $T = 380$ K isotherm using the iPRSV cubic EoS. There are three roots of the VLE condition, indicated by the circles connected by dashed lines. The first and third correspond to the saturated liquid and vapour states, respectively, and the pressure that returns this result (≈ 7.5 MPa) is the saturation pressure at $T = 380$ K. The middle root is an unstable solution and does not correspond to a realisable equilibrium state. It is unstable as it predicts the pressure to be increasing with increasing volume at constant temperature. The following section discusses stability criteria in more detail. Note that the loop is a consequence of the cubic nature of the EoS and is often corrected with the Maxwell construction which replaces it with a horizontal line, effectively requiring the pressure to be constant at the saturated value during a phase transition.

The slope of the vapour-pressure line can be calculated using Eq. 2.13, known as the Clapeyron equation. This will later serve to highlight some of the differences between PSCs and binary mixtures. Eq. 2.13 provides useful insight into the variation of saturation pressure as it shows that the gradient must always be positive, since the latent heat of vaporisation $(h^V - h^L)$ is always positive, and the volume of a vapour is generally greater than that of a liquid at the same pressure and temperature (phase change). Consistent with this is the fact that coexistence curves, as depicted on a PT phase diagram, have a positive gradient.

$$\frac{dP^{sat}}{dT^{sat}} = \frac{h^V - h^L}{T\left(v^V - v^L\right)} \tag{2.13}$$

2.1.3 Phase stability

VLE states have to obey the VLE conditions, Eq. 2.1-2.3. States that do not satisfy them lie outside the saturated liquid-vapour region and are unconditionally stable. To clarify, in the context of discussing VLE, when a single-phase substance is unconditionally stable (the conditions for stability are defined below) it will not separate into multiple phases and the VLE conditions are not satisfied. When a single-phase substance is unconditionally unstable, it does separate into multiple phases and the VLE conditions are satisfied. However, solely satisfying the VLE conditions does not guarantee the onset of phase separation. For this to occur, certain phase

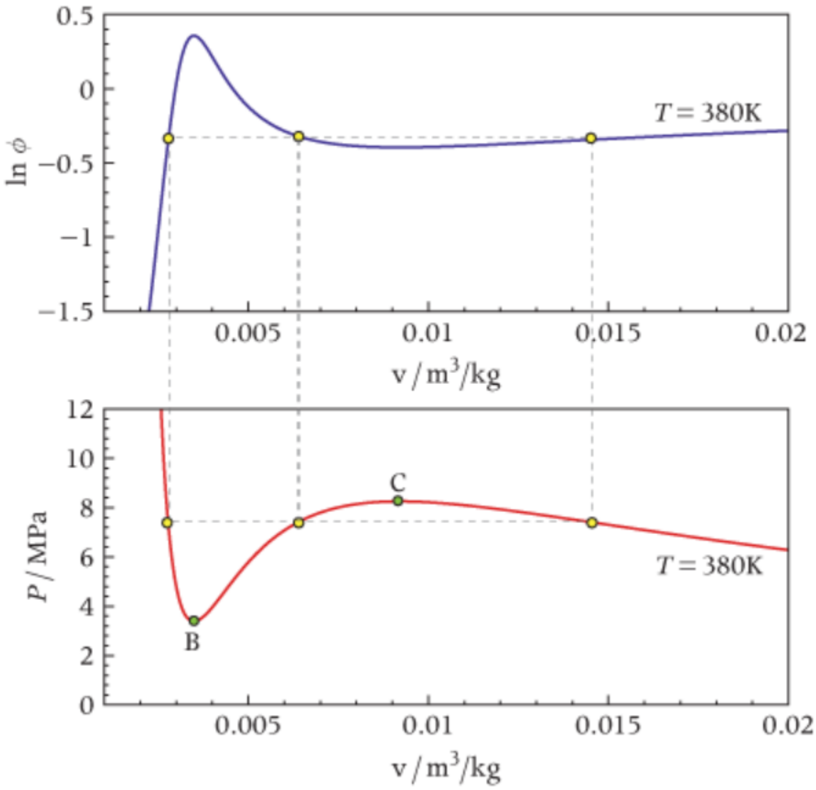

Figure 2.2: Solution at the $T = 380$ K isotherm showing the $P - v$ and $\ln \phi - v$ states calculated with the iPRSV EoS for ammonia [61]

stability criteria have to be violated which force the substance to separate into distinct phases. This suggests the existence of states that satisfy VLE conditions but have not separated into multiple phases. Such states are known as meta-stable states and are discussed below. For a simple fluid that exists as a single, homogeneous phase there are two stability conditions that must be satisfied for it to be stable

$$c_v > 0 \tag{2.14}$$

$$\left(\frac{\partial P}{\partial v}\right)_T < 0 \tag{2.15}$$

The term c_v is the specific heat capacity at constant volume. Equations 2.14 and 2.15 represent the thermal and mechanical stability conditions, respectively. The locus of points connected by the binodal line are unconditionally stable states, where the fluid will never separate into two phases. The same goes for states outside the binodal. Referring back to Figure 2.2, the binodal connects all the points that correspond to either the first or third root (saturated liquid/vapour states) for all isotherms between the triple and critical points. However, notice that the mechanical stability condition is not violated by all states enclosed by the saturated liquid and vapour lines; only those between the inflexion points B and C. At these points $\left(\frac{\partial P}{\partial v}\right)_T = 0$. A curve connecting all of these inflexion points, that represent the limit of mechanical stability, across all isotherms is called the mechanical spinodal. This curve separates the unstable states from the metastable states. Metastable states are those that can potentially be achieved without phase separation but only if large perturbations to the system are avoided, since these can bring about the onset of a transition to VLE. Thus three regions can be defined on a $P - v$ phase diagram:

1. The stable region that exists outside the saturated liquid-vapour dome where phase coexistence is impossible
2. The metastable region that exists between the binodal and spinodal curves. Here stability is conditional and VLE may or may not occur depending on how this thermodynamic state is achieved
3. The unstable region where under all circumstances the substance will separate in two distinct phases.

These regions are illustrated in Figure 2.3 for nitrogen. Notice how the critical point lies both on the binodal and spinodal curves. This gives rise to a more robust definition of a critical point as a thermodynamic state that simultaneously satisfies VLE conditions and is marginally stable as it exists at the limit of stability. This allows the implicit calculation of a critical point, which can be more convenient than one that calculates it directly through its rigorous mathematical definition discussed in Section 2.4.1.

2.2 Thermodynamics of binary mixtures

Mixture thermodynamics can quickly become very complex, especially when considering mixtures with molecules that are very dissimilar to each other. Mixture phase diagrams can be convoluted with multiple liquid sections, discontinuities in the VLE envelopes, liquid-liquid critical lines and more. Theoretical work by van Konynenburg and Scott [62] proposed various classifications of phase behaviour based on critical phenomena and illustrations of some of the main categories of binary mixture phase diagrams can be found in the work of Sadus [63]. For simplification, this section considers simple, non-reacting binary mixtures where the components are themselves pure, simple substances. These are grouped under type 1 phase diagrams, an example of which is illustrated in Figure 2.4a. The approach in this section is to develop the conditions of vapour-liquid equilibrium for binary mixtures with references to the pure substance analogues to both facilitate understanding and highlight differences. A detailed development of theory and equations presented here can be found in [61, ch.8] of which a shorter version is presented in the following paragraphs.

2.2.1 Mole fractions of simple mixtures

Notation for binary mixture mole fractions can be complicated. To avoid confusion, it can be helpful to introduce the notation used to indicate mole fraction under various

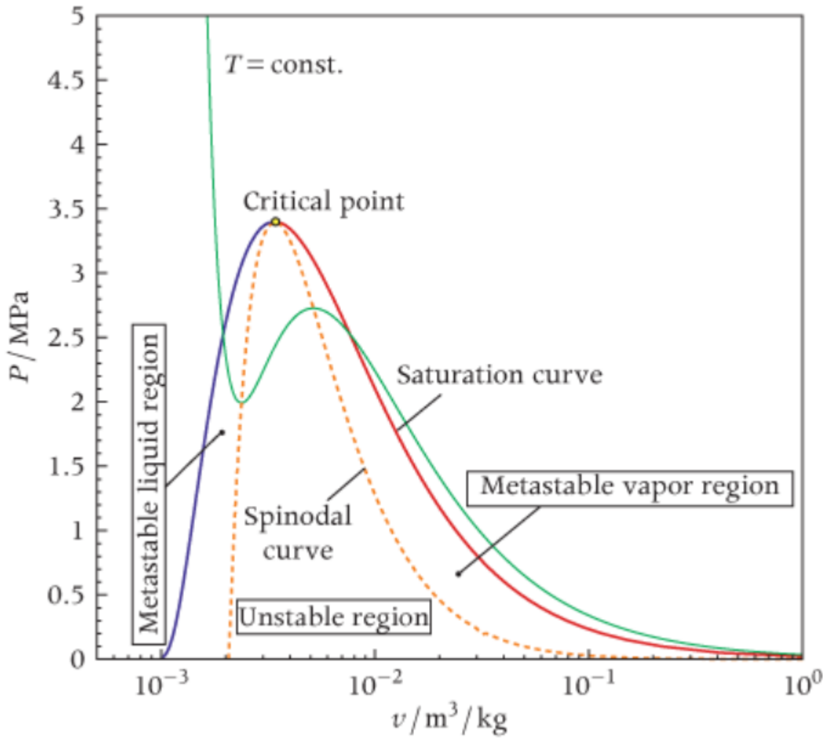

Figure 2.3: P-v diagram for nitrogen depicting the various regions delineated by the binodal and spinodal lines [61]

cases. First, consider a binary mixture that exists in a state that is either entirely liquid or gas. In this case the mole fraction of component i is indicated by z_i. For the example of an equimolar binary mixture, both z_1 and z_2 are equal to 0.5. In the absence of processes that could change the composition (e.g., chemical reactions or addition of one of the components to the mixture), z_i remains constant even if the state of the mixture is changed (e.g., by heating) from liquid to saturated (i.e., VLE) to vapour. When the binary mixture exists in a VLE state, the mole fraction of a component can have a different value in the liquid than in the vapour phase. The mole fractions in the liquid phase and the vapour phase, when the binary mixture exists in a saturated state, are given by x_i and y_i, respectively. Lastly, if the fluid can be treated as an ideal gas the mole fraction of each component is given by χ_i.

2.2.2 Thermodynamic properties and phase behaviour

The state of a PSC substance is defined through its physical properties and the same holds for a binary mixture. Unlike a pure substance though, the properties of a mixture depend in some manner to those of its constituents. It is only in the case of a mixture of ideal gases that the mixing process has no effect on the properties of the individual parts so that their values are the same both mixed and unmixed. This is a consequence of the absence of molecular interactions in the ideal gas model. At a given temperature and pressure, the volume taken up by a molecule that exists in a pure substance, and is therefore surrounded by molecules that are identical to

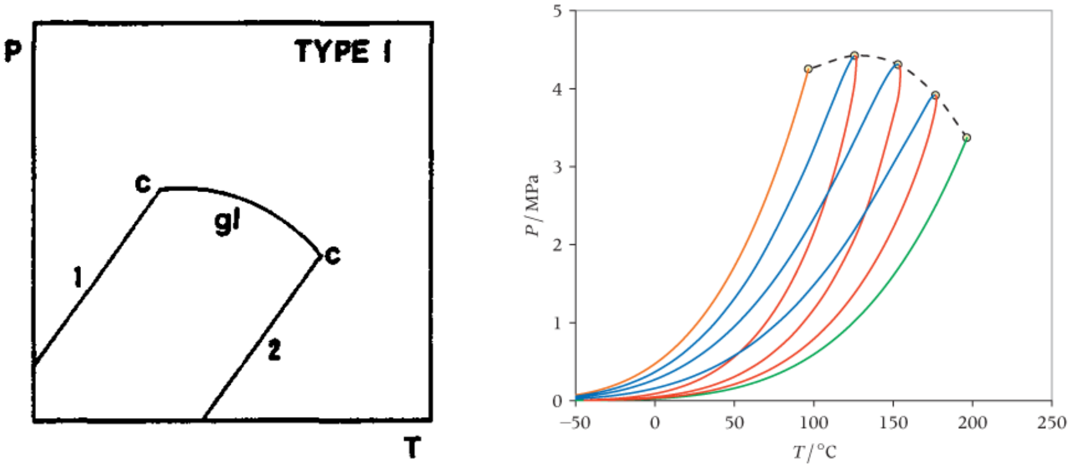

(a) Type 1 phase behaviour for a binary mixture [63]

(b) The binary mixture of propane/n-pentane exhibits type 1 phase behaviour [64]

Figure 2.4: The P-T phase diagram of propane/n-pentane (b) depicts the pure propane and pure n-pentane coexistence lines at the leftmost in orange and rightmost in green, respectively. Bubble lines are blue and dew lines are red and going from left to right the envelopes correspond to propane mole fractions of 0.75, 0.5, and 0.25. The mixture critical points are indicated by circles and the dashed line that connects them, labelled 'gl' in (a), is the critical line.

itself, is different than the space it occupies in a real mixture, where its neighbours can be other types of particles. Additionally, this change in volume depends on the proportion of similar to dissimilar neighbours, as the average attractive, or repulsive, force will change accordingly. The volume of a substance in a mixture on a molar basis is referred to as the partial molar volume and is a function of composition. The partial molar volume is defined as:

$$\bar{v}_i \equiv \left(\frac{\partial V}{\partial N_i}\right)_{T,P,N_{j\neq i}} \tag{2.16}$$

The term N_i is the number of moles of component i. Eq. 2.16 is calculated while keeping the pressure, temperature and number of moles of the other components constant. The total volume of the mixture can be calculated from the partial molar volume of its parts using the following relation:

$$V = \sum_{i=1}^{nc} N_i \times \bar{v}_i \tag{2.17}$$

The term nc stands for number of components. All other mixture extensive properties (properties whose value depends on the amount or extent of the system) such as enthalpy, entropy and the Gibbs energy, can be calculated from the partial molar properties of the components using the same method as Eq. 2.17. The overall mole fraction, z, refers to the fluid when it is either entirely liquid or gas. For component i, it is calculated as $z_i = N_i/N$, with N being the total number of moles of the mixture. The specific Gibbs energy of the mixture, essential for VLE calculations, can then be calculated using the following equation:

$$\hat{g} = \sum_{i=1}^{nc} z_i \times \bar{g}_i \tag{2.18}$$

In the above equation, $\bar{g}_i$ is the partial molar Gibbs energy of component i. For consistency, variables with a hat, e.g $\hat{a}$, refer to a property of the mixture or a pure component when unmixed, whereas variables with a bar, e.g. $\bar{a}$, refer to a partial molar property. Clearly, mixture properties depend on composition, and mixing can lead to non-linear changes in their values. An example of such a variation can be seen in the phase behaviour of a simple mixture. On a PT diagram, such as the one in Figure 2.4, pure substances have a continuous binodal line that terminates at a unique critical point. Examples of this are the single lines representing pure propane and n-pentane in Figure 2.4b. In contrast, PT diagrams of binary mixtures exhibit phase envelopes, formed by the bubble and dew lines. The bubble line consists of all the bubble points at the given composition. A bubble point is found by heating the initially entirely liquid mixture, at a given constant ambient pressure and composition, until the first bubble of gas is formed. A similar process is used for the dew line with each dew point found by cooling an initially gaseous mixture until the first droplet appears. All phase envelopes exhibit a critical point which corresponds to a specific mixture composition and the T_c and P_c of each critical point changes based on composition. A line connecting all of the critical points is referred to as the critical line or locus. From the critical line drawn (dashed) in Figure 2.4b several interesting features can be identified.

- The critical point with the highest temperature (aka cricondentherm) does not necessarily exhibit simultaneously the highest pressure (aka cricondenbar) of any critical point.
- The highest possible pressure at which VLE is possible can be higher than the critical pressures of both pure components.
- The critical line connecting the critical points of the two pure components is not a straight line; it is a curve. The variation with composition is non-linear and so a composition-weighted average of the pure component critical properties would be an inaccurate estimation of the mixture critical point.

In the specific example of the propane/n-pentane binary mixture, the cricondenbar is not much higher than the critical pressure of either component in pure form. However, this is the case here because of the simplicity of the mixture. Where molecules are significantly dissimilar, as can happen in the case of conventional fuels and oxidisers, the increase in critical pressure with mixing can be very rapid. This will be demonstrated in Section 2.3 with both numerical and experimental data. It is important, therefore, to calculate the extreme conditions under which VLE is possible for a mixture, to predict a transition to the super-critical regime, and to do this it is necessary to determine the conditions for VLE as they apply to mixtures.

2.2.3 VLE conditions and phase stability

VLE conditions

For a pure fluid that exists as a closed, isolated system at constant pressure and temperature the VLE conditions are given by Equations 2.1, 2.2 and 2.3. For a binary mixture, Eq. 2.3 is extended to all components as follows

$$\bar{g}_i^V = \bar{g}_i^L \qquad i = 1, 2, \ldots, nc \tag{2.19}$$

The term $\bar{g}_i$ is the partial molar Gibbs function, also known as the chemical potential and is defined as

$$\bar{g}_i \equiv \left(\frac{\partial G}{\partial N_i}\right)_{T,P,N_{j\neq i}} \tag{2.20}$$

Eq. 2.19 shows that for VLE, each component's $\bar{g}$ must be equal in both phases. This condition can be equivalently expressed in terms of the fugacity

$$\tilde{f}_i^V = \tilde{f}_i^L \qquad i = 1, 2, \ldots, nc \tag{2.21}$$

The tilde symbol indicates the property applies to the fluid in the mixture but it is not a partial molar property. This is because the fugacity of the mixture can not be calculated with an expression analogous to Eq. 2.17. The fugacity of a component in the mixture is defined as

$$\tilde{f}_i \equiv \chi_i P \, \exp\left[\frac{\bar{g}_i - \bar{g}_i^{IG}}{\hat{R}T}\right] \tag{2.22}$$

where χ_i is the mole fraction of component i if it were an ideal gas and $\hat{R}$ is the universal gas constant. The fugacity coefficient can then be defined as

$$\tilde{\phi}_i \equiv \frac{\tilde{f}_i}{y_i P} \tag{2.23}$$

with the term y_i referring to the mole fraction in the (real) vapour state. x_i is the notation used for the mole fraction in the liquid state and can replace y_i to calculate the fugacity coefficient in the liquid phase. Finally, similar to pure fluids, the VLE condition can be recast in terms of the fugacity coefficient as follows

$$y_i \tilde{\phi}_i^V (T, P, y_i) = x_i \tilde{\phi}_i^L (T, P, x_i) \qquad i = 1, 2, \ldots, nc \tag{2.24}$$

Similar to Eq. 2.9, the natural logarithm of the fugacity coefficient can be calculated by

$$\ln \tilde{\phi}_i = \frac{1}{\hat{R}T} \int_{\infty}^{\hat{v}} \left[\frac{\hat{R}T}{\hat{v}} - N \left(\frac{\partial P}{\partial N_i} \right)_{T,\hat{v},N_{j \neq i}} \right] d\hat{v} - \ln Z \tag{2.25}$$

The above expression is suitable for numerical schemes as it behaves in a stable manner. The equilibrium conditions given by Eq. 2.24 result in a system of equations that have to be solved to calculate the VLE states. For this, a suitable EoS is needed that can be used to calculate Eq. 2.25 in an iterative manner, both in the liquid and vapour phase until the VLE condition is satisfied. As a last remark to demonstrate the difference between pure fluids and mixtures, it can be shown that the Clapeyron equation for mixtures is

$$\left(\frac{dP}{dT} \right)^{bubble} = \frac{\sum_{i=1}^{nc} y_i \bar{h}_i^V - \sum_{i=1}^{nc} y_i \bar{h}_i^L}{T \left(\sum_{i=1}^{nc} y_i \bar{v}_i^V - \sum_{i=1}^{nc} y_i \bar{v}_i^L \right)} \tag{2.26}$$

Compared with the pure fluid version, Eq. 2.13, the Clapeyron equation for the bubble line of mixtures is complicated by the presence of partial molar properties (enthalpy and volume) as well as the dependence on the vapour phase composition.

Phase stability

In Figure 2.4b, it was shown that the critical properties of the mixture can be greater than those of both its constituents. This can be partly explained by considering the requirements for phase stability in mixtures. For a pure fluid, phase stability is ensured when the conditions expressed by Equations 2.14 and 2.15 are satisfied. This is not sufficient, however, for multi-component fluids where phase separation can also be initiated by diffusion [13]. Diffusional stability is guaranteed when the partial molar Gibbs energy of a component increases when the concentration of that component in the mixture is increased, at constant pressure and temperature. In mathematical terms

$$\left(\frac{\partial \bar{g}_i}{\partial N_i} \right)_{P,T} > 0 \tag{2.27}$$

Figure 2.5 shows the pressure against fuel mole fraction phase diagram, at an isothermal plane, for the $C_{12}H_{26}/N_2$ binary mixture. Within the two-phase envelope there are two regions where the mixture is unconditionally unstable; one due to diffusional and one due to mechanical instabilities. In the case of a pure fluid, the critical point would coincide with the highest pressure of the mechanical spinodal. This is a key difference of binary mixtures where now diffusional instabilities mean that two phase separation can happen at pressures much higher than the limit of the mechanical spinodal. The highest pressure at which VLE is possible, i.e. the critical point at this isotherm, now coincides with the limit of diffusional stability.

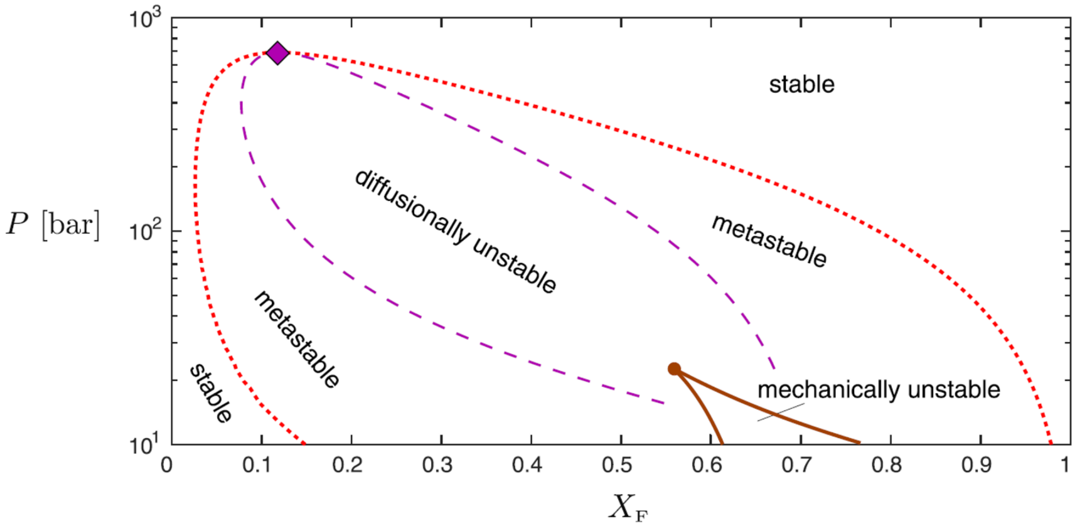

Figure 2.5: Pressure against mole fraction (fuel) diagram of the $C_{12}H_{26}/N_2$ binary mixture [13]

2.3 Binary mixture of fluoroketone and Nitrogen

2.3.1 Choice of fluid

“Novec 649”, a commercially available fluoroketone produced by 3M, was chosen as the working fluid for this project. Fluoroketone has favourable critical properties ($T_c = 169$ °C and $P_c = 1.88$ MPa) that are easier to achieve experimentally than those of other fluids. To study transitions to the super-critical regime, the substance has to be subjected to high temperatures. Fortunately, fluoroketone exhibits low reactivity and thermal stability up to 500°C [38]. It also fluoresces when excited by incoming light at 355nm, meaning it can be studied via laser induced fluorescence without the addition of a tracer. Novec 649 (fluoroketone) is a refrigerant and so it is not widely used as a surrogate for fuel. However, it has been studied before by other research groups doing related super-critical investigations, has favourable properties and its photo-physics have been well documented and published. For an experimental study into the fundamentals of thermodynamic transitions, rather than combustion mechanics, fluoroketone was a suitable choice. Experimental VLE data have also been published on the binary mixture of fluoroketone with nitrogen which enabled the validation of the chosen EoS for VLE calculations.

2.3.2 Equation of state, FluidProp and model validation

There are numerous EoS available for predicting the vapour-liquid coexistence region of binary mixtures. Two such EoS include the Peng-Robinson and PC-SAFT models. Linnemann and Vrabec [65] used a view cell to detect the critical locus for fluoroketone/N$_2$ mixtures by observing the disappearance of the liquid/gas interface at specific pressures and temperatures, for various mixture fractions. They then compared the performance of the Peng-Robinson and PC-SAFT models for the mixtures they had observed, and they reported that the PC-SAFT model matched the experimental data more closely. PC-SAFT is an equation of state that models molecular interactions. For pure fluid modelling purposes, three substance-specific parameters are required. These include the segment diameter, segment energy parameter, and the number of segments per chain. To calculate VLE states of binary mixtures, these parameters are supplemented with a binary interaction parameter that can be calibrated using experimental data. Assuming a weak dependence on temperature, the interaction parameter becomes a model constant. Given these parameters, the model is able to calculate the Helmholtz free energy (related to the Gibbs function) from which thermodynamic properties, including the fugacity, can be calculated [66].

To establish conditions under which vapour and liquid cannot co-exist within the chamber, it is useful to identify the critical locus on a graph of pressure against temperature. Here the commercial software FluidProp$^{\mathrm{TM}}$ was used to calculate VLE states. FluidProp can execute the calculations with a number of different EoS-based models, including PC-SAFT. Gross and Sadowski (see e.g. [66]) developed the PC-SAFT equation of state and provided a summary of the main equations used to calculate thermodynamic properties (e.g. pressure and fugacity). FluidProp is a commercial code and the specific details regarding how it solves equations are unpublished. It would nonetheless make use of the equations summarised in the paper by Gross and Sadowski [66] in some form, and the algorithm may depend on what the calculation objective is (e.g., pure substance thermodynamic property or phase equilibrium). The overall numerical scheme used in FluidProp is based on chapter 12 in the book by Michelsen and Mollerup [67].

VLE calculations can be highly non-linear, however, and it is good practice to replicate experimentally obtained data in order to validate the code's performance. In personal communication with the company developing FluidProp, the PC-SAFT model parameters for Novec 649 (fluoroketone) were updated to match the ones reported by Linnemann and Vrabec [65]. Following this update, agreement between the model and the data was good, as illustrated in Figure 2.6. Unfortunately, the program struggled to calculate the bubble line for part of the composition range (mole fraction of nitrogen from 0.4 to 0.7). Despite not being able to calculate VLE states for all of the compositions, the model was able to predict bubble-point pressures correctly up to nitrogen mole fractions of 0.4 for all cases, and the agreement with experimental data was near perfect in that region. Additionally, in the case of the 420 K isotherm, which is closer to the temperatures of the experimental cases in this work, the prediction is close at the critical point as well. The inaccuracy appears to be lower at higher temperatures, with the worst error being at the lowest (360 K) isotherm where the critical pressure was over-estimated. The highest predicted VLE pressure occurs at the 360 K isotherm and is just over 200 bar, in agreement with the PC-SAFT prediction reported by Linnemann and Vrabec. For the 360 K and 390 K isotherms, VLE is possible beyond a nitrogen mole fraction of 0.7 and the model predicts the maximum value of concentration for VLE to be approximately 0.9 and 0.8, respectively, which is also in agreement with what was reported [65].

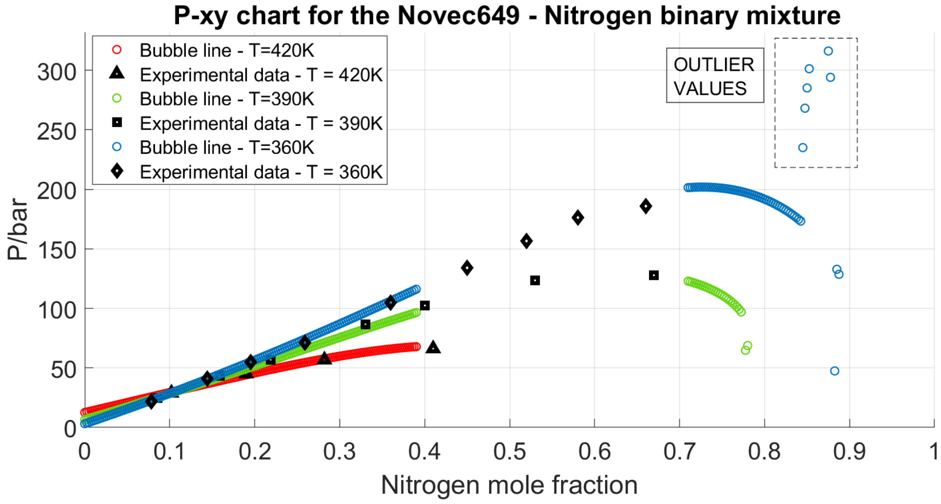

Figure 2.6: fluoroketone/nitrogen phase envelopes at various isotherms presented as pressure against mole fraction of nitrogen plots, supplemented with experimental data published in [65]

2.3.3 The pressure-temperature phase diagram

The PT diagram was calculated at different concentrations and the results are shown in Figure 2.7, illustrating clearly that by adding nitrogen to the mixture, the critical pressure increases rapidly, reaching values that can be more than an order of magnitude higher than the critical pressure of pure fluoroketone. This effect is more profound in the case of high mole fractions of nitrogen and at low temperatures. In contrast, the mixture critical temperature decreases as nitrogen is added. Similar effects have been reported in other binary mixtures involving nitrogen (e.g., see Figure 3b in [1]). The results shown here had important consequences for the choice of experimental test cases as at least one needed to be unconditionally super-critical, i.e. irrespective of mixture composition, which would exhibit a distribution in the experimental vessel, the mixture needed to be super-critical. Unfortunately, the experimental setup, described in Section 3.1, could not reach pressure levels high enough to ensure the critical pressure would be exceeded at all compositions and temperatures. Despite this, so long as the cricondentherm was exceeded then VLE would not be possible and within the context of this report this means the mixture was considered super-critical. Interestingly, if the mixture were to be defined as super-critical when both the cricondentherm and cricondenbar are exceeded, the supercritical region would begin at a point, located by these two extreme properties as co-ordinates, that would not be coincident on any of the phase envelopes. This is counter-intuitive, since the critical point is often described as the point where the liquid and gaseous states converge and become indistinguishable, and in the case of a pure fluid is geometrically identifiable as the inflection point on both the binodal and mechanical spinodal lines.

The PT phase diagram was an important step in defining the test cases to be performed over the course of this study. That said, there are some inherent limitations of VLE calculations. Before presenting the scope and experiments of this study,

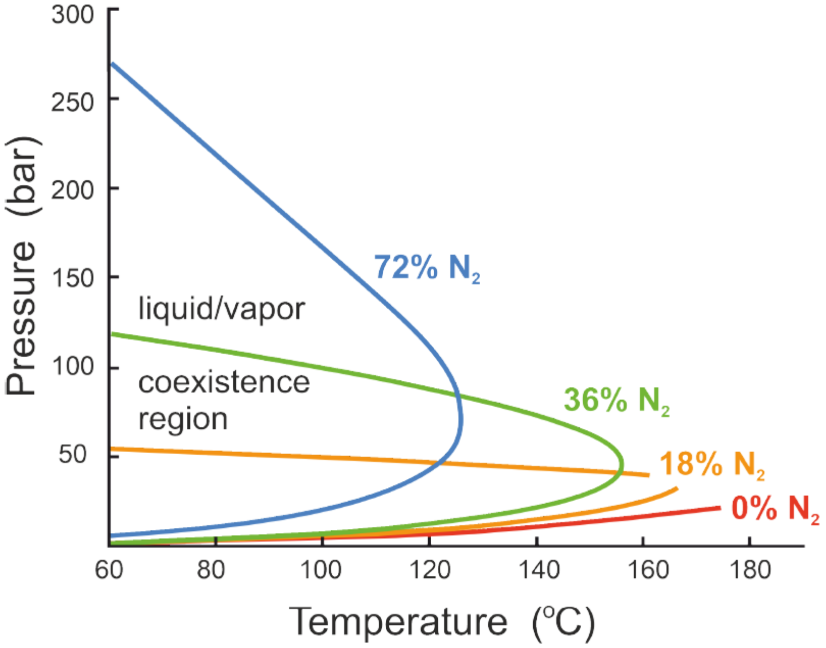

Figure 2.7: fluoroketone-Nitrogen iso-concentration phase envelopes plotted on a pressure against temperature graph

a critical discussion of these limitations will be useful to caution the drawing of conclusions.

2.4 Limitations of VLE calculations

2.4.1 Direct calculation

Calculation of the PT phase diagram for a binary mixture is not a direct calculation of the critical point at a specified composition. Rather it is an implicit one and it is in fact possible to calculate the critical point directly. Gibbs [68] developed the rigorous definition of the critical point for an m-component fluid that can be expressed mathematically in terms of the Gibbs function. However, it can be more simply presented in terms of the Helmholtz energy function, $A \equiv U - TS$. This is more suitable for use with EoS that are explicit in pressure, i.e. $P = P(T, V)$ because these return a unique value for pressure given a specified volume [63]. The conditions for the critical point of an m-component fluid, expressed in determinant form, are given by Equations 2.28, 2.29 and 2.30.

$$W = \begin{vmatrix} -\left(\frac{\partial^2 A}{\partial V^2}\right)_T & -\left(\frac{\partial^2 A}{\partial V \partial x_1}\right)_T & \cdots & -\left(\frac{\partial^2 A}{\partial V \partial x_{m-1}}\right)_T \\ \left(\frac{\partial^2 A}{\partial x_1 \partial V}\right)_T & \left(\frac{\partial^2 A}{\partial x_1^2}\right)_{T,V} & \cdots & \left(\frac{\partial^2 A}{\partial x_1 \partial x_{m-1}}\right)_{T,V} \\ \cdots & \cdots & \cdots & \cdots \\ \left(\frac{\partial^2 A}{\partial x_{m-1} \partial V}\right)_T & \left(\frac{\partial^2 A}{\partial x_{m-1} \partial n_1}\right)_{T,V} & \cdots & \left(\frac{\partial^2 A}{\partial x_{m-1}^2}\right)_{T,V} \end{vmatrix} = 0 \qquad (2.28)$$

$$X = \begin{vmatrix} \left(\frac{\partial W}{\partial V}\right)_T & \left(\frac{\partial W}{\partial x_1}\right)_{T,V} & \cdots & \left(\frac{\partial W}{\partial x_{m-1}}\right)_T \\ \left(\frac{\partial^2 A}{\partial x_1 \partial V}\right)_T & \left(\frac{\partial^2 A}{\partial x_1^2}\right)_{T,V} & \cdots & \left(\frac{\partial^2 A}{\partial x_1 \partial x_{m-1}}\right)_{T,V} \\ \cdots & \cdots & \cdots & \cdots \\ \left(\frac{\partial^2 A}{\partial x_{m-1} \partial V}\right)_T & \left(\frac{\partial^2 A}{\partial x_{m-1} \partial n_1}\right)_{T,V} & \cdots & \left(\frac{\partial^2 A}{\partial x_{m-1}^2}\right)_{T,V} \end{vmatrix} = 0 \tag{2.29}$$

$$Y = \begin{vmatrix} \left(\frac{\partial X}{\partial V}\right)_T & \left(\frac{\partial X}{\partial x_1}\right)_{T,V} & \cdots & \left(\frac{\partial X}{\partial x_{m-1}}\right)_T \\ \left(\frac{\partial^2 A}{\partial x_1 \partial V}\right)_T & \left(\frac{\partial^2 A}{\partial x_1^2}\right)_{T,V} & \cdots & \left(\frac{\partial^2 A}{\partial x_1 \partial x_{m-1}}\right)_{T,V} \\ \cdots & \cdots & \cdots & \cdots \\ \left(\frac{\partial^2 A}{\partial x_{m-1} \partial V}\right)_T & \left(\frac{\partial^2 A}{\partial x_{m-1} \partial n_1}\right)_{T,V} & \cdots & \left(\frac{\partial^2 A}{\partial x_{m-1}^2}\right)_{T,V} \end{vmatrix} > 0 \tag{2.30}$$

The first two equations are equal to 0 at the critical point. They can be solved on their own in isolation of Eq. 2.30, complemented by an EoS such as the Peng-Robinson, to predict the critical properties of a pure fluid or multi-component mixture. An example can be found in [69]. The third condition is needed to check the stability of the calculated critical point and must be greater than zero. Direct calculation of these conditions can be complicated and computationally expensive, particularly for multi-component mixtures. It is more common to calculate the binodal curve instead and find the location at which it is tangent to the spinodal curve for the substance [63]. By not calculating the stability determinant there is no guarantee that the calculated critical point will be a stable phase. Given experimental data, however, it is possible to identify erroneous critical points and verify the accuracy of a model, something that is more tractable for binary mixtures (than for higher multi-component mixtures) for which experimental data are more readily available in the literature.

2.4.2 Accuracy and validity of VLE states

It was mentioned previously that adjusting the PC-SAFT model parameters had a significant impact on the predicted VLE states as was seen on updating the fluoroketone constants in FluidProp. The sensitivity of the results on the model constants means that the accuracy of the VLE predictions must not be overly trusted and has to be supplemented with sufficient experimental data. Where high accuracy is required this must be balanced with very accurate measurements to ensure precise model parameter values can be extracted by fitting them to the data. In this work, what was important were the trends revealed by the VLE calculations that on one hand showed it would not be possible to achieve the pressures necessary under all conditions for supercritical transition, but on the other that the highest critical temperature could be exceeded. Furthermore, in fluid jet studies there are also fluid dynamic processes at play and there may not be enough time for thermodynamic equilibrium to be established. This limits the applicability of VLE calculations since the state inside and around the jet may be out of equilibrium. Nevertheless, the critical point is itself an equilibrium state and the conditions at which it occurs can be predicted by both direct and indirect calculation. Ultimately, the results shown in Figure 2.7 were used to design experimental cases of increasingly demanding thermodynamic conditions, culminating at a high pressure and temperature test case that *increased the likelihood* of experimentally observing a critical transition.

2.4.3 Estimating transition length

The VLE calculations formed the basis for the fully sub-critical and fully super-critical cases. However, they cannot be used on their own to design a test case where the injected fluid exists initially at a sub-critical state and then transitions to the super-critical regime during its transit time in the chamber. For this type of test case, referred to as trans-critical, it is necessary to model heat transfer to the injected fluid and obtain an estimate of the length scale required to heat the liquid from a sub-critical to a super-critical temperature. This would indicate whether a transition could be expected within the space available in the experimental vessel given the set of thermodynamic conditions. A simple calculation modelling heat transfer to a sphere of fluoroketone falling through a space filled with nitrogen was used to obtain an estimate of the length needed, given several different possible scenarios of ambient pressure, temperature as well as required fluoroketone mass flow-rate and injection temperature. This calculation was used for the design of the trans-critical test case and is described in more detail in Appendix A.

2.5 Present study

In this work, laminar fluid jets of fluoroketone 649 issuing into a chamber filled with ambient nitrogen were studied by optical diagnostics and temperature sensors. The chamber conditions into which the fluid jet was injected could be controlled, as could the state of the injectant prior to entering the chamber. The experimental setup is described in the next chapter. The test cases are shown in Table 2.1 where T_f and T_{ch} are the fluid and chamber temperature, respectively, and P_{ch} is the chamber pressure. The description column indicates the general state of the fluid prior to injection, i.e relative to the pure component, and the chamber state relative to the mixture critical temperature. Reduced temperatures (T_r) and pressures (P_r), defined by $T_r \equiv T/T_c$ and $P_r \equiv P/P_c$, are often reported in the literature. For the binary mixtures in this study, T_r and P_r depend on fluoroketone mixture fraction and hence position in the chamber, so they are not reported here. Table 2.2 contains the reduced temperatures and pressures for pure fluoroketone inside the nozzle, for all six test cases.

For all test cases the same mass flow-rate, $\dot{m} = 900$ g/hr, of fluoroketone was used. For test cases 1,2 and 3 the pure fluoroketone was injected in a sub-critical, super-critical and near-critical state, respectively, while the ambient environment into which it was injected was sub-critical relative to the mixture. For test cases 4,5 and 6 the chamber temperature was super-critical relative to the mixture critical temperature. Test case 4 was the trans-critical test case where the fluid jet temperature was expected to exceed the mixture supercritical temperature as it travelled through the chamber. For case 5 the jet was injected at a pressure exceeding the pure fluid P_c but

Table 2.1: Experimental test cases. On a day-to-day basis, feedback-controlled liquid temperatures are reproducible to $\pm\, 0.1°$C, gas temperatures are reproducible to $\pm\, 1°$C, and pressure is reproducible to $\pm\, 0.1$ bar.

Test case	T_{Novec} (°C)	T_{chamber} (°C)	P_{chamber} (bar)	Description
1	160	150	16	Subcritical jet into subcritical chamber
2	190	150	16	Superheated vapor ($T > T_c$ but $P < P_c$ inside injector) into subcritical ($T_{\text{ch.}} < 170\,°\text{C}$) chamber
3	170	170	19	Critical point ($T_c\,\&\,P_c$ inside injector) into critical point ($T_{\text{ch.}} = 170\,°\text{C}$) chamber
4	160	220	16	Subcritical (inside injector) into supercritical ($T_{\text{ch.}} > 175\,°\text{C}$) chamber
5	160	220	31	Compressed liquid ($P > P_c$ but $T < T_c$ inside inj.) into supercritical ($T_{\text{ch.}} > 175\,°\text{C}$) chamber
6	190	220	31	Supercritical ($P > P_c$ and $T > T_c$, inside injector) into supercritical ($T_{\text{ch.}} > 175\,°\text{C}$) chamber

Note: pressures reported here are absolute pressure. T_{chamber} is measured by an off-centreline type K thermocouple located 40 mm below the nozzle exit.

below T_c. For case 6 the fluid was injected at $P > P_c$ and $T > T_c$. How the thermodynamic conditions were established and controlled are explained in more detail in the following chapter. A total of three experimental campaigns were conducted in this project.

1. Simultaneous Planar Laser Induced Fluorescence (PLIF) imaging and Planar Elastic Light Scattering (PELS) formed the first campaign. PLIF monitored and imaged the fluoroketone distribution while PELS monitored the strength of the interface through the scattered signal average intensity.

2. Temperature measurements were performed at all test cases using thermocouples. Temperature maps in the injection plane were acquired for test cases 2,3,4

Table 2.2: Reduced temperatures and pressures for pure fluoroketone inside the nozzle, for the test cases in Table 2.1

Test case	T_{Novec} $(°C)$	T_r	P (bar)	P_r
1	160	0.98	16	0.85
2	190	1.05	16	0.85
3	170	1.00	19	1.01
4	160	0.98	16	0.85
5	160	0.98	31	1.65
6	190	1.05	31	1.65

and 6.

3. Magnified PLIF imaging with improved spatial resolution and greater magnification factor provided more detail on fluoroketone distributions.

The next chapter describes in detail the experimental setup followed by the underlying theory and application of the optical diagnostics used. The calibration and methodology of temperature measurements is also discussed.

2.5.1 Novec 649 (fluoroketone) coexistence and Widom lines

The Widom line can be thought of as an extension of the coexistence line for a pure substance (the 0% N_2 line in Figure 2.7) into the supercritical region. The location of the Widom line on a pressure/temperature plot is typically defined in terms of maxima in the constant pressure specific heats (C_p) [58]. Here we have used FluidProp to estimate the locations of C_p maxima for pure fluoroketone as a function of pressure and temperature. The result is plotted in Figure 2.8, on which test case points (from Table 2.2) for pure fluoroketone inside the nozzle have also been plotted, together with chamber conditions (purely for reference). When the thermodynamic state of a substance crosses the Widom line, a non-linear transition occurs. The inset in Figure 2.8 shows the variation of C_p with temperature, at several relevant isobars both below and above the critical pressure of pure fluoroketone. The temperatures at which the C_p maxima occur (at supercritical pressures) correspond to points on the Widom line. To cross the Widom line from left to right is termed "pseudoboiling". According to Banuti [25], beyond a supercritical pressure of $P/P_c > 3$, C_p maxima can, in general, be expected to have completely decayed and pseudoboiling effects become negligible. This is reflected in the fact that the C_p peak at the 31 bar level, depicted by the inset in Figure 2.8, is significantly less pronounced than the peak at the 19 bar level.

The highest reduced pressure achieved here was $P_r = 1.65$ (for cases 5 and 6). For case 6 especially, pseudoboiling effects are not negligible and should be considered because the injection conditions of the pure fluid are in the vicinity of the Widom line. The injectant conditions under test cases 1, 2 and 4 are at sub-critical pressures. In test case 5 the reduced pressure is $P_r = 1.65$ but the injection temperature is low enough that no pseudoboiling effects would take place (see the C5 point in Figure 2.8). Under test case 6, however, the injectant exists at a state that is very close to the Widom line. At 31 bar, the pseudoboiling temperature, T_{pb}, is estimated to be $192.4\,°$C and the injection temperature is $190\,°$C. The injection temperature will be subject to fluctuations, however, and there is an error associated with estimating T_{pb} via an EoS. Furthermore, the lower C_p maximum at elevated supercritical pressures is accompanied by a broadening of the C_p curve, meaning pseudoboiling effects can be expected at that condition since they take place over a larger range of temperature. As will be discussed later, this is one possible reason for a detected drop in temperature during injection under test case 6.

Test case 3 is unusual because of a critical point overestimation by the PC-SAFT EoS as applied using FluidProp. The program considers 19 bar to be a sub-critical pressure for pure fluoroketone (it estimates the critical pressure to be 21.39 bar). Furthermore, it should be noted that the blue C_p curve in the inset plot of Figure

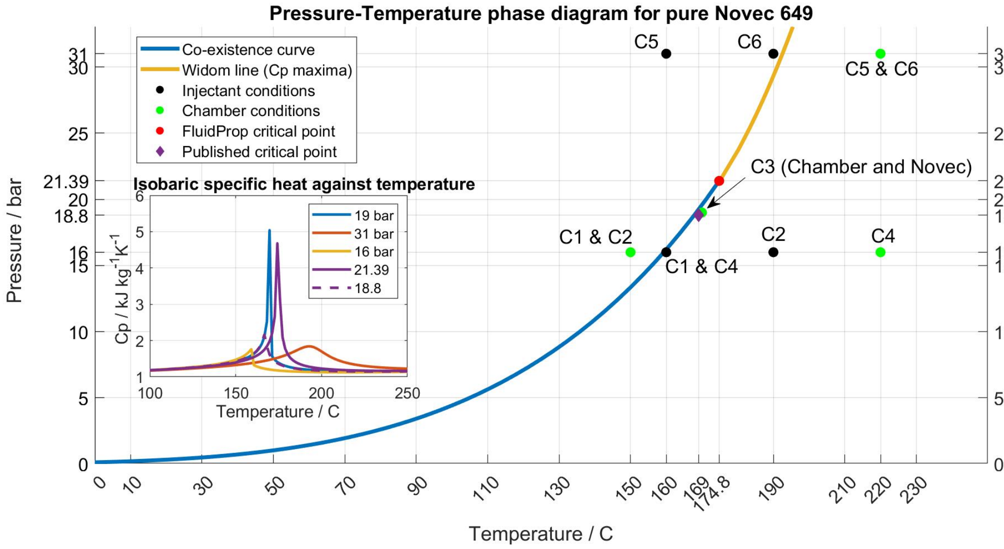

Figure 2.8: PT phase diagram for pure fluoroketone, showing the coexistence and Widom lines, both calculated using FluidProp$^{\mathrm{TM}}$. Both the injectant and chamber conditions have been marked using filled markers. Test cases have been indicated adjacent to these with the letter "C" followed by the test case number. The inset figure depicts the variation of the isobaric specific heat capacity, C_p, with temperature at relevant pressure levels.

2.8 indicates the drop in C_p that FluidProp estimated should take place across its predicted coexistence line; not the Widom line. Nevertheless, in case 3 fluoroketone is considered here to be injected under a near-critical (slightly supercritical) state compared to the published critical point. Owing to the close proximity to the critical point, large fluctuations in various thermophysical properties could be expected.

Chapter 3

Experimental Setup and Diagnostics

3.1 Experimental setup

The centrepiece of the experimental setup was the high-pressure, high-temperature vessel (or chamber) where the fluids of interest were injected. Its design is introduced first. There are several experiment subsystems that perform various functions to create the required test cases. These are described next, categorised by function. Subsequently, the diagnostics and optical setups used in the experiments are presented.

3.1.1 High pressure vessel

The experiment vessel is illustrated in Figure 3.1. The main body is made of a single block of stainless steel (numerical designation: 1.4913) and the chamber core is square in cross-section, with sides 73×73 mm^2. This is the space completely enclosed by the windows and includes an area occupied partly by the walls containing the cartridge heaters, as well as available space to be filled with the injected fluids. The innermost portion of the chamber, occupied entirely by fluids, is also square in cross section, with sides 32×32 mm^2. The domain of research interest exists inside this central area. The inner chamber is 234 mm long resulting in a total available fluid volume of about one litre. Manufacturing drawings can be found in Appendix B and provide further detail about the design of the chamber.

The interior is viewed through orthogonal window sets (the fused silica windows are 225 mm long, 32 mm wide and 20 mm thick). The windows are installed in separate steel flanges. Sealing is achieved through the use of o-rings (Barnwell, material: FFKM) that can withstand temperatures up to 300 °C. Two different gaskets are installed on the interface between each flange and the main body of the vessel. One is made of graphite (novaphit) and serves as additional pressure sealing whilst the other is made of phlogopite mica (novamica) and provides thermal insulation. Each flange is mounted onto the vessel via 28 mechanical, steel fasteners using ceramic washers to isolate further the window flanges from the heated body.

One of the flanges has a metal blank, instead of a window, with three feedthroughs (Spectite) that allow for thermocouple probes to be placed inside the chamber without breaking the pressure seal. These can be seen in Figure 3.2 at the left of the vessel.

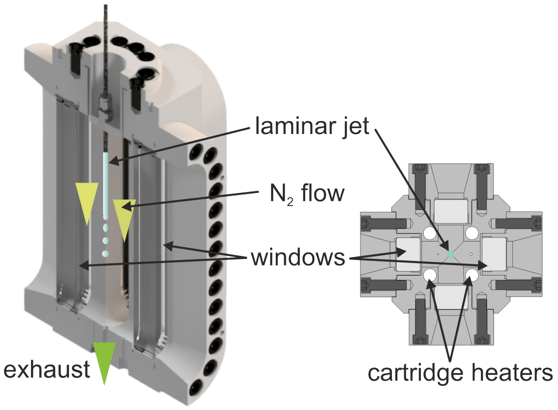

Figure 3.1: High pressure and temperature chamber: left - cut-out view, right - top section view

Four access points located around the perimeter near the top of the chamber, not shown in Figure 3.1, are used to supply high-pressure nitrogen to the vessel. Centred at the top is a capillary tube through which the laminar jet flows and is injected. There are two exhausts - one for matter in a gaseous state and one for liquid state. Matter in each of these outlets passes through their own throttle (choke) valve, before heading to the exhaust subsystem.

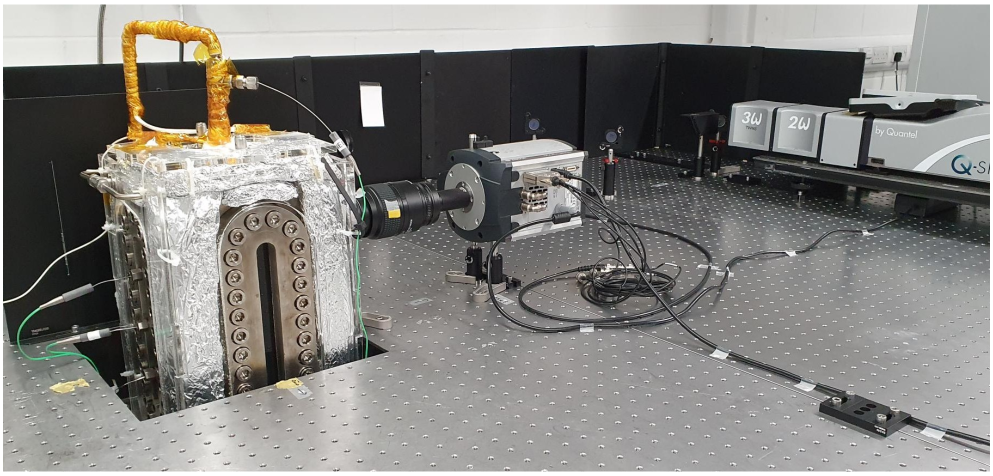

Figure 3.2: Image of high pressure chamber

3.1.2 Experiment subsystems

The experimental setup is illustrated in Figure 3.3 and Table 3.1 presents a summary of the main components, models and manufacturers (for more information most entries have been hyperlinked to the relevant manufacturer online site). The system as a whole consists of several subsystems working together, each performing a specific function. These are discussed in the following paragraphs.

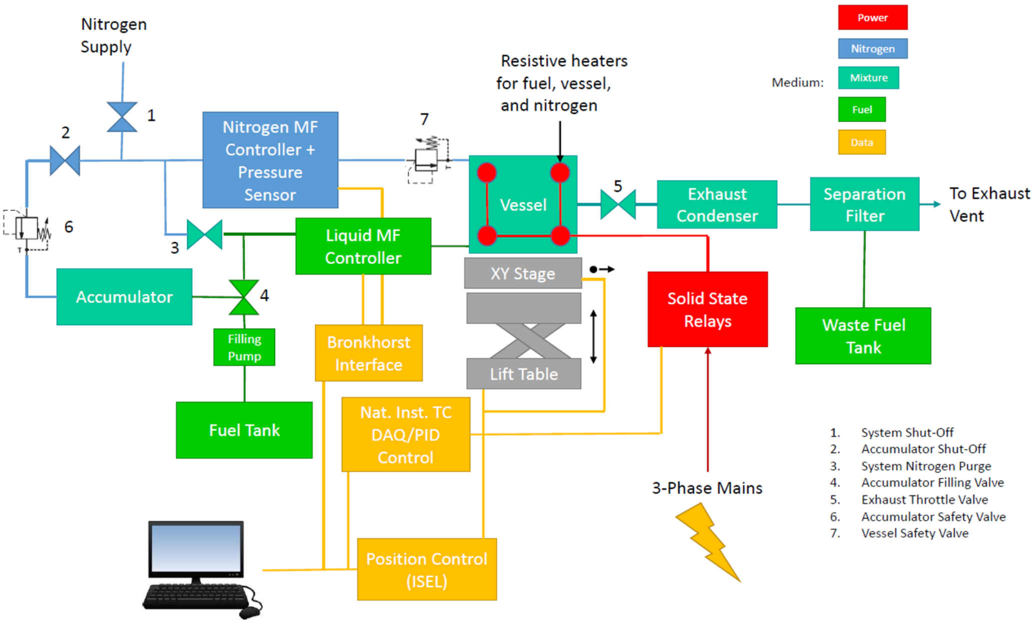

Figure 3.3: Diagram of the experiment

Chamber pressure

A flow of high-pressure nitrogen gas is used to control the pressure in the chamber. Choked-flow valves are installed downstream of the vessel, making the upstream pressure depend solely on the mass flow-rate. A mass flow controller (Bronkhorst IN-FLOW F-221MI) is used to control the mass flowrate of nitrogen. The pressure is measured just outside (downstream) of the chamber by a pressure transducer (Bronkhorst IN-PRESS P-522CI). Both of these instruments are connected to a Bronkhorst interface device (Flow Bus Terminal E-8501), which acts as their power supply, and can communicate with each other creating a control system. The nitrogen is delivered to the vessel via four access points located around the perimeter near its top. There is a constant flow of low velocity gas and the mass flow history was logged during each experiment. The chamber pressure is overall repeatable and very stable during experiments, with fluctuations being limited to as little as 0.1 bar. Pressure is assumed to be uniform within the chamber, an assumption that is valid for Mach numbers lower than 0.3. The highest Mach number was estimated to be 0.035, satisfying the condition for uniform pressure.

Chamber temperature

Cartridge heaters embedded in the vessel are used to heat the main body and interior. The thermocouple (K-type) used for the temperature control system is embedded in one of the four heaters and sends a signal to a National Instruments (NI) C Series Temperature Input Module. This, in turn, sends the temperature reading to a LabView programme located on the main desktop PC. Based on the error between the temperature reading and set-point, the programme then communicates with another NI temperature module that sends signals to four solid state relays, that are connected each of the four heaters. These effectively isolate the heaters from the 3-phase mains

Table 3.1: List of main experimental apparatus, models and their manufacturers

Component	**Model**	**Manufacturer**
ThinksStation PC Desktop	-	Lenovo
Thermoelectric cooler	MRC300-DH2-DV	Laird Technologies
Lift table	MLP-150-45	Hamaco
X-Y controller	IMC-S8	Isel
Piston accumulator	A6ES0347L2K	Parker Hiffin
Gas mass flow controller	F-221MI	Bronkhorst
Liquid mass flow controller	mini CORI-FLOW M14	Bronkhorst
Pressure transducer	IN-PRESS P-522CI	Bronkhorst
Flow bus terminal	E-8501	Bronkhorst
Liquid separator	F74C-4GD-AP0	IMI Norgren Excelon
Tube-in-tube heat exchanger	00413	Exergy LLC
Heavy duty frame	-	Thorlabs
Optical breadboard	-	Thorlabs
Temperature input module	C-series Temperature Input Module (compactDAQ)	National Instruments
Absolute origin gauge	iGaging Absolute Origin DRO	iGaging

Note: Most component names are hyperlinked to websites providing further details if needed

power supply, switching them on or off based on the instruction of the incoming signal and ultimately controlling their energy output.

The temperature inside the chamber, where the fluid is injected, is measured using three K-type thermocouples. The thermocouples all enter the chamber via one of the removable four flanges that is equipped with a metal blank (instead of a window) using Spectite feed-through assemblies. These allow the thermocouples to be inserted into the chamber without leaking under high pressure. They are spaced in the vertical direction, but in the jet plane, and are located at 40, 102.5 and 165 mm below the nozzle outlet. The thermocouple probes are flexible and so the measurement location can be varied. The reason none of these three are used as the control sensor for the heating system is because the system responsiveness is very slow. Going from room condition to the temperature required for test case 1, for example, the heater-embedded thermocouple stabilises within 15 minutes, compared to approximately 2 hours needed by the thermocouples placed inside the chamber. The reason it takes a long time for a change in the temperature setpoint to be seen inside the chamber, is because the body of the vessel is essentially a very large thermal capacitor. Therefore, even though it is the temperature inside the chamber that is of experimental interest, it is the temperature sensor embedded in the heater that is used for the control system. This raises the question of how the temperature of each test case, which requires the temperature of the chamber interior to be controlled, is achieved during an experiment.

The Proportional–Integral–Derivative (PID) controller set-points were calibrated

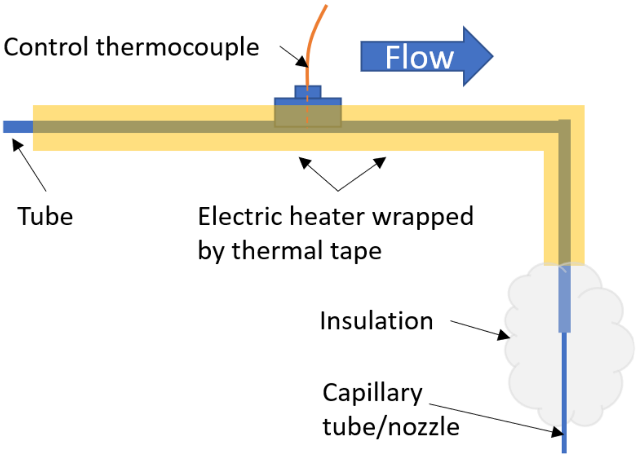

Figure 3.4: Schematic of nozzle, rope heater, control thermocouple and insulation.

so that they would produce the desired temperature reading at the first thermocouple, located approximately 40 mm below the nozzle. The chamber conditions were repeatable for each case to within a degree. Lastly, it should be mentioned that the body of the vessel is insulated with glass fibre foam. A "cage" made of acrylic plastic was manufactured that surrounds the entire chamber and is filled with thermal insulation material. The temperature was largely uniform within the chamber when no liquid was injected, with temperature drop in the vertical direction of 0.2 °C per cm, while the standard deviation in the radial direction from the jet was 2.1 °C.

Fluid injection and heating

A piston accumulator serves as the main storage tank for fluid during an experiment. One side is filled with the fluid, initially in a liquid state, and the other side is connected to the same nitrogen gas supply that pressurises the vessel. The supply of fluid to the vessel is controlled by a Bronkhorst mini CORI-FLOW™ M14 mass flow-rate controller. The pressure at the supply pressure regulator, which is the same as that for both the accumulator and the nitrogen mass flow-rate controller, is typically kept 20 bar above the required chamber pressure. Hence, the Novec inside the accumulator is also pressurised to 20 bar above the test condition. However, there is a significant pressure drop across the fluid mass flow controller. A direct measurement showed that at the output of the controller, the fluid was only slightly higher than the chamber pressure, of the order of 0.5 bar. The fluid travels via a feed tube which is a quarter-inch in diameter but is ultimately delivered through a smaller capillary tube, 0.8 mm in diameter located at the top of the chamber (centred). This is a stainless steel tube that is 102 mm long and ensures laminar flow.

The fluid injection temperature is controlled by a separate heating system. A flexible rope heater is wrapped around the final section of the fluid delivery tube. The heating arrangement is shown in Figure 3.4. A control thermocouple (K-type) measures the fluid temperature and communicates this to a PID controller (Omega engineering CN742) which in turn supplies power accordingly to the rope heater via a solid-state relay.

The control thermocouple probe is constantly present in the fluid flow, about 15 cm upstream of the nozzle. The disturbance quickly dies away and the fluid is still delivered in a laminar state. However, heat loss in the section past the thermocouple could mean the actual injection temperature is not known. Hence, a portion of the rope heater extends beyond the control sensor. This was then insulated. Measuring the temperature in real time at the tip of the injection nozzle with a thermocouple during an experiment is not possible since this would disturb the flow significantly. Instead, the temperature was calibrated at each test case by bending and placing the tip of the thermocouple closest to the nozzle inside the nozzle's outlet. The setpoint on the temperature controller was changed until the desired fluid injection temperature reading was achieved and this value was used during the final experiments (after the calibration thermocouple was removed).

Chamber positioning

Control of the chamber's physical location, relative to the static optical diagnostic system, is possible through two separate systems. A vertical stage, directly onto which the vessel sits, can be used to change the chamber elevation with displacements measured by an iGaging Absolute Origin DRO sensor. Movement in the horizontal plane is made possible through an x-y stage and controlled via an ISEL step controller (iMC-S8) through a software interface (ISEL PAL-PC).

Experiment exhaust

The nitrogen and Novec are delivered to the chamber as pure substances. However, mixing occurs within the chamber and so at the output of the vessel, the medium in the pipe network is a mixture. Novec does not pose any significant threat to humans but it can harm aquatic life. To separate it from the nitrogen and collect it for appropriate waste disposal (or recycling), a tube-in-tube heat exchanger was installed. This condenses the Novec, and a gas-liquid separation filter, placed at the very end of the setup, directs gaseous nitrogen to the ventilation and the liquefied Novec to a recycling container.

LabView programme

A programme developed in LabView is used to control and monitor the experimental setup. This is done through a graphical interface depicted in Figure 3.5.

The programme contains a PID controller used to control the heating of the chamber, and it allows the user to set the PID constants. The interface can be used to slowly ramp up the desired temperature set-point, thus avoiding spikes in the cartridge heaters' duty cycle. Additionally, it can be used to set the desired chamber pressure and the corresponding nitrogen flow-rate is displayed. Instructions can also be sent to the liquid mass flow controller to set the Novec flowrate. Chamber temperature, pressure and fluid mass flow-rates are all logged and saved to an Excel file. Novec's temperature is also logged by a separate program (Omega Engineering CN7-A) but with the same timestamp (that of the desktop PC) as the one used by LabView.

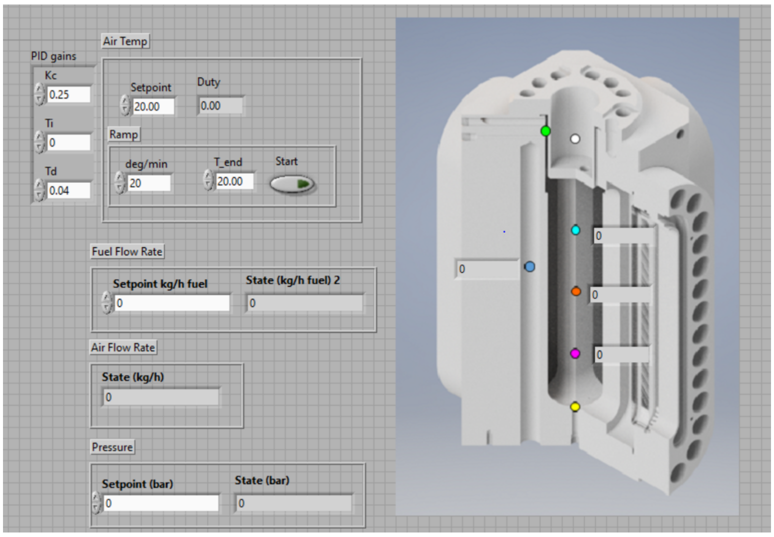

PID gains
Kc: 0.25
Ti: 0
Td: 0.04

Air Temp
Setpoint: 20.00
Duty: 0.00

Ramp
deg/min: 20
T_end: 20.00
Start

Fuel Flow Rate
Setpoint kg/h fuel: 0
State (kg/h fuel) 2: 0

Air Flow Rate
State (kg/h): 0

Pressure
Setpoint (bar): 0
State (bar): 0

0
0
0
0

Figure 3.5: LabView programme interface

3.2 Experimental challenges

Experimental work is seldom straightforward. In this project, there were many challenges that had to be addressed before measurements could be taken. A discussion of some of the main obstacles that had to be overcome may prove useful to fellow researchers currently doing related work or who may engage in similar experimental work in the future.

3.2.1 Chamber sealing

Achieving a good chamber seal is not an easy task. It is essential to ensure that there are no leaks in the system, to prevent accidents. The windows were the weakest point, with respect to leakage, in the high-pressure vessel used here. The primary mode of sealing was through the use of O-rings. The design of the windows (see Appendix B) meant that a flexible O-ring was required that could adapt to an irregular configuration; the O-ring would largely be used as a rectangular-ring in this application. Although many O-ring materials are flexible enough, it proved difficult to source ones that could also withstand high temperatures.

The only material found at the time that seemed to satisfy these requirements was Perfluoroelastomer / FFKM. These were high cost O-rings and had to be custom made in the dimensions required. Calculating these was not trivial because a balance had to be struck in choosing the amount of interference (between the window side and O-ring) and actually being able to install the window. To clarify, the O-ring, which sits in a groove that is cut into the steel flange and that runs around the perimeter of the window, has to be extruding from the groove (i.e., the O-ring's cross sectional diameter has to be larger than the groove's depth). Figure 3.6 shows the part of the metal flange where the window sits and clearly indicates where the groove is located. An interference is needed so that on installing the window, it forces the extra O-ring material back inside the groove, deforming it and achieving a seal. Finally, an interference of 0.5 mm was chosen (groove depth of 2 mm and O-ring cross sectional

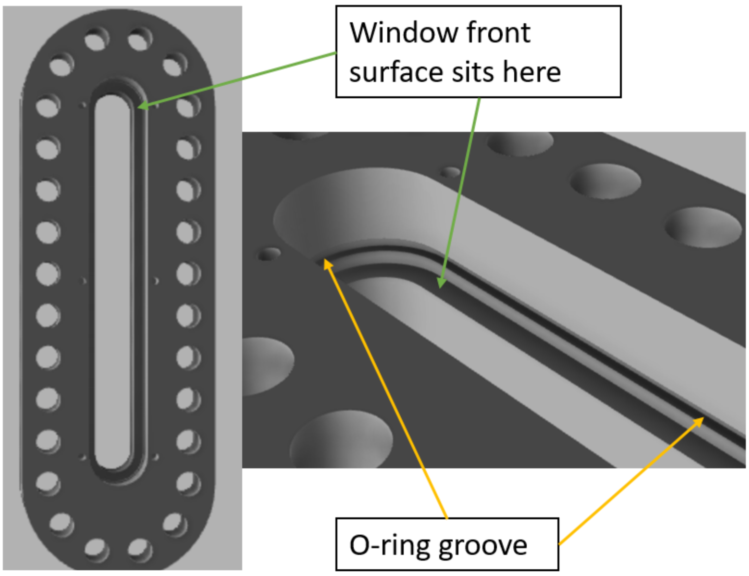

Figure 3.6: O-ring groove and window bed. Left: Top view of flange. Right: Expanded side view focusing on groove geometry

diameter of 2.5 mm) and the chamber was able to maintain high pressures.

The main problem with the 0.5 mm interference was the significant difficulty in forcing the window into its slot. With hand installation no longer possible (in contrast with previously used O-rings with minimal interference), tools had to be designed for installation and extraction of the window and O-rings. These were essentially pieces of acrylic that were placed on top of the window and could be gradually screwed toward the flange via bolts (with a fine pitch) placed around the perimeter. This resulted in the window being pushed uniformly across the O-rings in a gradual, linear motion. Even with careful installation the O-rings would occasionally be damaged. This problem was never solved; damage required replacing the O-ring with a new one.

To complicate matters further, FFKM is chemically similar to the working fluid (Novec 649). In the past, this had caused blockage of the liquid mass flow meter which used a Kalrez (FFKM based) seal, due to swelling (i.e., the seal had been absorbing some of the flowing Novec over time). This was cause for concern since the Novec might have caused swelling of the FFKM O-rings and thus be incompatible for this application. Fortunately, trial runs with FFKM O-rings installed achieved a good seal and O-rings removed at a later stage showed no signs of swelling. This was a major success since the chamber could now achieve and maintain a seal at high-temperatures. This also eliminated the need for active, local cooling near the O-rings (previously used materials could not withstand sufficiently high temperatures) that would have been achieved with a liquid cooler. The flanges have internal ducts cut into them running around the O-ring grooves, for cooling liquid to circulate and cool the O-rings to prevent them failing at high temperatures. To use the cooling circuit caused some competition between the body heating process and the flange cooling process, and the coolant lines made it difficult to move the chamber. In cases requiring very high temperature, however, the coolant could potentially be required to protect the seals.

3.2.2 Chamber heating

Heating the chamber to high-temperatures presented its own set of challenges. Test runs to establish the upper limit of temperature that the cartridge heaters could achieve showed faults in the heating system, as beyond a certain temperature the control system appeared to be failing. Essentially, the control thermocouple reading (the control thermocouple was installed inside the cartridge heater that was itself embedded in the vessel wall) would begin to fall despite the fact that the heaters were still operational. The exact nature of the fault was never established. It is still uncertain whether the heaters were also shutting down or if they would go to maximum power due to the error signal (i.e., difference between control thermocouple reading and temperature setpoint) was increasing. What was clear was that the control thermo-couple was not operating properly. Upon investigating, it was found that a thermal paste used to achieve a better thermal connection between the cartridge heater and main body of the vessel, might have been failing under the very high temperatures. It is possible that it may have been breaking down and conducting electricity. Though this was never proved, the problem was decisively solved when the cartridge heater was replaced with a new one and no thermal paste was used.

3.2.3 Piston accumulator blockage

The initial scope of the project had been to investigate a liquid hydrocarbon and acetone was being used in the fluid system. When the choice was made to switch to fluoroketone, a blockage occurred at the piston accumulator. This meant that the liquid pump used to fill the liquid side was unable to push the piston back. To complicate matters the model of piston accumulator appeared to have been discontinued by the manufacturer and they were unable to provide repair services. In collaboration with the mechanical workshop at the School of Engineering, the piston accumulator was opened and upon visual inspection it was clear that a chemical reaction had occurred between the fluoroketone and residual acetone that caused blockages. The accumulator had to be thoroughly cleaned and re-assembled. Documentation provided by the manufacturer for the accumulator was advised to re-torque it to appropriate levels. Following this maintenance procedure the accumulator could be operated normally as the piston could now slide under the action of the pump.

3.3 Diagnostics and optical setup

3.3.1 Planar laser-induced fluorescence (PLIF) and planar elastic light scattering (PELS)

DeSouza and Segal [36] have explored the photophysics of fluoroketone in detail. It can absorb laser radiation at the third harmonic of Nd:YAG (355 nm), but that wavelength is near the edge of the absorption spectrum. The fluorescence spectrum peaks near 420 nm. The absorption and emissions spectra touch in the wings but do not strongly overlap; radiative trapping of the fluorescence is not a major issue.

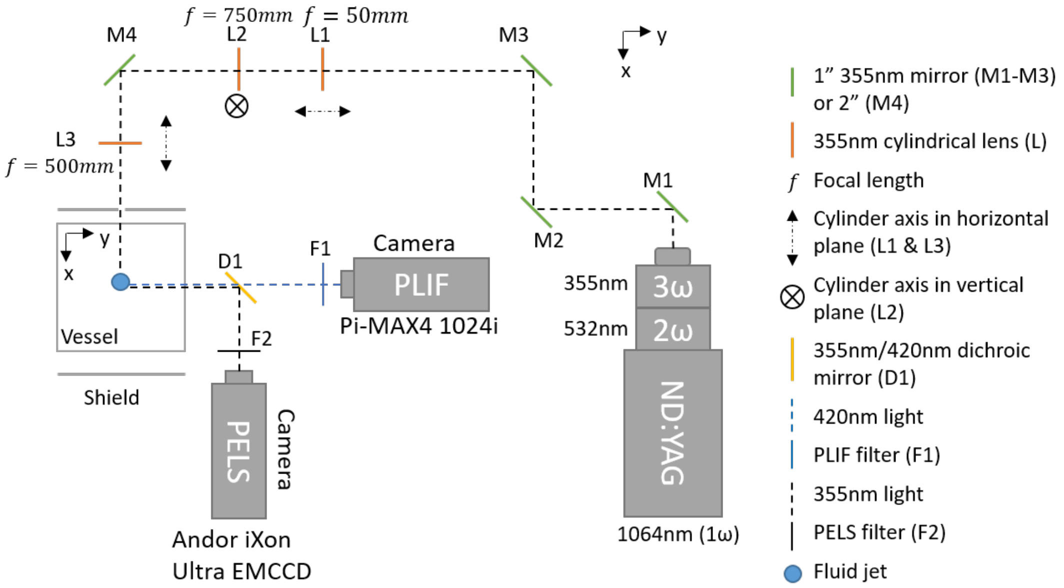

Figure 3.7: Combined PLIF and PELS optical setup

The optical setup for this study (depicted in Figure 3.7) monitored fluorescence and elastically scattered light signals simultaneously. The output of a Quantel pulsed Nd:YAG laser in the third harmonic was spread into a sheet using three cylinder lenses. The vertical dimension (40 mm) was set by a 50 mm focal length cylinder lens followed by a 500 mm focal length cylinder lens (both lenses with their cylinder axes oriented horizontally). A $\sim$ 7.9 mm thick sheet was established by a third 750 mm focal length cylinder lens (with its cylinder axis oriented vertically).The sheet thickness was measured using a WinCamD (DataRay Inc) after the sheet had passed through the input window. The WinCamD software uses a 13.5% clip level (where intensity is 13.5% of normalised peak intensity) and measures the location where the incoming beam crosses this level. Since most beams are fairly Gaussian two locations are found and the distance between them is deemed the beam width (according to the Gaussian beam formulas, see also the WinCamD user manual available at `dataray.com`). Given the width of the sheet, the entire jet was illuminated (at the nozzle the jet is 0.8 mm in diameter).

The PLIF/PELS imaging system used a 2 in. dichroic mirror in front of the exit window, reflecting 355 nm light to an Andor iXon Ultra EMCCD camera (used for PELS) and passing fluorescent light to a Princeton Instruments Pi-MAX4 1024i camera (for PLIF) equipped with a bandpass filter centred at 420 nm and a bandwidth of 10 nm FWHM. The Andor camera was fitted with a 50 mm focal length lens while the Pi-MAX was fitted with a 105 mm focal length lens. The camera images were registered to each other, but since the imaging chips have different dimensions, the exercise only ensured that we viewed the same field at similar magnification. Distances were calibrated for both cameras by imaging a high-resolution ruler located in the image plane. PLIF/PELS images presented here were taken on the jet centre-line.

Linear fluorescence (at 60 mJ per pulse, linearity was confirmed by measurement) was used because no problems with optical depth were detected during initial experiments, and linear fluorescence makes scaling more straightforward. It is assumed that the fluid exiting just at the nozzle is 100% Novec, while 0% is the background level acquired during every experiment. It is also assumed that fluorescence is linear in number density. The 100 PLIF images per test case and location were background subtracted and corrected for the laser sheet profile, which was acquired by imaging the sheet using surface scattering from a uniform, non-fluorescing card.

The sheet of laser light at 355 nm will also scatter elastically from an intact liquid interface. This signal can be used to detect when the interface is strong, when it is weakening, and when it has disappeared. Loss of interface scattering could be caused by a supercritical transition or because the liquid has vaporised entirely; this measurement alone is not sufficient to decide whether the fluid has become supercritical, but it is a contributing piece of information.

Because the subcritical jets are not optically thick, the laser sheet entered and was reflected around inside the liquid before exiting toward the camera. The camera collected image signatures of randomly varying caustics for that reason. Despite their complexity, caustics contain evidence for interface scattering. Because the jet underwent Rayleigh breakup when surface tension was present, small wave structures were developed across the interface and these structures located the strongest caustics. Under subcritical conditions, however, the Novec was vaporising so the liquid column shrank over time even in that case.

To analyse these data, 200 elastically scattered images were acquired and the background was subtracted from each of them. They were then normalised for the laser sheet profile, and an average was then calculated from all 200 images. Each radial signature at each axial position was then averaged to give an averaged scattering signal as a function of axial position.

Koller et al. [70] have demonstrated that one can infer surface tension from single-surface scattering measurements. That calculation is not appropriate in this case, however, because there are several reflections involved in the production of the PELS signal, and at each axial location it is not possible to know how many were involved. Moreover, work from this thesis has recently demonstrated that a diffuse interface, typical of the predicted interface for a transcritical jet, retains some reflectivity [32]. Reflectivity does not instantly become zero when the interface begins to degrade. For Novec, as an example, the reflectivity of a 50 nm thick diffuse interface (with nearly zero surface tension) can be around 0.055, and it doesn't reach zero until the interface is roughly 150 nm thick. In comparison, the Fresnel reflectivity for an infinitely thin Novec/N_2 interface is 0.075, which is only about 40% larger than diffuse-interface reflectivity. Once a transcritical interface begins to break down, it would no longer be possible to infer surface tension using the formalism presented by Koller et al. The fact that a weakened interface maintains reflectivity, however, explains some of the weakened PELS results to be presented subsequently.

3.3.2 Magnified PLIF

Following the PLIF and PELS experiments, a second campaign was conducted. Magnified PLIF (MPLIF) imaging with improved spatial resolution and greater magnification factor provided more detail on Novec distributions.

The optical setup for MPLIF was similar to the previous setup. The only difference was that the PELS signal was not monitored, so that the dichroic could be removed and the camera moved closer. Here, the Andor camera was used to acquire the MPLIF images (for improved spatial resolution). To improve the magnification factor macro-tubes increased the distance between the image sensor and the 105 mm focal length Nikon lens. As the camera was moved closer to the object, the depth of field was expected to be smaller. Since the laser sheet has a finite thickness, a portion of it might have extended beyond the depth of field. To avoid collecting out-of-focus fluorescent light contributions, a mechanical slit was used to ensure the laser sheet was narrower than the depth of field (the sheet had a width of 3.9 mm measured with a WinCam at the imaging location). The laser light sheet was thicker than the jet at the nozzle exit (with a diameter of 0.8 mm). Even in this case, therefore, the laser excitation and fluorescent emission were volumetric. It should also be noted that the jet will act as a plano-convex lens, refracting some light from the periphery towards the centre, and this contribution will be more noticeable in magnified images. This refraction effect was not accounted for in the analysis but will be more pronounced in sub-critical cases (more liquid like) than in supercritical states.

The original PLIF images (Figures 4.3 to 4.8) did not indicate significant absorption of laser light as it traversed the jet, and so a laser energy level ensuring that the LIF signal fell into the linear regime was chosen. Linear LIF offers advantages in terms of scaling, and in this work, the data are scaled.

The magnified PLIF images, however, contained evidence for absorption of the laser beam (approaching from the left in the MPLIF images, Figure 4.10). As an example, in the top of the transient image of Figure 4.10d, a decrease in LIF signal can be detected on the right-hand side. This issue existed primarily in the dense jets near the nozzle outlet. Despite the fact that absorption was an issue only for a small region of some flows, a scheme for correcting data was developed, starting from the nozzle exit to render all of the results more useful.

The chosen approach to correct for absorption was developed using images that were averages of 100 individual MPLIF images, and it consisted of several computational steps. It was first necessary to model the loss of laser irradiance via absorption as it passed across the jet and then to infer the effect of this diminished irradiance on the local LIF signal.

Loss of irradiation as it passes across a non-uniform distribution of mass requires application of the equation of radiative transfer (ERT). The more commonly used Beer's law does not apply in this case because it was developed assuming a uniform mass distribution. For continuous functions, absorption is modelled in the ERT using [71]

$$I(x) = I(0)\mathrm{e}^{-\tau(x)\cdot x}, \tag{3.1}$$

where $I(x)$ is the laser irradiance (W/m^2) as a function of radial position x, $I(0)$ is the input irradiance, and τ is the optical depth defined by

$$\tau(x) \equiv \int_0^x N(x')\sigma dx', \tag{3.2}$$

where $N(x')$ is the mass distribution written in the form of absorber number density, and σ is the absorption cross-section (m^2). For discrete data, such as was acquired here, the integration in equation 3.2 is replaced by a summation, with discretisation performed on a per-pixel basis.

To model LIF rigorously, based on $I(x)$, requires the solution of coupled rate equations, and the outcome can be highly uncertain. Instead, it is asserted here that LIF is linearly proportional to $I(x)$ (the LIF excitation source). It is then possible to normalise the experimental LIF profile at a specific axial location and compare it to a normalised value of $I(x)$ (from equation 3.1), since there is a direct proportionality. Once the two match, the form of $N(x')$ used in equation 3.2 then provides the profile for mass distribution which can be scaled to the actual density.

The density profile [$N(x)$] was modelled using a super-Gaussian function:

$$N(x) = N_{\mathrm{peak}} \exp[-(x-b)^2/(2c^2)]^P \tag{3.3}$$

where N_{peak} is the number density at the peak of the function, b can be used to offset the curve centre from 0 (an issue for the jets farther downstream because the jets were not perfectly vertical), c controls the width of the distribution, and P controls the shape of the curve. Example super-Gaussian curves are shown in Figure 4.11, where the density curves near the nozzle represent a nearly top-hat profile and curves farther down in the flow (axial distances 5 and 7 mm) represent a Gaussian shape. This functional dependence is justified, for application to the averaged images, by the fact that the experimental curves have these same profiles on the laser input side up to the point where absorption distorts them. Moreover, other sources (see, e.g., the Raman imaging results, Figure 1.8, by Mayer et al. [20]) indicate that a jet like this one will exit the injector tube with a nearly top-hat density profile, and it will evolve into a Gaussian profile with axial distance.

The MPLIF image correction process started at the nozzle outlet, which is a reference point because the distribution at that location was a nearly top-hat profile of pure Novec, with negligible amounts of vapour to the side. The wings of the normalised LIF distribution at that point were used to fit an initial super-Gaussian (fitting c and P). At the nozzle outlet b was set to 0. The inferred $N(x)$ distribution was then used in equations 3.1 and 3.2 to infer a normalised LIF signal. The error between the simulated LIF profile and the measured profile (both normalised to their peak values) was then minimised by adjusting c and P. Here, σ was also allowed to float because the laser sheet was thicker than the jet at the nozzle, meaning that the absorption path length varied from the jet diameter on centre-line to nearly zero in the vapour that existed well beyond the edges of the jet. The σ values inferred using this technique were significantly lower than the various published values for this reason (for liquid 0.23×10^{-20} [cm^2/molec] [38] and for vapour 38.1×10^{-20} [cm^2/molec] [72]), but the difference occurs because we use σ to account for path length variation.

There is no cross-talk among c, P and σ during minimisation because c can be set using both sides of the experimental LIF curve, P sets the width of the top of the profile, and σ controls how much the LIF signal decreases with radial distance across the distribution.

This minimisation process generated a normalised expression for $N(x)$, which was then set on an absolute mass basis using the density of Novec at the nozzle outlet, as estimated by FluidProp. This result was checked against the known mass flow rate for Novec, and the maximum error was 15.4%. The disagreement, which is one indication of the uncertainty in the correction, is a result of several factors. First, FluidProp is not entirely accurate (none of the EoS are). For example, it disagrees with the published critical temperature for pure Novec by 3.4% and with the critical pressure by 13.8%, overestimating in both cases. Next, the PLIF image near the nozzle outlet is generated by a cylindrical volume of fluid because the laser sheet illuminates the entire jet. The centre of the jet generates an LIF signal across the entire diameter while the edges generate LIF from thin regions, meaning that the centre is somewhat over-emphasised relative to the edges. These issues decrease in importance with distance downstream because the laser sheet is no longer absorbed strongly and the jet becomes wider. Uncertainties will be discussed in more detail below.

A similar process was used to extract density profiles $[N(x)]$ at downstream axial locations. Optimising b for the downstream data helped to avoid erroneous narrowing/broadening via c to account for centre-line mismatch, and it prevented non-physical solutions whereby the code would raise the signal level and apply strong absorption to achieve a better fit, precisely because of misalignment of the curve centres. Finally, the absolute mass density was inferred by scaling the downstream distribution with the LIF signals.

3.3.3 Temperature measurements

Temperature measurements were performed using thermocouples to acquire temperature maps in the injection plane. Because the flows are steady and reproducible, three thermocouples inside the chamber were used to measure the temperature at various locations. To vary the test location, the probes of the thermocouples were bent and their location monitored via images from a spatially calibrated camera looking directly at the jet plane (i.e., placed perpendicular to the plane). To ensure the thermocouple bead (approximately 0.5 mm in diameter) was in the jet plane, a second camera was used to view it end-on and the probe was rotated until the bead was seen to be on the centre-line of the injection nozzle. Radial and axial profiles of temperature were obtained.

3.4 Density measurement uncertainty

The uncertainty of the MPLIF density measurements reported in Chapter 4 was calculated by considering several factors. These included the chamber pressure, the temperature inside the nozzle tip and the application of the PC-SAFT equation of state (through FluidProp) to calculate the density at injection. The density values reported in the image plane were then linearly interpolated from this calibrated value. Thus, the error of the results depended on the accuracy of the laser sheet profile correction which was also estimated.

For the chamber pressure and injection temperature, a sensitivity study was done using FluidProp to establish how much the final density value would change based on the expected uncertainty in each of these. The combined uncertainty considering both pressure and temperature can be estimated using the method of Kline and McClintock [73]

$$U_c = \sqrt{\left(\frac{\partial \rho}{\partial T_{inj}} \cdot U_T\right)^2 + \left(\frac{\partial \rho}{\partial P} \cdot U_P\right)^2} \tag{3.4}$$

where U_c is the combined uncertainty, ρ is the density, T_{inj} is the injection temperature, U_T is the uncertainty in temperature, P is pressure and U_P the uncertainty in pressure. To estimate the combined uncertainty, the partial derivatives of density with respect to temperature and pressure had to be estimated via FluidProp. For example, the measured value of temperature at the nozzle was varied within the expected uncertainty ($2.2\ ^{\circ}C$) for each test case and then FluidProp was used to calculate the corresponding change in density, with all else being constant. The partial derivative of density with temperature was then estimated.

The same process was done for pressure. The pressure transducer used, Bronkhorst In-Press 522CI, had a published error of 0.5% of the sensor's full scale range which was 100 bar. That is, the error was a constant 0.5 bar meaning the percentage error would go down at higher experimental pressures. The sensor also had a temperature sensitivity at 0.1%, of the sensor's full scale range, per degree C. With a conservative temperature uncertainty of 2.2 °C (the temperature of the sensor would not have varied as much as at the nozzle) this was an additional constant error of 0.22 bar. The total uncertainty in pressure, under all test cases, was thus estimated to be 0.72 bar. As before, through the use of FluidProp, the pressure was varied within its uncertainty limits, and the change in density calculated.

The partial derivatives and uncertainties were used in Eq. 3.4 to estimate an uncertainty in the density. For each test case, the value was expressed as a percentage of the predicted density at the nozzle. The error associated with using an equation of state was estimated by comparing the discrepancy between the published critical density value (639.1 kg/m^3 [74]) and the critical density predicted by PC- (FluidProp) (594.9 kg/m^3). This percentage error (6.9%) was added to the combined percentage uncertainty from the temperature and pressure measurements.

Finally, the error based on the laser sheet correction was estimated by assuming an uncertainty in the location of the laser sheet profile by ± 10mm in the vertical direction and calculating the change in final density value. The laser sheet profile was not uniform and so the correction applied to each pixel was different depending on which part of the profile was considered. The final percentage errors from FluidProp and laser sheet profile uncertainty were combined by taking the square root of their sum of squares. The final uncertainty was then 8.1%, 8.5%, 8.9% and 8.9% for test cases 2,3,4 and 6 respectively (test cases 1 and 5 were omitted from the MPLIF campaign).

Chapter 4

Results

For ease of reference to the conditions of each test case, Table 2.1 is re-created here.

Test case	T_{Novec} (°C)	T_{chamber} (°C)	P_{chamber} (bar)	Description
1	160	150	16	Subcritical jet into subcritical chamber
2	190	150	16	Superheated vapor ($T > T_c$ but $P < P_c$ inside injector) into subcritical ($T_{\text{ch.}} < 170\,°\text{C}$) chamber
3	170	170	19	Critical point ($T_c\,\&\,P_c$ inside injector) into critical point ($T_{\text{ch.}} = 170\,°\text{C}$) chamber
4	160	220	16	Subcritical (inside injector) into supercritical ($T_{\text{ch.}} > 175\,°\text{C}$) chamber
5	160	220	31	Compressed liquid ($P > P_c$ but $T < T_c$ inside inj.) into supercritical ($T_{\text{ch.}} > 175\,°\text{C}$) chamber
6	190	220	31	Supercritical ($P > P_c$ and $T > T_c$, inside injector) into supercritical ($T_{\text{ch.}} > 175\,°\text{C}$) chamber

4.1 PELS results

The PELS images were analysed as described in Section 3.3, and Figure 4.1 includes the results for the six test cases provided in Table 2.1. The images were corrupted by scattering from the nozzle within the first few mm, so the PELS data start at 2.5 mm below the nozzle outlet. In Figure 4.1, one can see that there is a significant interface scattering signal for cases 1, 4 and 5. These three cases use the same temperature for the injected liquid, and it is below T_c for the pure liquid. The oscillations in cases 1 and 5 were repeatable; they were established by the wave structure in the liquid column. These wave structures, which are characteristic of the Rayleigh breakup process, are an indication that surface tension remains significant, but the structures are less pronounced in case 5 than they are in case 1. Case 4 did not have such strong wave structure or oscillations. The difference between cases 4 and 5 is that case 5 was at almost twice the pressure of case 4. The jet was therefore more dense and it had a higher boiling point. The test case 1 curve has two slopes, with a steeper slope between 2.5 and 12 mm axial distance, and a reduced slope afterwards. This happened because the average intact liquid length for that jet was 12 mm. Past that point, gaps between drops reduced the slope of the averaged curve. Note that the curve for test case 5 does not have the same change of slope, and the magnitude between 2.5 and 12 mm axial distance is fairly low compared to case 1, implying a weakening of the interface.

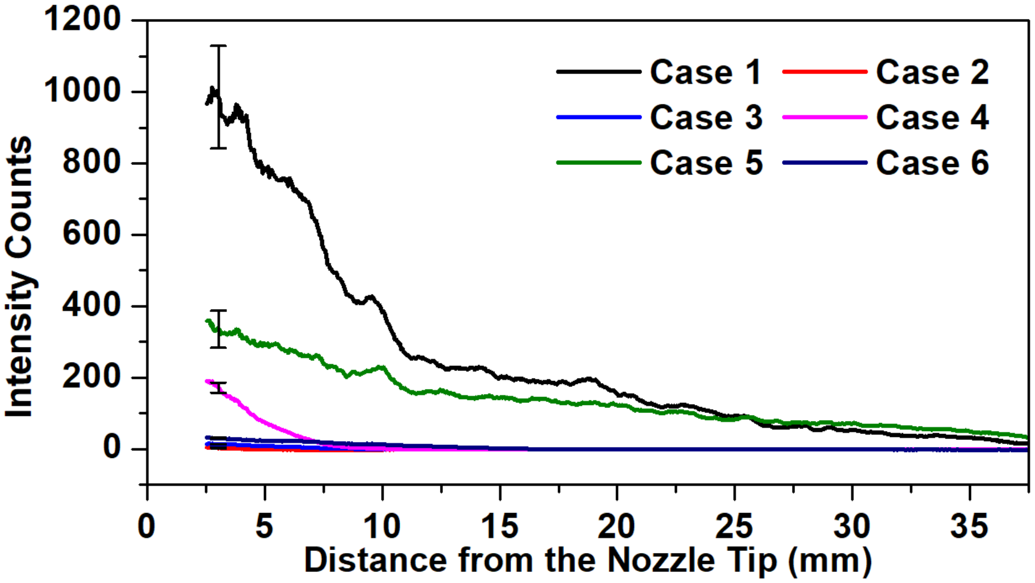

Figure 4.1: PELS results for the jets under the test cases listed in Table 2.1. The average standard deviations in the data were: $\sigma_1 = 143$, $\sigma_2 = 1.1$, $\sigma_3 = 1.4$, $\sigma_4 = 16$, $\sigma_5 = 25$, and $\sigma_6 = 2.2$.

The other cases shown used a temperature inside the injection system that was at or above T_c for the pure liquid. Those test cases exhibited no evidence of elastic scattering and it is assumed that there was no intact, thin interface.

Figure 4.1 indicates that there are characteristic rates of decay in the scattering signal (cases 1, 4 and 5). For subcritical cases, the chamber was hot enough to vaporise the liquid. Even in that case the signal decays, albeit with a long tail. The signal for case 4, however, decays faster and it goes to zero. To ascertain whether one can observe this transition changing axial location and/or rate, extra cases were added. Figure 4.2 contains curves for those extra cases, together with cases 1 and 4 as well. All four cases had the same subcritical temperature and pressure inside the liquid delivery system; the only difference between the cases was the chamber temperature. Case 1 is for a subcritical chamber temperature ($T_{\text{chamber}} < 170\,°\text{C}$). The oscillations in the signal and the long tail were a result of Rayleigh breakup, as already explained. The curve for case 1a ($T_{\text{chamber}} = 180\,°\text{C}$) has evidence for oscillations between 2.5 and 10 mm, but past that point the curve decays smoothly to zero. The other two curves ($T_{\text{chamber}} = 200$ and $220\,°\text{C}$) have few to no oscillations, and they decay more rapidly to zero. These results imply that the interface is weakening, even very near the nozzle, and it happens more rapidly as T_{chamber} increases past 200 °C. There is a reasonable chance that all of these cases were dominated by evaporation, although the rapid loss of scattering signal together with reduced oscillations as chamber temperature increases implies simultaneous weakening of the interface.

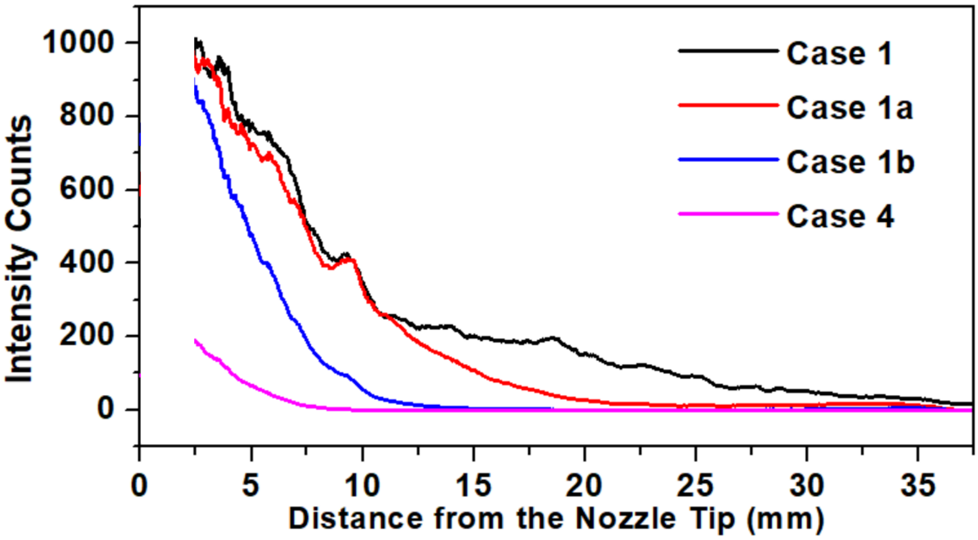

Figure 4.2: PELS results with evidence for changes in transition location and rate.

It is important to emphasise that the curves in Figure 4.2 are based on an average of 200 images, each of which have a spatial resolution of 100 μm, and there was random variation from frame to frame. As the curves drop off to zero, their shape is not representative of a liquid/gas interface. They do indicate, however, that the axial location of transition decreases as the chamber temperature is raised, and the average rate of change increases as well (it is difficult to detect rates in Figure 4.2, but the case 4 curve does decay more rapidly than the others).

The disappearance of interface scattering is certainly indicative of a vanishing, sharp interface. However, on its own it is not enough to conclude that a thermodynamic transition has taken place. Even in a fully sub-critical case, such as case 1, the signal eventually disappears due to vaporisation. Under conditions designed to create a trans-critical scenario, the interface could vanish both due to vaporising (the initially pure jet is injected at a sub-critical state) and potentially due to ‘emission’ or diffusion of molecules from the denser main body toward the ambient gas. If an equilibrium, supercritical state is established at some point, it is unclear if that point would exactly coincide with the disappearance of the interface scattering signal. Nevertheless, using a flow time defined based on the jet velocity at the nozzle, an estimate of the time required for the interface to vanish can be obtained.

The jet velocities at the nozzle for cases 1, 4, and 5 were estimated using the known mass flow-rate, the nozzle diameter, and an estimated density at the nozzle provided by FluidProp (density values at the nozzle for all cases are given in Section 4.4). The exiting jet velocity for cases 1 and 4 is approximately 1.8 m/s and for case 5 it is 0.5 m/s. Based on these velocity estimates, the jet decay time can be defined as the time required for the averaged ES intensity signal to drop from its peak value to the 20% level. For cases 1 and 4 this time is 7.0 and 2.3 ms, respectively. While this estimate is approximate (e.g. the jet velocity is not constant with axial distance) the figures demonstrate that the rate of interface decay increases going from case 1 to case 4, with cases 1a and 1b falling somewhere in between as shown in Figure 4.2. The decay in case 5 takes a significantly longer time, estimated to be 51 ms. This difference is to be expected since the case 5 jet produces a much lower peak than the jet in case 1, and beyond the 12.5 mm location their ES curves have approximately the same slope. The jets in cases 2, 3, and 6 generated no PELS signal and so they were not included in this decay time analysis.

4.2 PLIF results

Here combined PLIF and PELS images for each test case are presented. The PLIF images include one typical transient image together with an average of 100 images. The corresponding elastic scattering data are included for reference.

Figure 4.3 (case 1), for the subcritical case, shows a jet undergoing Rayleigh breakup, a clear sign of surface tension. The chamber temperature induced vaporisation while also modifying the liquid physical properties at the interface.

Figure 4.4 (case 2) images a superheated vapour jet ($T > T_c$ but $P < P_c$ inside the nozzle). The chamber temperature is below T_c for the mixture. Here the images indicate a moderately dense gas jet at the nozzle outlet; the jet is diffuse and sinuous with no evidence for Rayleigh breakup, and there is no interface scattering signal. Evidence indicates that the jet entered the chamber as a vaporising fluid. The chamber temperature was subcritical, so it is likely that a subcritical vapour would be found around and below the jet (this point is discussed further in Section 4.4).

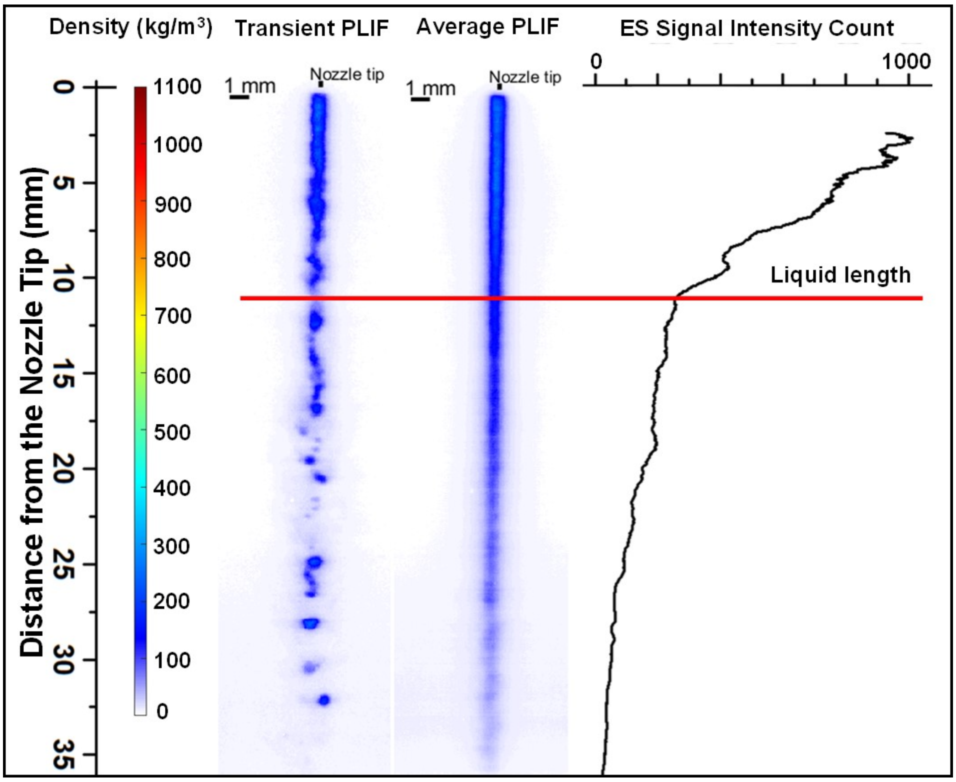

Figure 4.3: Test case 1: $T_{\text{Novec}} = 160\,^{\circ}\text{C}$ ($T_{r\,\text{Novec}} = 0.98$), $T_{\text{chamber}} = 150\,^{\circ}\text{C}$, and $P_{\text{chamber}} = 16\,\text{bar}$ ($P_{r\,\text{Novec}} = 0.85$). The 12 mm liquid length is indicated.

Test case 3 (Figure 4.5) is very close to the critical point for the pure liquid inside the nozzle and for the chamber. Holding the liquid near the critical point inside the fluid delivery system can produce an instability, although the test case 3 in Table 2.1 is stable and reproducible. When operating in the other five test cases in Table 2.1, it was found that the liquid control thermocouple (i.e., with the thermocouple placed upstream of the nozzle as depicted in Figure 3.4) was usually less than 10 °C lower than the liquid outlet temperature (there is heater tape wound around the tube in

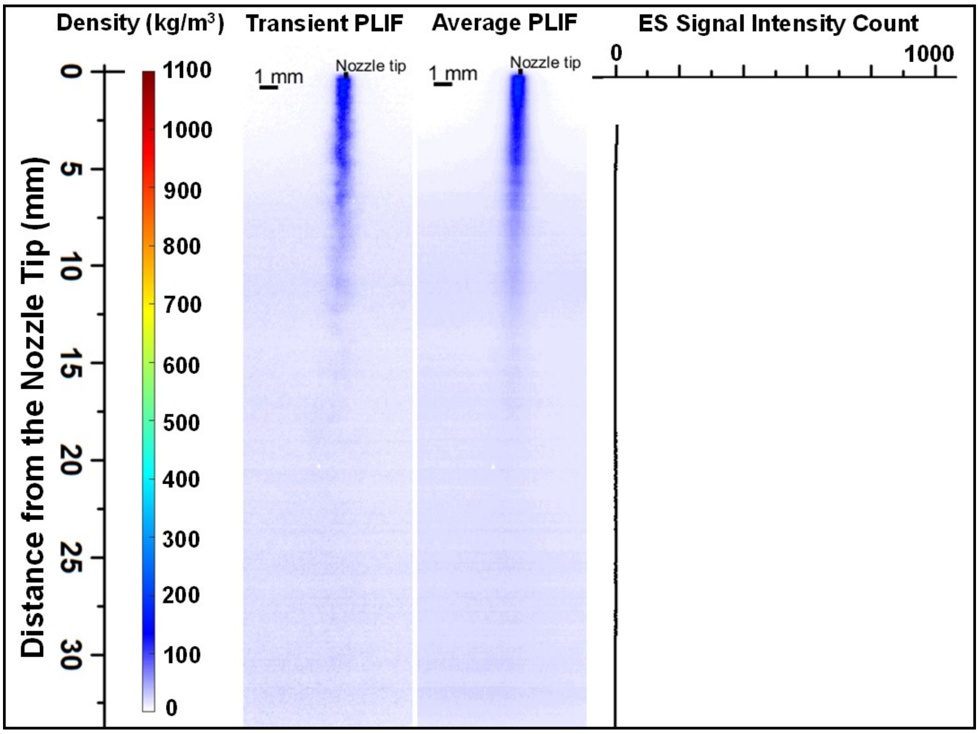

Figure 4.4: Test case 2: $T_{\mathrm{Novec}} = 190\,^{\circ}\mathrm{C}$ ($T_{r\,\mathrm{Novec}} = 1.05$), $T_{\mathrm{chamber}} = 150\,^{\circ}\mathrm{C}$, and $P_{\mathrm{chamber}} = 16$ bar ($P_{r\,\mathrm{Novec}} = 0.85$).

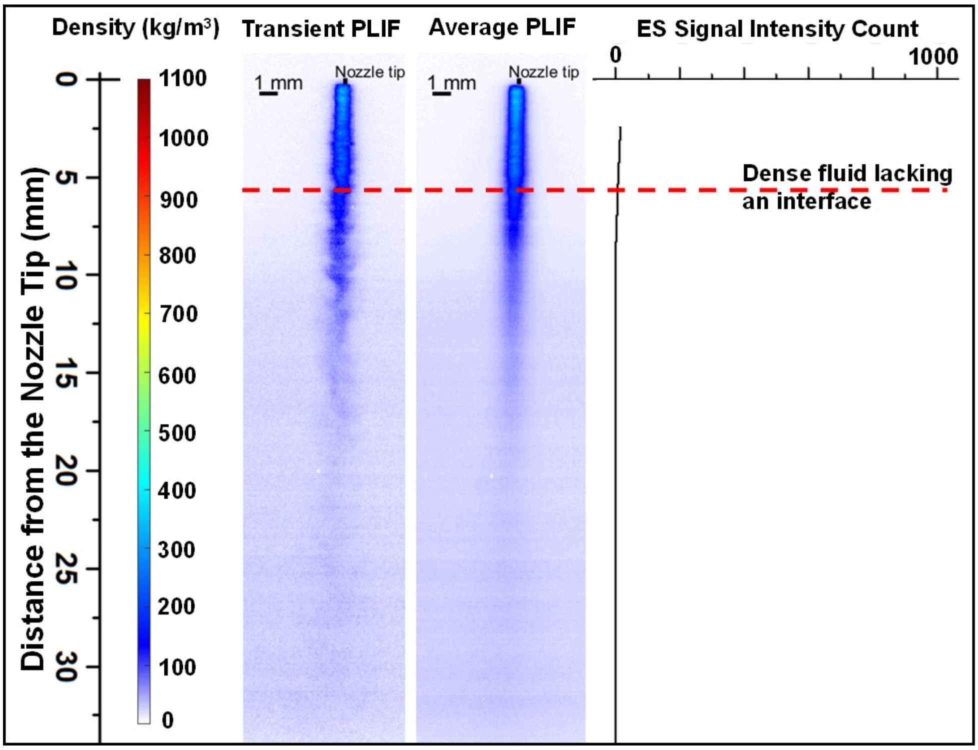

Figure 4.5: Test case 3: $T_{\mathrm{Novec}} = 170\,^{\circ}\mathrm{C}$ ($T_{r\,\mathrm{Novec}} = 1.00$), $T_{\mathrm{chamber}} = 170\,^{\circ}\mathrm{C}$, and $P_{\mathrm{chamber}} = 19$ bar ($P_{r\,\mathrm{Novec}} = 1.01$).

between the control thermocouple and nozzle outlet, so the exit temperature is always higher than the control temperature). For case 3, however, the difference could easily reach 30 °C and it could be difficult to stabilise the temperature. This observation is consistent with the findings of Fu and Lin [75], who demonstrate that the thermal conductivity of pure Novec increases rapidly to the critical point, and then just as quickly decreases past the critical point. Figure 4.5 shows a dense but diffuse, sinuous jet and it contains no evidence for Rayleigh breakup or elastic scattering.

Test case 4 (Figure 4.6) is for a subcritical pure liquid issuing into a chamber that is supercritical (based upon the VLE estimates of this work). As a reminder, states existing outside the VLE coexistence dome (where phase coexistence is not possible) are considered to be supercritical. Within the first 10 mm the PLIF image shows some very weak wave structure on the jet surface (similar to Rayleigh breakup, but it dissipates with distance) and there is an initial elastic scattering signal. Beyond that axial location, the elastic scattering signal has disappeared and the jet has become diffuse and sinuous before disappearing. Whether the Novec has evaporated or become supercritical is not clear. This jet was discussed further in the section on scattering.

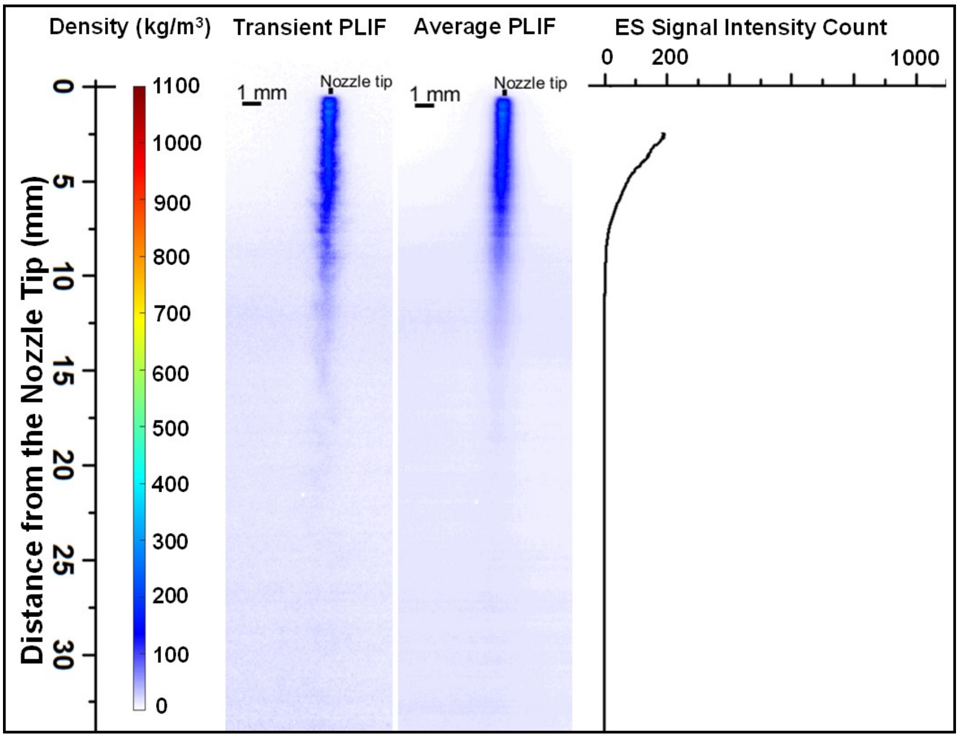

Figure 4.6: Test case 4: $T_{\text{Novec}} = 160\,°\text{C}$ ($T_{r\,\text{Novec}} = 0.98$), $T_{\text{chamber}} = 220\,°\text{C}$, and $P_{\text{chamber}} = 16\,\text{bar}$ ($P_{r\,\text{Novec}} = 0.85$).

Figure 4.7 contains data for test case 5. During these experiments, the pure Novec inside the nozzle was in the form of a compressed liquid. The chamber conditions were supercritical according to the VLE estimates of this work. The LIF signal is stronger than in the earlier cases because the jet density is higher. This jet is neither supercritical nor fully vaporised, because there is clear evidence for surface scattering and the jet is undergoing Rayleigh breakup (with a liquid length around 12 mm again).

The PELS signal is significantly lower than it was for case 1, however, indicating a weakened interface. The only difference between Figures 4.6 and 4.7 is that the data in Figure 4.7 are for a pressure that is 1.9 times the pressure of case 4 (Figure 4.6). Here, the Novec boiling point has increased with pressure, significantly reducing the rate of evaporation.

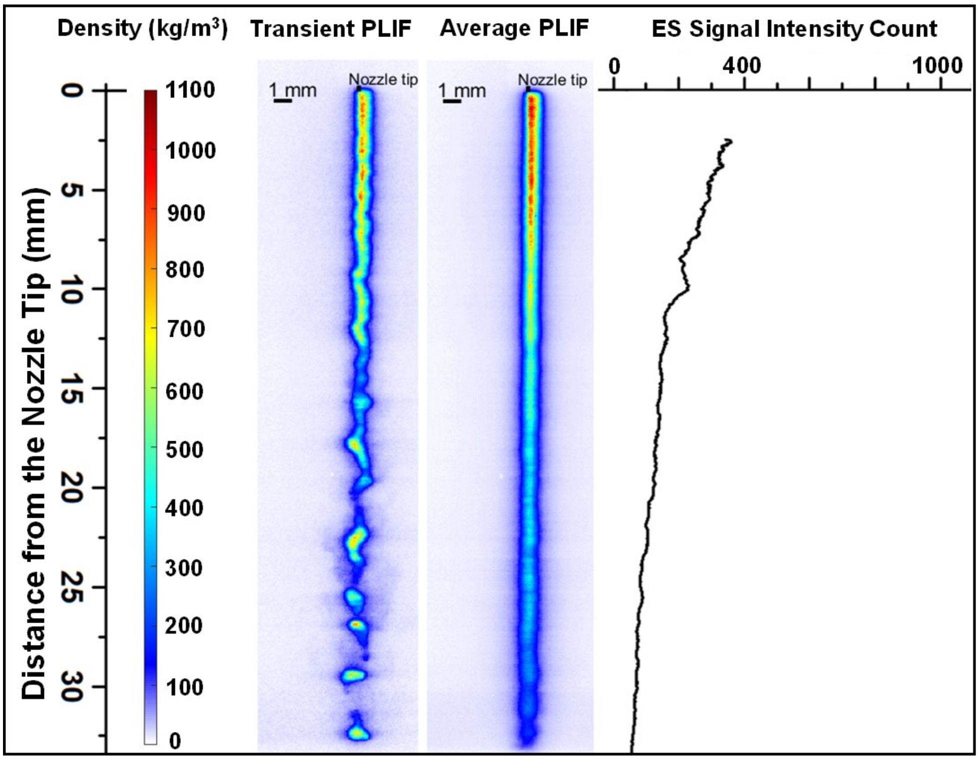

Figure 4.7: Test case 5: $T_{\text{Novec}} = 160\,^{\circ}$C ($T_{r\,\text{Novec}} = 0.98$), $T_{\text{chamber}} = 220\,^{\circ}$C, and $P_{\text{chamber}} = 31$ bar ($P_{r\,\text{Novec}} = 1.65$).

Finally, test case 6 results are shown in Figure 4.8. Here the pure Novec inside the nozzle was supercritical, while the chamber conditions were also supercritical according to VLE estimates of this work. The PLIF images imply a jet similar to that of case 5 within the first few mm, but it disappears more quickly. The scattering data indicate that there is no well-defined liquid/gas interface.

The injection temperature of the fluid jet appears to have a significant effect on the strength of its interface. For the cases where the injection temperature was below T_c for the pure fluid (for cases 1, 4, and 5) interface scattering could be detected. For the rest of the cases there was virtually no scattering signal even though a dense, gas jet could still be observed via PLIF imaging. The closest published example similar to the work presented here, is the work of Muthukumaran and Vaidyanathan [44], who also studied jets of fluoroketone injected into ambient nitrogen. A direct comparison is difficult owing to differences in the test conditions, mass flow-rates and the fact that they studied an elliptical jet, but there are certain trends in the results of this thesis that are similar. In the work of Muthukumaran and Vaidyanathan, for the sub-critical cases, Rayleigh breakup was observed. As the injection and chamber temperatures were increased, there was an observed decrease in the jet length and what was a long column of liquid transitioned into a dense gas jet. The more interesting similarity was

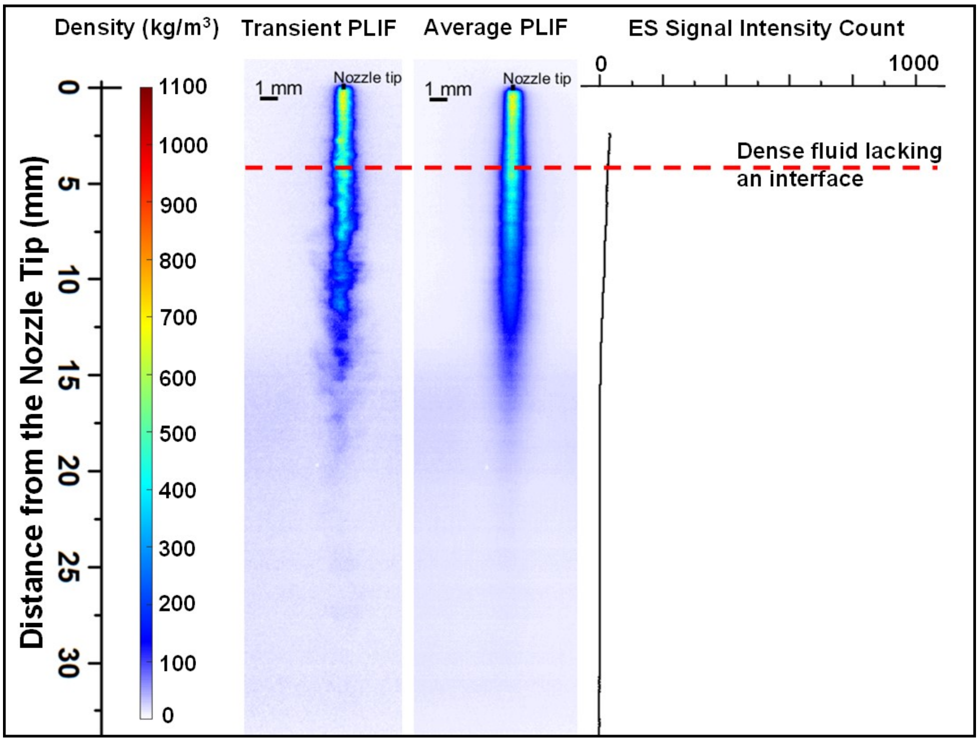

Figure 4.8: Test case 6: $T_{\mathrm{Novec}} = 190\,^{\circ}$C ($T_{r\,\mathrm{Novec}} = 1.05$), $T_{\mathrm{chamber}} = 220\,^{\circ}$C, and $P_{\mathrm{chamber}} = 31$ bar ($P_{r\,\mathrm{Novec}} = 1.65$).

the increasing presence of a sinuous feature in cases where surface tension came close to vanishing.

In a following study [30], Muthukumaran and Vaidyanathan investigated a round jet, but at a lower fluid reduced temperature of $T_r = 0.68$. The results for these jets injected into nitrogen included evidence for several propagating instabilities that depended on the thermodynamic conditions. These instabilities were observed neither in the jets considered here (minimum $T_r = 0.98$), nor in their elliptical jet study wherein the injection temperature was higher (minimum $T_r = 0.71$).

4.3 Temperature results

For both the temperature and MPLIF experiments, test cases 1 and 5 were eliminated because the other conditions presented experimentally more interesting scenarios. The temperature results are shown in Figure 4.9 as 2-D maps, in which the vertical axes represent the jet-centre axis and the nozzle tip is set as the origin $(0, 0)$. The scattered data-points on the main body of the map represent thermocouple measurement locations. The continuous line of points at the right-hand edge of each plot contains artificial data defining a boundary condition calculated as the average of the outermost measurements (radial distance > 5 mm), including at axial distances further downstream (not shown here). The maps were created in MatLab using a polynomial ('poly23') surface fit function (the standard deviations of residuals are given in Figure 4.9).

In case 2, the jet was at a supercritical temperature that was higher than the subcritical chamber temperature. As expected, the jet cooled as it flowed downwards. The ambient temperature was too high to generate detectable condensation of droplets during cooling. Figure 4.4 shows that elastically scattered light was not detected in this case.

Test case 3 was designed to maintain chamber conditions near the critical point of Novec. The goal was to keep the temperature of both the chamber and the fluid near 170 °C. Even though the temperature controller was calibrated to inject Novec at that temperature, controlling it very near the critical point was challenging. The data indicate some cooling in the jet with distance. Part of this cooling could be attributed to variations in the measurements themselves together with fluctuations in the injection and chamber temperatures.

In test case 4 the jet was injected at 160 °C. The expected observation was for the jet to be heated by the significantly hotter chamber (at 220 °C), and the jet temperature did clearly increase following injection. The disappearance of elastic scattering in Figure 4.6 occurs at approximately 7.5 mm, and a temperature of 172.5 was measured 9 mm below the nozzle. The axial distance at which the critical temperature was exceeded and the distance at which elastically scattered light became null, were similar.

For case 6, the expected observation was again for the jet to be heated by the chamber. For this case, both jet and chamber were held at temperatures higher than the critical temperature of the mixture with $T_{chamber} > T_{Novec}$. However, the thermocouple measurements indicated a reduction in temperature near the jet core. This reduction was outside the expected error in thermocouple measurements ($\pm 2.2\,°$C). The experiment was repeated over several days and each time the temperature would drop near the jet core. A physical phenomenon that would unambiguously explain the observed cooling was not identified. Thus, it remains unclear whether there is a physical explanation or if the result is erroneous; caused by the possible adverse effects that a supercritical mixture can have on a physical probe, for example owing to solubility effects. One explanation could be a change in heat capacity. As discussed previously, the thermodynamic state of Novec inside the nozzle under test case 6 is very close to the Widom line. As the fluid is heated from room temperature to near the pseudoboiling temperature, an increase in the isobaric specific heat capacity is

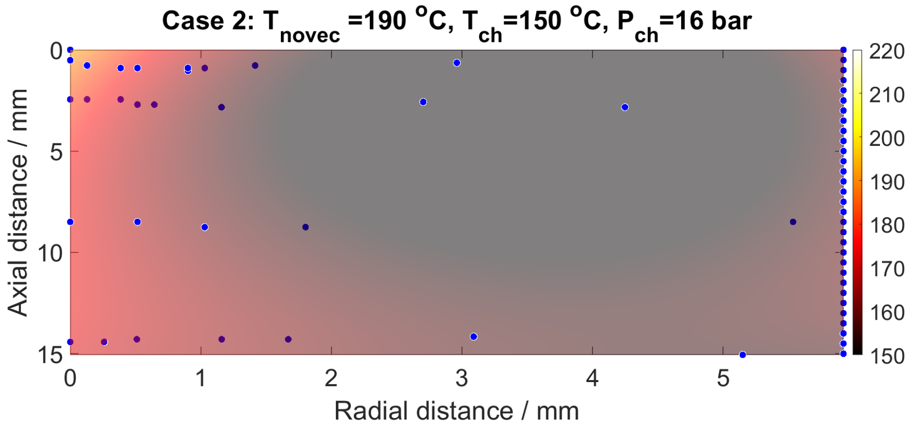
Case 2: T_{novec} =190 °C, T_{ch}=150 °C, P_{ch}=16 bar
Axial distance / mm
Radial distance / mm
0
5
10
15
0
1
2
3
4
5
220
210
200
190
180
170
160
150

(a)

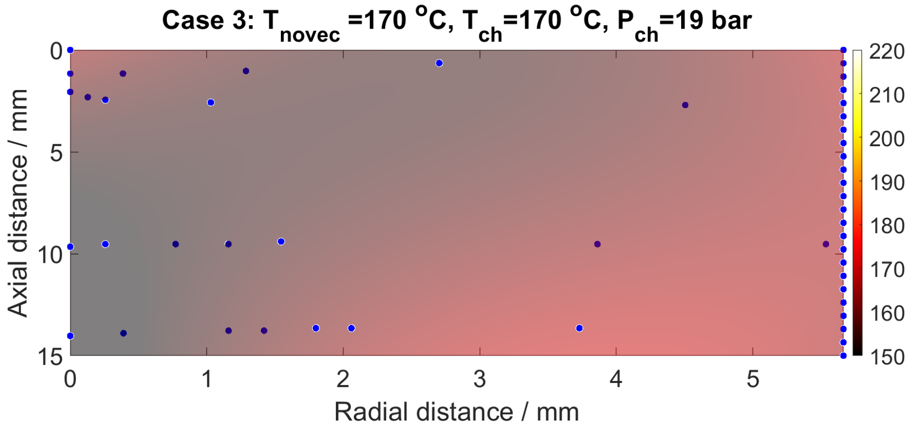
Case 3: T_{novec} =170 °C, T_{ch}=170 °C, P_{ch}=19 bar
Axial distance / mm
Radial distance / mm
0
5
10
15
0
1
2
3
4
5
220
210
200
190
180
170
160
150

(b)

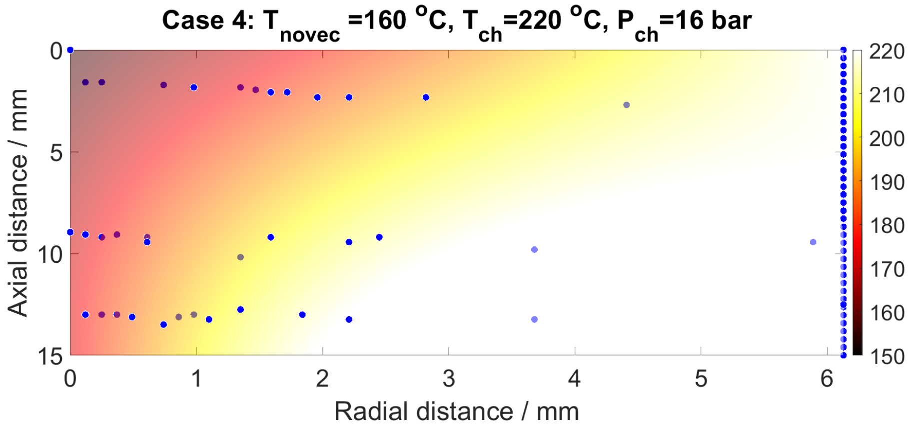
Case 4: T_{novec} =160 °C, T_{ch}=220 °C, P_{ch}=16 bar
Axial distance / mm
Radial distance / mm
0
5
10
15
0
1
2
3
4
5
6
220
210
200
190
180
170
160
150

(c)

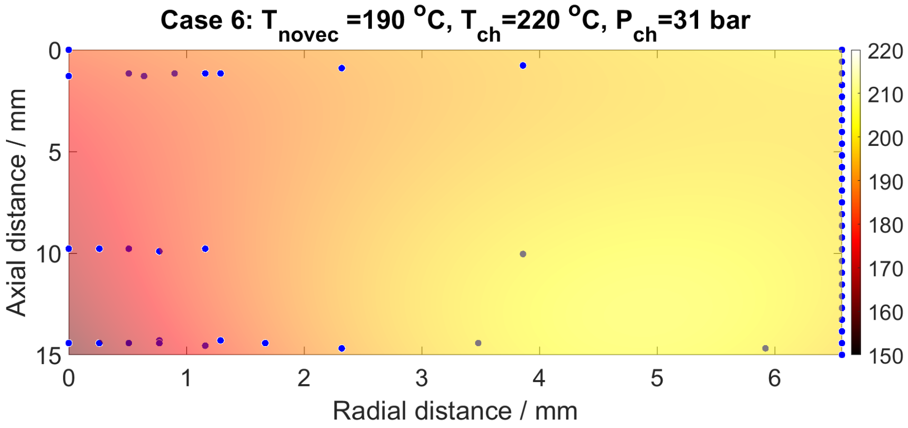

(d)

Figure 4.9: Temperature results for (a) case 2, (b) case 3, (c) case 4 and (d) case 6. The circles in the main body of the diagrams represent measurement locations. There is no difference between the bright blue data points and those that are grey. The grey points appear so because they fell under the fitted surface. Standard deviations of residuals are 5.6, 3.2, 4.3 and 4.1 °C for cases 2,3,4 and 6 respectively

expected. There is a possibility that, because FluidProp using the PC-SAFT model overestimates the critical temperature, the pseudoboiling temperature may also be overestimated. This could mean that the injection temperature might in fact fall to the right of the C_p peak, as shown in the inset plot in Figure 2.8, in the constant 31 bar $\mathrm{C}_p(T)$ curve. The significance of this is that a fall in temperature would now be accompanied by a further increase in C_p, facilitating a further drop in temperature. Note that at a reduced pressure of $P_r = 1.65$, the increase in C_p is not as profound as it might be at lower reduced pressures, but the detected drop in temperature is also fairly small.

4.4 MPLIF results

Figure 4.10 presents magnified PLIF transient and averaged images. The mixing of the fluid jet with the surrounding nitrogen, and the boundary between them, have been imaged with a spatial resolution of 17μm, providing greater detail. The average images in Figure 4.10 were corrected as described above but the transient (single) images were not. The striations in the transient cases, particularly evident in test case 6, are caused by strong absorption across the flow structures. For these cases, there was no elastic scattering signal (with the exception of case 4 where elastic scattering decays within the first 5 mm). Therefore, there is no interface to steer the light in a refractive manner. Refraction would not have been a strong effect anyway, because the laser sheet was thicker than the jet.

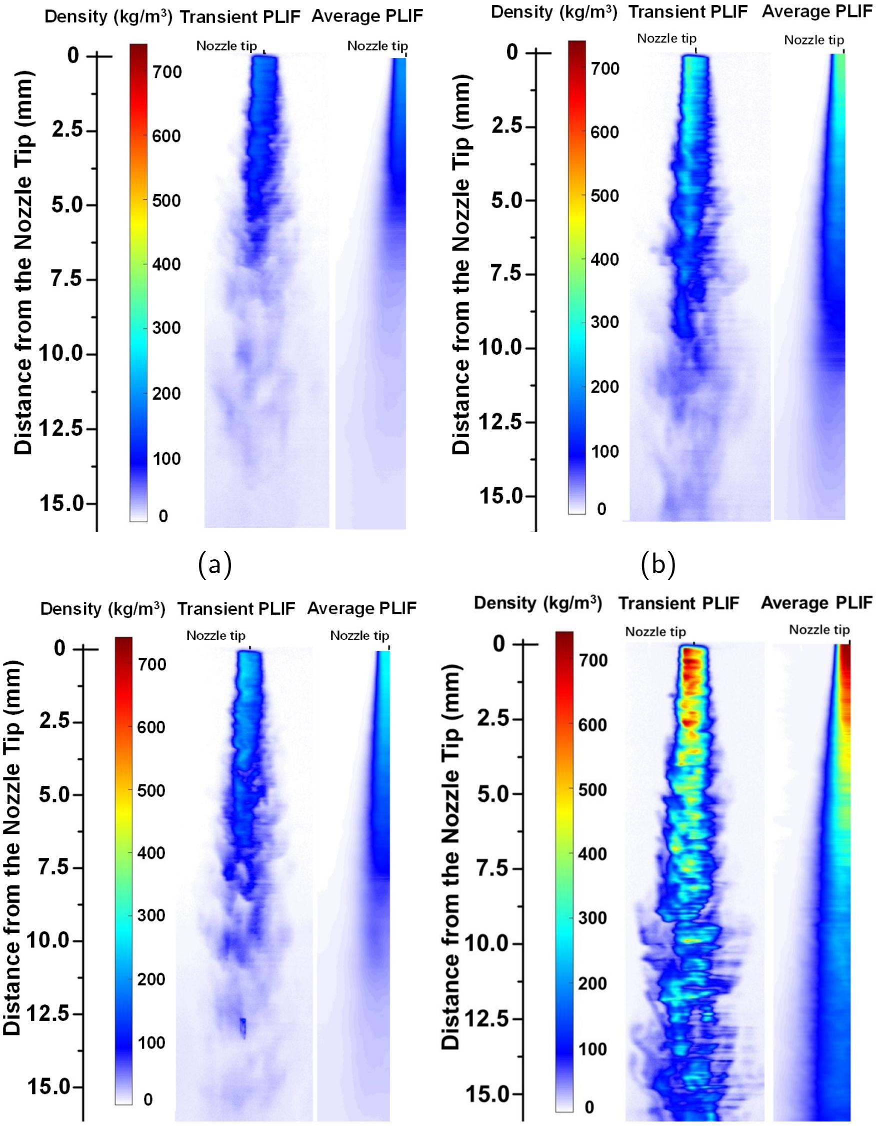

(a)

(b)

(c)

(d)

Figure 4.10: MPLIF density maps for (a) Case 2, (b) Case 3, (c) Case 4 and (d) Case 6. The laser sheet entered from the left hand side.

In Figure 4.10, case 2 achieved the shortest core length partly because it was injected as a superheated vapour with the lowest density, and because it has a higher temperature than its surroundings. There is no jet breakup because it is injected as a vapour. According to Figure 4.9, the temperature remains higher than the critical temperature near the jet axis, even beyond the point where the main jet core has disappeared. Following Banuti's four quadrant portrayal of classical pure fluid states [10], case 2 (for pure Novec) falls into quadrant 2 ($P < P_c$ and $T > T_c$). On the centre-line of the jet, at an axial distance of 8.5 mm, the temperature was measured to be 181 °C indicating that the fluid could still be in quadrant 2. By this point, the fluid is no longer entirely pure. However, superheated jets at subcritical pressure depend on diffusional mixing to transition to a mixture supercritical state when injected into fully subcritical conditions. As such, on centre-line and at an axial location of 8.5 mm, the mixing of fluoroketone and nitrogen might not have been significant enough for a transition to occur per the VLE estimates of this thesis. Moreover, by that point the jet would have become aware of the surrounding subcritical pressure (information travel via the speed of sound is faster than diffusional mixing).

Banuti [10] summarised several definitions of the pure fluid supercritical region adopted by various authors. A few of them consider quadrant 2 to be supercritical; others do not (a single phase is not necessarily supercritical). Depending on which definition is chosen, the jet in case 2 could exist as a supercritical fluid during the first few mm of its transit. If the requirement is for both P_c and T_c to be exceeded then it is highly unlikely that the fluid (pure or mixture) is supercritical in this case. The transient images show more clearly that the jet enters as a dense, sinuous gas, and the mixing process appears to include significant diffusion.

The flow structure for case 3 was similar to that observed for case 2, albeit with a significantly longer core length. The sinuous characteristic of the jet persists. As with case 2, no elastic scattering was observed, no breakup or ligaments, and the mixing process appears to include significant diffusion. Case 3 is the near-critical case relative to pure Novec where one might have expected much greater fluctuations. However, there are challenges to maintain a substance at its critical point and the chosen setpoint was one that avoided instabilities by calibrating the controller at a temperature near, but not exactly at, the pure Novec critical temperature of 169 °C.

The transient image in Figure 4.10c contains evidence for surface wave structure at the nozzle outlet (indicating some surface tension), but it dissipates with distance as the jet is heated. Case 4 is the only scenario where occasional droplets were observed. In Figure 4.10c a drop can be seen at an axial distance just after 12.5 mm, and it is clearly distinct from the surrounding vapour. It is possible that this occurred because some Novec fluid remained inside the delivery tube and it condensed. However, such droplets were not observed in case 6, which was tested soon after case 4. It is more likely that droplets appeared because case 4 has a pressure and temperature combination that corresponds to a point very close to the binodal. At an ambient pressure of 16 bar the saturated temperature is estimated, through FluidProp, to be 159.3 °C, and the injection temperature is set to 160 °C. The temperature controller was given a setpoint that ensured the jet evolved into a dense gaseous jet as opposed to a longer column of liquid. Despite the similarities in flow structure and comparable density to cases 2 and 3, case 4 was accompanied by elastically scattered light, that disappears soon after following injection.

The jet in case 6 is injected at a significantly higher density (approximately 740 kg/m^3) than the rest of the cases, giving it higher momentum than the other jets. It extends a longer distance into the chamber before dissipating and, not surprisingly, the transient image contains evidence of shear-based roll-ups along the edge. This structure is characteristic of a dense gas jet, with no surface tension.

Average density profiles for the laser-input side of the jets, found according to the description provided above and at specific axial locations, are shown in Figure 4.11. The experimental curves on the laser input side (to the right in these images) contain no indication of absorption at the edges, the super-Gaussian fits match nearly exactly there (the average disagreement is on the order of 1 to 2 % with a maximum estimated error of 5 %), and so those edges can be taken to represent reality with very low uncertainty. The locations where absorption begins to have an effect on the PLIF image change with axial distance, and they are indicated by triangles in each plot (the triangles indicate that 5% of the input irradiance has been absorbed at that radius, with absorption levels increasing to the left).

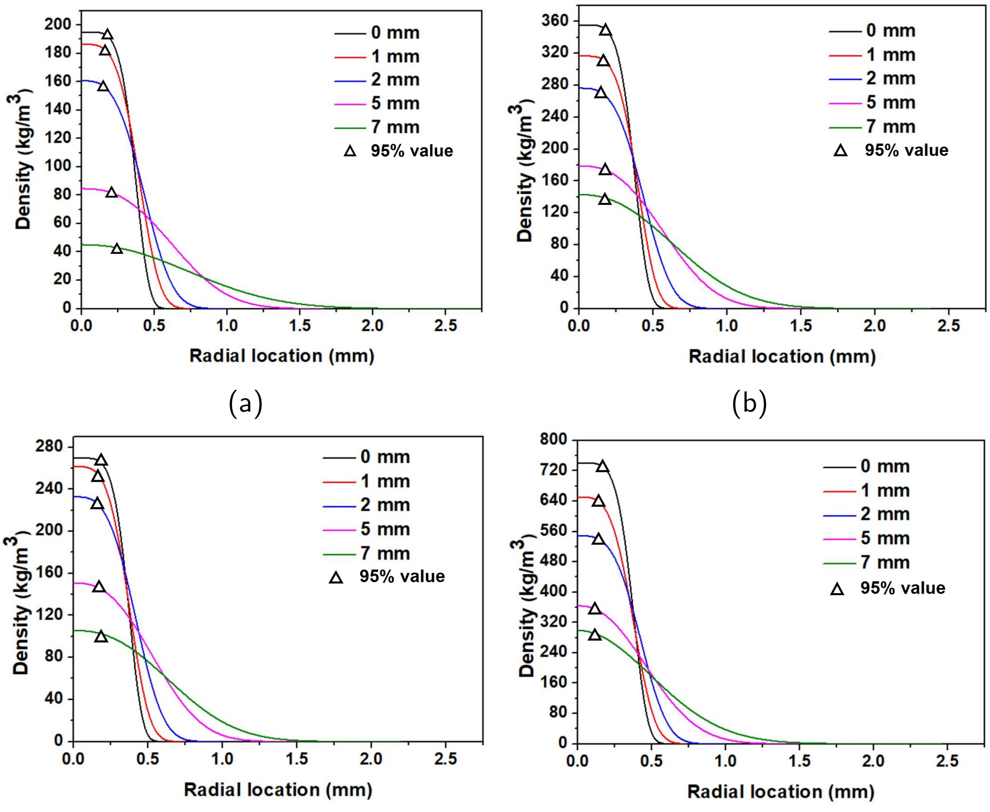

(a)

(b)

(c)

(d)

Figure 4.11: Averaged Novec density vs radial distance (the laser sheet entered from the right hand side in these plots) for (a) Case 2, (b) Case 3, (c) Case 4 and (d) Case 6. Each line corresponds to a different axial distance. The density at the nozzle was calculated using FluidProp to be 195, 356, 270 and 741 kg/m^3 for case 2,3,4 and 6 respectively

When the correction begins to have a significant effect on the curve, the combined density scaling uncertainty (based on FluidProp errors, image processing, and LIF scaling) is estimated to be 8.1%, 8.5%, 8.9% and 8.9% for cases 2, 3, 4 and 6 respectively. This estimate does not account for the fact that LIF is volumetric, causing more signal in the centre of the cylinder than at the edges. That effect would be difficult to estimate because the laser sheet is thicker than the jet diameter. Dense vapour outside of the interface would also contribute in ways that are difficult to estimate with fidelity. The previously reported 15.4 % disagreement with the mass flow meter at the nozzle is the best indicator of maximum uncertainty.

Table 4.1: Fitted (density) super-Gaussian profile parameters at chosen axial distances

Case	ρ_{peak} (kg/m^3)	N_{peak} (molecule/m^3)	c (mm)	P (...)	b (mm)
0 mm from nozzle					
2	195.1	3.72×10^{26}	0.276	2.65	0
3	355.7	6.78×10^{26}	0.280	2.60	0
4	269.8	5.14×10^{26}	0.276	2.70	0
6	741.0	1.41×10^{27}	0.280	2.55	0
1 mm from nozzle					
2	186.4	3.55×10^{26}	0.304	1.95	0
3	316.7	6.04×10^{26}	0.302	2.15	0
4	261.6	4.99×10^{26}	0.288	1.95	-0.02
6	651.1	1.24×10^{27}	0.292	1.85	-0.03
2 mm from nozzle					
2	160.7	3.06×10^{26}	0.341	1.6	-0.02
3	276.3	5.27×10^{26}	0.345	1.65	-0.02
4	232.8	4.44×10^{26}	0.331	1.65	-0.02
6	549.0	1.05×10^{27}	0.335	1.7	-0.02
5 mm from nozzle					
2	84.6	1.61×10^{26}	0.526	1.3	-0.05
3	178.8	3.41×10^{26}	0.484	1.3	-0.05
4	150.8	2.87×10^{26}	0.452	1.3	-0.07
6	364.0	6.94×10^{26}	0.416	1.15	-0.1
7 mm from nozzle					
2	45.1	8.60×10^{25}	0.685	1.1	-0.15
3	142.9	2.72×10^{26}	0.573	1.15	-0.02
4	105.7	2.01×10^{26}	0.563	1.2	-0.08
6	299.1	5.70×10^{26}	0.490	1	-0.13

The super-Gaussian parameters for the curves shown in Figure 4.11, for use in Equation 3.3, are provided in Table 4.1. If they are of interest, density gradients could be calculated radially from the nozzle centre-line at these axial locations. Close to the nozzle the fitted parameter 'b' is essentially 0. Further downstream, the centre of the fitted super-Gaussian had to be offset slightly. Values of 'b' are provided in the table. Note that this offset has been removed in the density profiles depicted in Figure 4.11, so that all curves are centred at 0.

4.5 Potential evidence for supercritical states

As already mentioned, the disappearance of an interface can be caused either by transition to a supercritical state or by evaporation. The chamber is hot enough to support evaporation, as evidenced by the test case 1, 4, and 5 curves in Figure 4.1. As liquid evaporates, however, the vapour mixes across the flow-field and the PLIF image of the remaining liquid weakens substantially. Evaporating drops have been observed at axial distances of roughly 40 mm below the nozzle exit, under case 1, with no evidence of elastic scattering at that location. The vapour has become a uniform background across the entire chamber (the entire chamber was not viewed here). Some of the test cases in this work do not exhibit those spreading trends and they may contain supercritical regions.

There are regions where the PLIF image indicates a fluid density on the same order as the subcritical density, but there is no evidence for interface scattering. Examples include the regions marked with a red dashed line in Figures 4.5 and 4.8. There is a reasonable chance that those datasets indicate a supercritical jet. Case 6 (Figure 4.8) holds all conditions above the critical point, and if any of the jets in this work were supercritical it would be this one. Those PLIF images indicate a sinuous, dense gas jet. Case 3 could potentially have supercritical locations as well, and as already discussed, case 2 has regions at high temperature that are difficult to categorise.

Chapter 5

Reflectivity of diffuse, transcritical interfaces

Analysis of experimental results obtained in this project demonstrated that diffuse, transcritical interfaces do not lose their reflective properties spontaneously once broadening of the interface reaches a level that one may consider as a transition to a supercritical state, e.g. once surface tension approaches zero [32]. This was achieved by modelling the reflectivity of various mixtures, including Novec 649 with nitrogen (the working fluid mixture used in this experimental campaign). These results branch out from the injection experiments and so a brief review of more relevant work on fluid interface reflectivity and thickness will be given here.

During elastic scattering experiments, the camera collected image signatures of caustics which were often similar in appearance to the signal generated during Interferometric Laser Imaging Droplet Sizing (ILIDS [76]). In ILIDS, scattering from the input face interferes with the first internal light to exit a drop (it is internally reflected once from the opposite surface of the drop and then refracted as it leaves the liquid and propagates towards the camera), generating an obvious fringe pattern which is a function of drop size. Thus, jet-induced caustics contain evidence of an intact interface. When surface tension was present, the jet was in the Rayleigh breakup regime, and small wave structures were developed across the interface and these structures located the strongest caustics.

When the injected fluid was supercritical inside the nozzle, and the chamber was also operating under supercritical conditions for the fluoroketone/nitrogen mixtures (based on vapor/liquid equilibrium calculations), usually no elastic scattering signal was observed (which was expected). Very infrequently, however, a random caustic would appear momentarily. The term ‘caustic’ is appropriate here due to the fact that a (striped) interference pattern could be observed, which is a distinct characteristic of such features. The caustic was always close to the nozzle exit where interfacial wave structures existed (as observed in PLIF images). An example caustic is contained in Figure 5.1. It should be noted that previously mentioned scattering from the nozzle, which corrupted near-nozzle data (section 4.1), was not imaged directly. The camera imaged stray light that originated as nozzle scattering. With the absence of drops in the near nozzle area and no elastic scattering signal (on average) the base (low) signal level was attributed to Rayleigh scattering.

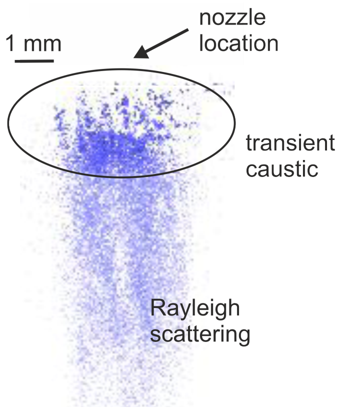

Figure 5.1: Transient image of elastic scattering from a laminar, supercritical jet of fluoroketone. Under normal circumstances one would expect to see only Rayleigh scattering. The caustic is recognizable by an interference pattern, similar to the signal produced by ILIDS. Note that under supercritical conditions, reflectivity is thought to be 10^{-7} of the reflectivity under subcritical conditions [77], which is why the signal is weak

In the discussion of the back-scattered signal produced by 'front-lighted shadowgraphy', Gerber et al. [56] mention a weakening of the signal as conditions approach and then exceed the critical point, and they discuss it in terms of strengthened Rayleigh (molecular) scattering. The laser sheet scattering experiments indicated strong Rayleigh scattering from a supercritical (i.e., very dense) jet, but the caustics were clearly caused by some other phenomenon. It was hypothesized that thin density gradients might be generated randomly by the shear-based wave structures; they could potentially generate some thin-interface reflectivity, and that could be the source of the momentary caustics. The same phenomenon could potentially be observed in other, related experiments so an investigation was warranted. The main goal in this work was twofold. The first goal was to test this hypothesis. As such, a highly accurate determination of reflectivity is unnecessary; trends can confirm the hypothesis. The second goal was to alert the community to the possibility that reflectivity may exist even when an interface has broken down.

5.1 Prior work

Gilmer et al. [78] used a treatment of electron penetration into a potential barrier by Eckart [79] to develop a theory for the reflectivity of a diffuse index gradient profile. The theory was used in conjunction with backscattering experiments. In their initial work, they studied a binary system of cyclohexane and methanol in a heated high pressure cell. They illuminated the horizontal fluid interface under nearly critical conditions, at normal incidence, using a mercury arc lamp, and then detected the reflected light. They measured reflectivity at five wavelengths using bandpass filters in front of the mercury lamp as they varied the cell thermodynamic conditions, because their theory depends upon the optical wavelength. The multiwavelength approach added fidelity to the measurements. Unfortunately, they were unable to measure reflectivity as they neared the critical point in this first experiment.

Gilmer and co-workers used Gradient Theory [80, 81] for the spatial dependence of the fluid density normal to the interface, and assumed that the index is linearly proportional to density. Their model was able to reproduce Fresnel reflection values for an infinitely thin interface, and reflectivity dropped as the interface grew in thickness. The results at the five wavelengths were consistent with each other. The approach was proposed as a means to measure the thickness of the interface, and by using their reflectivity measurements Gilmer et al. estimated a thickness on the order of 100 nm. In subsequent work, the same group [77] evaluated various models for the density distribution at the interface using the same model for reflectivity. They compared the results to similar mercury lamp experiments on the same binary mixture, but the setup had been substantially improved. This allowed them to more closely approach the critical point, but as they mention, reflectivity could be reduced by a factor of 10^{-7} going from fully subcritical to fully supercritical. This dynamic range presented a serious challenge. Meunier and Langevin [82] revisited the issue of density profiles, discussing the fact that chemical-potential-based models ignore the degradation of reflectivity based on thermal fluctuations. They proposed a modified reflectivity model that would take into account both processes (density gradient and thermal fluctuation). Unfortunately, the thermal fluctuation model required knowledge of the correlation length in the interface, and it was unknown.

5.2 Modelling reflectivity in recent experiments

In the work described here, the reflectivity models listed in Huang and Webb [77] were applied to evaluate the aforementioned hypothesis. The equations are based on various models for the density distribution in the interface, including: a linear model, exponential model, hyperbolic tangent model, and error function model. These profiles were folded into the reflectivity equation which was based upon the original work by Eckart [79], to generate four simplified models:

$$R = R_F(\sin kL \,/\, kL)^2 \tag{5.1}$$

$$R = R_F[1 \,/\, (1 + k^2L^2)]^2 \tag{5.2}$$

$$R = R_F[\pi kL \,/\, 2\sinh{(\pi kL \,/\, 2)}]^2 \tag{5.3}$$

$$R = R_F \exp{(-2k^2L^2 \,/\, \pi)} \tag{5.4}$$

where R_F is the Fresnel reflectivity (P-polarization case), and k is the average wave vector of light in the interfacial region. L is the thickness of the interface. R_F and k are given by:

$$R_F(P - polarization) = \frac{n_1 \cos\theta_2 - n_2 \cos\theta_1}{n_1 \cos\theta_2 + n_2 \cos\theta_1} \tag{5.5}$$

$$k = (n_1 + n_2)\pi/\lambda \tag{5.6}$$

where n_1 and n_2 are the refractive indices of the materials in the core and at the edge of the interface, respectively. These values were inferred here by reference to the density profiles published by Dahms and Oefelein [83] (including a 363 K liquid phase injected into 900 K, 60 bar nitrogen). The angles θ_1 and θ_2 are for incidence and refraction, and λ is the wavelength of incident light (532nm light is adopted here).

Similar to prior work, the refractive index is assumed to depend linearly on the mass density. In the optical regime, the index is also temperature dependent via temperature dependence of the molecular dipole moments, but in the case under consideration it is a lesser effect. Index is also dependent on the composition, but in this binary mixture the fluoroketone index dominates. The reflectivity calculation results are shown in Figure 5.2.

Next, various mixtures (acetone/nitrogen, hexane/ nitrogen, pentane/nitrogen, and fluoroketone/ nitrogen) were calculated assuming the same conditions reported by Dahms and Oefelein [83]. Both NIST REFPROP [84] and FluidProp [85] were used to calculate densities. The error function model (Equation 5.4) was used to calculate reflectivity for the cases shown in Figure 5.3. The goal was to infer the effect of changes in refractive index for the various fluid mixtures. Similar density profiles for each curve were assumed, which generates profiles that are similar in shape for all fluids considered.

5.3 Reflectivity modelling results

The values of reflectivity presented in Figure 5.2 clearly support the hypothesis proposed here that specific fluid dynamics can generate intermittent, thin density profiles with a finite reflectivity, even when the fluid is supercritical. While this finding does not negate the value of using average observations of scattering to identify a weakened interface, one should be aware that this phenomenon can occur.

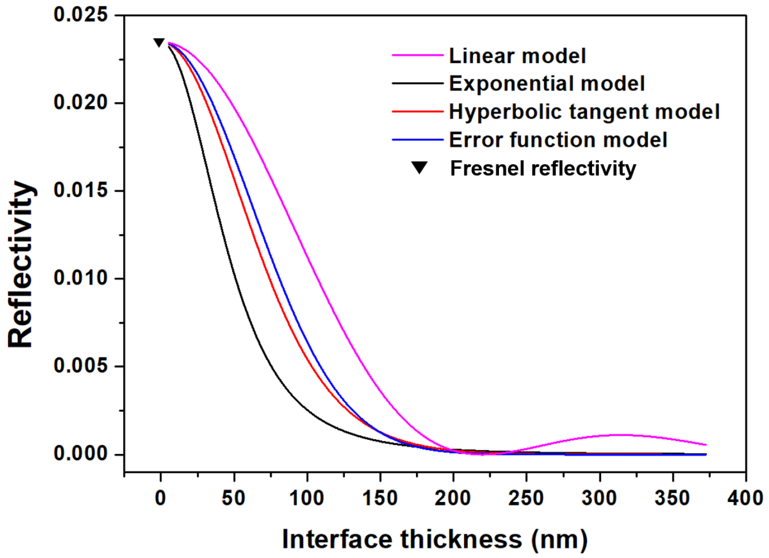

Figure 5.2: Normal incidence reflectivity of various interfaces (Dodecane/nitrogen mixture). Operating conditions: 363K liquid phase injected into $900K$ and 60 bar nitrogen

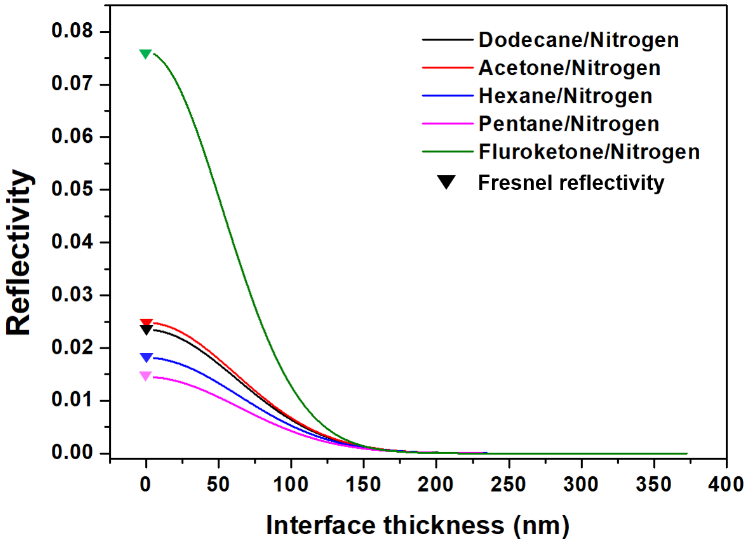

Figure 5.3: Normal incidence reflectivity for various mixtures using the error function model for the density distribution. Operating conditions: 363K liquid phase injected into $900K$ and 60 bar nitrogen

Chapter 6

Conclusion and future work

The purpose of this thesis was to conduct an experimental investigation of transcritical interfaces and report both qualitative and quantitative data. Jets of pure fluoroketone were issued into ambient nitrogen in an optically accessible vessel. To ensure the thermodynamic conditions of the chosen test cases spanned from subcritical to supercritical, VLE calculations were performed. These established the locus of VLE states for the binary mixture of fluoroketone-nitrogen and helped to identify the supercritical region. Moreover, they revealed the effect that mixing had on the critical properties of the mixture and how these differed from those of the pure components. The mixture critical pressure increases in a highly non-linear manner and, depending on mixture composition, could reach values more than an order of magnitude higher than that of pure fluoroketone.

PLIF and PELS laser diagnostics were used to study the injection process simultaneously. The former was used to obtain mixture distribution while the latter monitored the strength of the interface. The PELS signal was formed of varying caustics, owing to transmission/reflection of incoming laser light rays within the body of the jet prior to exiting. The signal was integrated in the radial direction and averaged over many frames. This was done for all rows of pixels in the longitudinal direction which resulted in a signal intensity curve that represented the strength of the interface during the time of transit of the jet. In the sub-critical case it was found that the fluid interface was scattering strongly. As the chamber temperature and pressure were increased, going toward the supercritical case, the signal intensity deteriorated. Eventually, the signal intensity became null, even near the nozzle. This demonstrated that the interface had weakened significantly and provided evidence that the interface had been destroyed. The rate of decay of the interface scattering signal meant that estimates of the temporal destruction of the interface could also be reported, given the average fluid velocity at injection.

Driven by intermittent interface scattering observed even in supercritical cases, an additional body of work was done to further investigate the reflectivity of diffuse interfaces. Through the application of reflectivity modelling, estimates were obtained for the interface reflectivity of various binary mixtures, including fluoroketone-nitrogen, as a function of interface thickness. It was demonstrated that the reflectivity may persist even beyond interface thicknesses that would indicate a transition to a supercritical state. For example, the reflectivity of fluoroketone-nitrogen has a value of about 0.075 at an interface thickness of only a few nm and this drops to approximately 0.03 once the interface has broadened to 75 nm. The reflectivity approaches 0 at interface thicknesses greater than 150 nm. There are different estimates in the literature for the width of a transcritical interface, beyond which it breaks down and surface tension can be considered null. Dahms et al. [39] estimated the maximum width of a diffuse interface to be 30 nm. While not conclusive, this estimate provides evidence that the interface may be considered destroyed (and the surface tension may become null) before reflectivity reaches zero. Intermittent interface scattering observed in the supercritical case considered in this project provides further evidence that support this hypothesis.

PLIF imaging and scaling of the data provided quantitative results of density distribution in the chamber. In all test cases PLIF images were obtained at the same time as the PELS signal. Although a jet could be seen in all test cases via PLIF, in some of the cases no PELS signal could be detected. For those test cases, the boundary identifiable in a PLIF image that separated the main jet from the ambient background gas appeared intact even though no interface scattering was detected. This showed that vital information about the interface is inaccessible due to the spatial resolution of the imaging system not being able to resolve the interface. Despite this, a magnified PLIF campaign was also done with an improved spatial resolution to provide more information about mass fraction distribution. For these experiments absorption of the laser sheet clearly affected the images so a program was developed that modelled absorption and fitted super-Gaussian profiles to the estimated, averaged density in the radial direction. Density results and super-Gaussian parameters have here been reported that may be useful for the validation of future simulation work.

Through the use of thermocouples 2-D temperature maps were obtained for a subset of chosen test cases. Temperature was measured at various locations by bending the thermocouple probes. Maps were obtained through interpolation and these revealed information about the steady state of the injection process. Pseudo-boiling effects may have been observed due to cooling of the jet following injection at the supercritical case.

6.1 Future work

This experiment has successfully provided useful data and insight into the challenging subject of transcritical fluid injection. However, measurement of a thermodynamic variable (beyond temperature and pressure) under such conditions would have given further information about the specific thermodynamic state of the fluid. Near the critical point, large fluctuations of properties occur and it would be difficult to overplay the significance of a spatially resolved measurement of one such property. An unsuccessful attempt to apply Laser Induced Grating Spectroscopy (LIGS) was made, to measure the speed of sound at this facility under the same test cases. Note that LIGS is also referred to as Laser Induced Thermal Acoustics [(LITA), see e.g., Steinhausen et al.[86]]. Although several good quality measurements were achieved, the focusing of the beams (necessary for the measurement) would very easily damage the windows, even when the laser power was well below the damage threshold of the bare glass. The problem was exacerbated due to the forming of a hardened coating on the inner face of the window owing to the presence of the injectant even after only 30 minutes of experimentation. The 355 nm wavelength pump laser beams for LITA burned the coating and that caused the beams to begin to destroy the glass surface. The same challenge was not encountered with PLIF because the laser sheets used were much larger with significantly lower energy density. One could evaluate different LITA setups that use laser pulsewidths, wavelengths, and/or power levels that avoid window damage.

In the future, to measure the sound speed, it may be necessary to consider alternative designs of the window arrangement or of the chamber entirely. In this project, the chamber that was manufactured had followed an existing design. Although this performed satisfactorily for fluoroketone, it provided numerous experimental challenges that were ultimately too serious for LITA to be effectively applied. A student working as part of the research group in Edinburgh had designed a different chamber configuration shown in Figure 6.1. In this design there is an inner core made of copper contained by an outer shell. The core is actively heated but the outer shell is not. This eases the heating power requirement since the copper body has a high conductivity and there is also a greatly reduced mass that would need to be heated. The nitrogen in the core would reach the required temperature quickly and the system would likely be much more responsive than the design used in this thesis. The vessel used in this project had acted as a large thermal capacitor which increased significantly the required time for temperature to reach steady state. Additionally, the gap between the outer shell and the core would be filled with a flow of dry nitrogen which could potentially keep the windows cleaner and prevent fluoroketone deposition.

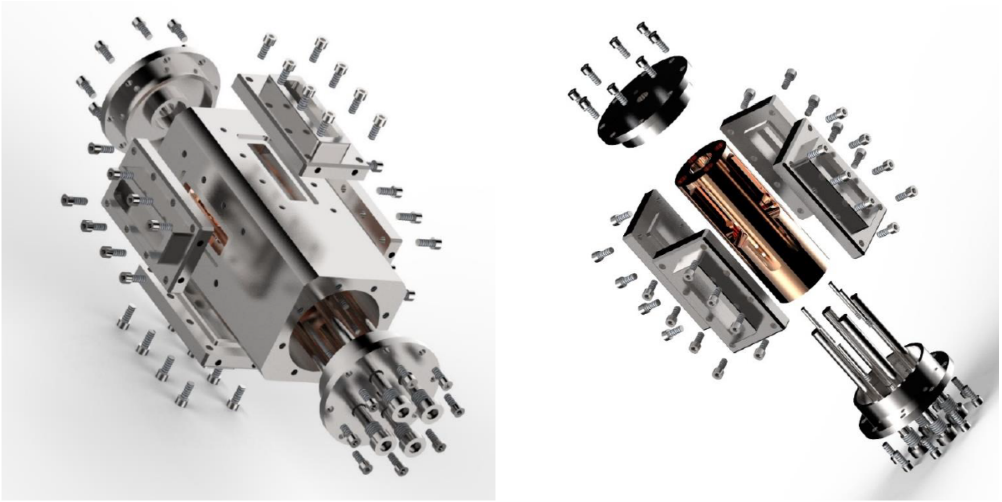

(a) (b)

Figure 6.1: Alternative chamber design showing (a) the overall model and (b) the copper core. Designed by Ralica Bencheva and professor Mark Linne.

Bibliography

[1] S. Xie, Y. Fu, P. Yi, T. Li, and R. Chen, "Evaluation of trans-critical transition of single- and multi-component sprays under diesel engine-like conditions," *Applied Thermal Engineering*, vol. 202, no. October 2021, p. 117 830, Feb. 2022, ISSN: 13594311. DOI: `10.1016/j.applthermaleng.2021.117830`.

[2] H.-O. Pörtner *et al.*, "IPCC, 2022: Climate Change 2022: Impacts, Adaptation and Vulnerability. Contribution of Working Group II to the Sixth Assessment Report of the Intergovernmental Panel on Climate Change," Intergovernmental Panel on Climate Change, Tech. Rep., 2022. DOI: `10.1017/9781009325844`. [Online]. Available: `https://www.ipcc.ch/report/ar6/wg2/`.

[3] M. Klöwer, M. R. Allen, D. S. Lee, S. R. Proud, L. Gallagher, and A. Skowron, "Quantifying aviation's contribution to global warming," *Environmental Research Letters*, vol. 16, no. 10, p. 104 027, Oct. 2021, ISSN: 1748-9326. DOI: `10.1088/1748-9326/ac286e`. [Online]. Available: `https://iopscience.iop.org/article/10.1088/1748-9326/ac286e`.

[4] A. Schwab, A. Thomas, J. Bennett, E. Robertson, and S. Cary, "Electrification of Aircraft : Challenges , Barriers , and Potential Impacts Electrification of Aircraft : Challenges , Barriers , and Potential Impacts," National Renewable Energy Laboratory, Golden, Colorado, Tech. Rep. October, 2021. [Online]. Available: `https://www.nrel.gov/docs/fy22osti/80220.pdf`.

[5] I. Staack, A. Sobron, and P. Krus, "The potential of full-electric aircraft for civil transportation: from the Breguet range equation to operational aspects," *CEAS Aeronautical Journal*, vol. 12, no. 4, pp. 803–819, Nov. 2021, ISSN: 1869-5582. DOI: `10.1007/s13272-021-00530-w`. [Online]. Available: `https://link.springer.com/article/10.1007/s13272-021-00530-w`.

[6] Air Transport Action Group, *Facts and Figures*, 2020. [Online]. Available: `https://www.atag.org/facts-figures.html`.

[7] S. Gross, "The challenge of decarbonizing heavy transport," 2020. [Online]. Available: `https://www.brookings.edu/wp-content/uploads/2020/09/FP_20201001_challenge_of_decarbonizing_heavy_transport.pdf`.

[8] R. Kamal and A. Chang, *Here's why it's so hard to electrify shipping and aviation*. [Online]. Available: `https://www.theguardian.com/environment/ng-interactive/2021/nov/11/climate-fuel-gasoline-petrol-ships-planes`.

[9] Rolls Royce, *Trent XWB*, 2022. [Online]. Available: `https://www.rolls-royce.com/products-and-services/civil-aerospace/airlines/trent-xwb.aspx#/`.

[10] D. Banuti, M. Raju, P. C. Ma, M. Ihme, and J.-P. Hickey, "Seven questions about supercritical fluids - towards a new fluid state diagram," in *55th AIAA Aerospace Sciences Meeting*, Reston, Virginia: American Institute of Aeronautics and Astronautics, Jan. 2017, ISBN: 978-1-62410-447-3. DOI: `10.2514/6.2017-1106`. [Online]. Available: `https://arc.aiaa.org/doi/10.2514/6.2017-1106`.

[11] Z. Falgout, M. Rahm, D. Sedarsky, and M. Linne, "Gas/fuel jet interfaces under high pressures and temperatures," *Fuel*, vol. 168, pp. 14–21, Mar. 2016, ISSN: 00162361. DOI: `10.1016/j.fuel.2015.11.061`. [Online]. Available: `https://linkinghub.elsevier.com/retrieve/pii/S0016236115012119`.

[12] C. Crua, J. Manin, and L. M. Pickett, "On the transcritical mixing of fuels at diesel engine conditions," *Fuel*, vol. 208, pp. 535–548, Nov. 2017, ISSN: 00162361. DOI: `10.1016/j.fuel.2017.06.091`. [Online]. Available: `https://linkinghub.elsevier.com/retrieve/pii/S0016236117308013`.

[13] L. Jofre and J. Urzay, "Transcritical diffuse-interface hydrodynamics of propellants in high-pressure combustors of chemical propulsion systems," *Progress in Energy and Combustion Science*, vol. 82, p. 100 877, Jan. 2021, ISSN: 03601285. DOI: `10.1016/j.pecs.2020.100877`. [Online]. Available: `https://linkinghub.elsevier.com/retrieve/pii/S0360128520300873`.

[14] J. Bellan, "Supercritical (and subcritical) fluid behavior and modeling: drops, streams, shear and mixing layers, jets and sprays," *Progress in Energy and Combustion Science*, vol. 26, no. 4, pp. 329–366, 2000, ISSN: 03601285. DOI: `10.1016/S0360-1285(00)00008-3`.

[15] J. Bellan, "High Pressure Flows for Propulsion Applications," in Reston VA: American Institute for Aeronautics and Astronautics Inc., 2020.

[16] M. Oschwald *et al.*, "Injection of fluids into supercritical environments," *Combustion Science and Technology*, vol. 178, no. 1-3, pp. 49–100, Jan. 2006, ISSN: 0010-2202. DOI: `10.1080/00102200500292464`. [Online]. Available: `https://www.tandfonline.com/doi/abs/10.1080/00102200500292464`.

[17] J. A. Newman and T. A. Brzustowski, "Behavior of a Liquid Jet near the Thermodynamic Critical Region," *AIAA Journal*, vol. 9, no. 8, pp. 1595–1602, Aug. 1971, ISSN: 0001-1452. DOI: `10.2514/3.49962`. [Online]. Available: `https://arc.aiaa.org/doi/10.2514/3.49962`.

[18] A. Birk, M. McQuaid, and G. Bliesener, "Reacting Liquid Monopropellant Sprays-Experiments with High Velocity Full Cone Sprays in 33 MPa, 500 Degrees C Nitrogen," Defense Technical Information Center, Tech. Rep., 1992. [Online]. Available: `https://apps.dtic.mil/sti/citations/ADA259799`.

[19] A. Birk, M. McQuaid, and M. Gross, "Liquid Core Structure of Evaporating Sprays at High Pressures - Flash X-Ray Studies," Defense Technical Information Center, Tech. Rep., 1995, p. 36. [Online]. Available: `https://apps.dtic.mil/sti/citations/ADA302618`.

[20] W. Mayer, J. Telaar, R. Branam, G. Schneider, and J. Hussong, "Raman Measurements of Cryogenic Injection at Supercritical Pressure," *Heat and Mass Transfer*, vol. 39, no. 8-9, pp. 709–719, Sep. 2003, ISSN: 0947-7411. DOI: `10.1007/s00231-002-0315-x`. [Online]. Available: `http://link.springer.com/10.1007/s00231-002-0315-x`.

[21] D. T. Banuti and K. Hannemann, "The absence of a dense potential core in supercritical injection: A thermal break-up mechanism," *Physics of Fluids*, vol. 28, no. 3, p. 035 103, Mar. 2016, ISSN: 1070-6631. DOI: `10.1063/1.4943038`. [Online]. Available: `https://aip.scitation.org/doi/10.1063/1.4943038`.

[22] W. Mayer and H. Tamura, "Propellant injection in a liquid oxygen/gaseous hydrogen rocket engine," *Journal of Propulsion and Power*, vol. 12, no. 6, pp. 1137–1147, Nov. 1996, ISSN: 0748-4658. DOI: `10.2514/3.24154`.

[23] W. O. H. Mayer *et al.*, "Atomization and Breakup of Cryogenic Propellants Under High-Pressure Subcritical and Supercritical Conditions," *Journal of Propulsion and Power*, vol. 14, no. 5, pp. 835–842, Sep. 1998, ISSN: 0748-4658. DOI: `10.2514/2.5348`. [Online]. Available: `https://arc.aiaa.org/doi/10.2514/2.5348`.

[24] M. Oschwald and A. Schik, "Supercritical nitrogen free jet investigated by spontaneous Raman scattering," *Experiments in Fluids*, vol. 27, no. 6, pp. 497–506, Nov. 1999, ISSN: 0723-4864. DOI: `10.1007/s003480050374`. [Online]. Available: `http://link.springer.com/10.1007/s003480050374`.

[25] D. T. Banuti, "Crossing the Widom-line - Supercritical pseudo-boiling," *Journal of Supercritical Fluids*, vol. 98, pp. 12–16, 2015, ISSN: 08968446. DOI: `10.1016/j.supflu.2014.12.019`. [Online]. Available: `http://dx.doi.org/10.1016/j.supflu.2014.12.019`.

[26] B. Chehroudi, D. Talley, and E. Coy, "Visual characteristics and initial growth rates of round cryogenic jets at subcritical and supercritical pressures," *Physics of Fluids*, vol. 14, no. 2, pp. 850–861, Feb. 2002, ISSN: 1070-6631. DOI: `10.1063/1.1430735`. [Online]. Available: `http://aip.scitation.org/doi/10.1063/1.1430735`.

[27] K. Harstad and J. Bellan, "Evaluation of commonly used assumptions for isolated and cluster heptane drops in nitrogen at all pressures," *Combustion and Flame*, vol. 127, no. 1-2, pp. 1861–1879, Oct. 2001, ISSN: 00102180. DOI: `10.1016/S0010-2180(01)00292-9`. [Online]. Available: `https://linkinghub.elsevier.com/retrieve/pii/S0010218001002929`.

[28] G. Lamanna *et al.*, "Laboratory Experiments of High Pressure Drops," in *High Pressure Flows for Propulsion Applications*, J. Bellan, Ed., Reston, VA: American Institute for Aeronautics and Astronautics Inc., 2020.

[29] C. Segal and S. A. Polikhov, “Subcritical to supercritical mixing,” *Physics of Fluids*, vol. 20, no. 5, p. 052 101, May 2008, ISSN: 1070-6631. DOI: `10.1063/1.2912055`. [Online]. Available: `http://aip.scitation.org/doi/10.1063/1.2912055`.

[30] C. K. Muthukumaran and A. Vaidyanathan, “Initial instability of round liquid jet at subcritical and supercritical environments,” *Physics of Fluids*, vol. 28, no. 7, p. 074 104, Jul. 2016, ISSN: 1070-6631. DOI: `10.1063/1.4954312`. [Online]. Available: `https://doi.org/10.1063/1.4954312%20http://aip.scitation.org/doi/10.1063/1.4954312`.

[31] F. J. Förster, S. Baab, C. Steinhausen, G. Lamanna, P. Ewart, and B. Weigand, “Mixing characterization of highly underexpanded fluid jets with real gas expansion,” *Experiments in Fluids*, vol. 59, no. 3, p. 44, Mar. 2018, ISSN: 0723-4864. DOI: `10.1007/s00348-018-2488-1`. [Online]. Available: `https://link.springer.com/article/10.1007/s00348-018-2488-1`.

[32] S. Yang, G. Kasapis, and M. Linne, “Reflectivity of diffuse, transcritical interfaces,” *Experiments in Fluids*, vol. 63, no. 8, p. 137, Aug. 2022, ISSN: 0723-4864. DOI: `10.1007/s00348-022-03492-9`. [Online]. Available: `https://link.springer.com/10.1007/s00348-022-03492-9`.

[33] G. Kasapis, S. Yang, Z. Falgout, and M. Linne, “A study of Novec 649 TM fluid jets injected into sub-, trans- and super-critical thermodynamic conditions using planar laser induced fluorescence and elastic light scattering diagnostics,” *Physics of Fluids*, Sep. 2022, ISSN: 1070-6631. DOI: `10.1063/5.0106473`. [Online]. Available: `https://aip.scitation.org/doi/10.1063/5.0106473`.

[34] A. Roy, C. Joly, and C. Segal, “Disintegrating supercritical jets in a subcritical environment,” *Journal of Fluid Mechanics*, vol. 717, pp. 193–202, Feb. 2013, ISSN: 0022-1120. DOI: `10.1017/jfm.2012.566`. [Online]. Available: `https://www.cambridge.org/core/journals/journal-of-fluid-mechanics/article/abs/disintegrating-supercritical-jets-in-a-subcritical-environment/7FF7744426A304EF36BC6074CACA2BC2`.

[35] S. DeSouza and C. Segal, “Sub- and supercritical jet disintegration,” *Physics of Fluids*, vol. 29, no. 4, p. 047 107, Apr. 2017, ISSN: 1070-6631. DOI: `10.1063/1.4979486`. [Online]. Available: `https://aip.scitation.org/doi/10.1063/1.4979486`.

[36] S. DeSouza and C. Segal, “Supercritical Coaxial Jet Disintegration,” in *High Pressure Flows for Propulsion Applications*, J. Bellan, Ed., Reston, VA: American Institute for Aeronautics and Astronautics Inc., 2020.

[37] J. P. R. Gustavsson and C. Segal, “Fluorescence Spectrum of 2-Trifluoromethyl-1,1,1,2,4,4,5,5,5-nonafluoro-3-pentanone,” *Applied Spectroscopy*, vol. 61, no. 8, pp. 903–907, 2007. [Online]. Available: `https://opg.optica.org/as/abstract.cfm?URI=as-61-8-903`.

[38] J. Gustavsson and C. Segal, "Characterization of a Perfluorinated Ketone for LIF Applications," in *46th AIAA Aerospace Sciences Meeting and Exhibit*, American Institute of Aeronautics and Astronautics, Reston, Virigina: American Institute of Aeronautics and Astronautics, Jan. 2008, ISBN: 978-1-62410-128-1. DOI: `10.2514/6.2008-259`. [Online]. Available: `https://arc.aiaa.org/doi/10.2514/6.2008-259`.

[39] R. N. Dahms, J. Manin, L. M. Pickett, and J. C. Oefelein, "Understanding high-pressure gas-liquid interface phenomena in Diesel engines," *Proceedings of the Combustion Institute*, vol. 34, no. 1, pp. 1667–1675, Jan. 2013, ISSN: 15407489. DOI: `10.1016/j.proci.2012.06.169`. [Online]. Available: `https://www.sciencedirect.com/science/article/abs/pii/S1540748912002775?via%3Dihub`.

[40] R. N. Dahms and J. C. Oefelein, "On the transition between two-phase and single-phase interface dynamics in multicomponent fluids at supercritical pressures," *Physics of Fluids*, vol. 25, no. 9, p. 092 103, Sep. 2013, ISSN: 1070-6631. DOI: `10.1063/1.4820346`. [Online]. Available: `http://aip.scitation.org/doi/10.1063/1.4820346`.

[41] R. N. Dahms and J. C. Oefelein, "Liquid jet breakup regimes at supercritical pressures," *Combustion and Flame*, vol. 162, no. 10, pp. 3648–3657, Oct. 2015, ISSN: 00102180. DOI: `10.1016/j.combustflame.2015.07.004`. [Online]. Available: `https://linkinghub.elsevier.com/retrieve/pii/S0010218015002059`.

[42] R. N. Dahms, "Understanding the breakdown of classic two-phase theory and spray atomization at engine-relevant conditions," *Physics of Fluids*, vol. 28, no. 4, pp. 1–44, 2016, ISSN: 10897666. DOI: `10.1063/1.4946000`. [Online]. Available: `http://dx.doi.org/10.1063/1.4946000`.

[43] C. K. Muthukumaran and A. Vaidyanathan, "Experimental study of elliptical jet from sub to supercritical conditions," *Physics of Fluids*, vol. 26, no. 4, p. 044 104, Apr. 2014, ISSN: 1070-6631. DOI: `10.1063/1.4871483`. [Online]. Available: `http://aip.scitation.org/doi/10.1063/1.4871483`.

[44] C. K. Muthukumaran and A. Vaidyanathan, "Experimental study of elliptical jet from supercritical to subcritical conditions using planar laser induced fluorescence," *Physics of Fluids*, vol. 27, no. 3, 2015, ISSN: 10897666. DOI: `10.1063/1.4916344`. [Online]. Available: `https://doi.org/10.1063/1.4916344`.

[45] J. Manin, M. Bardi, L. Pickett, R. Dahms, and J. Oefelein, "Microscopic investigation of the atomization and mixing processes of diesel sprays injected into high pressure and temperature environments," *Fuel*, vol. 134, pp. 531–543, Oct. 2014, ISSN: 00162361. DOI: `10.1016/j.fuel.2014.05.060`. [Online]. Available: `https://linkinghub.elsevier.com/retrieve/pii/S0016236114005225`.

[46] G. Mo and L. Qiao, "A molecular dynamics investigation of n-alkanes vaporizing into nitrogen: transition from subcritical to supercritical," *Combustion and Flame*, vol. 176, pp. 60–71, Feb. 2017, ISSN: 00102180. DOI: `10.1016/j.combustflame.2016.09.028`. [Online]. Available: `https://linkinghub.elsevier.com/retrieve/pii/S001021801630298X`.

[47] J.-P. Hickey and D. M. Ihme, "Supercritical mixing and combustion in rocket propulsion," Center for Turbulence Research, Stanford, Tech. Rep., 2013. [Online]. Available: `http://www.dl.edi-info.ir/Supercritical%20mixing%20and%20combustion%20in%20rocket%20propulsion.pdf`.

[48] R. S. Miller, K. G. Harstad, and J. Bellan, "Direct numerical simulations of supercritical fluid mixing layers applied to heptane-nitrogen," *Journal of Fluid Mechanics*, vol. 436, pp. 1–39, 2001, ISSN: 00221120. DOI: `10.1017/S0022112001003895`.

[49] J. Bellan, "Theory, modeling and analysis of turbulent supercritical mixing," *Combustion Science and Technology*, vol. 178, no. 1-3, pp. 253–281, 2006, ISSN: 00102202. DOI: `10.1080/00102200500292241`.

[50] G. Castiglioni and J. Bellan, "On models for predicting thermodynamic regimes in high-pressure turbulent mixing and combustion of multispecies mixtures," *Journal of Fluid Mechanics*, vol. 843, pp. 536–574, 2018, ISSN: 14697645. DOI: `10.1017/jfm.2018.159`.

[51] G. Xiao, K. H. Luo, X. Ma, and S. Shuai, "A molecular dynamics study of fuel droplet evaporation in sub- and supercritical conditions," *Proceedings of the Combustion Institute*, vol. 37, no. 3, pp. 3219–3227, 2019, ISSN: 15407489. DOI: `10.1016/j.proci.2018.09.020`. [Online]. Available: `https://linkinghub.elsevier.com/retrieve/pii/S1540748918306254`.

[52] S. Baab, F. J. Förster, G. Lamanna, and B. Weigand, "Speed of sound measurements and mixing characterization of underexpanded fuel jets with supercritical reservoir condition using laser-induced thermal acoustics," *Experiments in Fluids*, vol. 57, no. 11, p. 172, Nov. 2016, ISSN: 0723-4864. DOI: `10.1007/s00348-016-2252-3`. [Online]. Available: `http://link.springer.com/10.1007/s00348-016-2252-3`.

[53] C. Steinhausen *et al.*, "Experimental Investigation of Droplet Injections in the Vicinity of the Critical Point: A comparison of different model approaches," in *Proceedings ILASS–Europe 2017. 28th Conference on Liquid Atomization and Spray Systems*, Valencia: Universitat Politècnica València, Sep. 2017, ISBN: 9788490485804. DOI: `10.4995/ILASS2017.2017.4635`. [Online]. Available: `http://ocs.editorial.upv.es/index.php/ILASS/ILASS2017/paper/view/4635`.

[54] A. Preusche, A. Dreizler, C. Steinhausen, G. Lamanna, and R. Stierle, "Non-invasive, spatially averaged temperature measurements of falling acetone droplets in nitrogen atmosphere at elevated pressures and temperatures," *The Journal of Supercritical Fluids*, vol. 166, p. 105 025, Dec. 2020, ISSN: 08968446. DOI: `10.1016/j.supflu.2020.105025`. [Online]. Available: `https://www.`

sciencedirect.com/science/article/abs/pii/S089684462030276X?via%3Dihub.

[55] B. Bork, A. Preusche, F. Weckenmann, G. Lamanna, and A. Dreizler, "Measurement of species concentration and estimation of temperature in the wake of evaporating n-heptane droplets at trans-critical conditions," *Proceedings of the Combustion Institute*, vol. 36, no. 2, pp. 2433–2440, 2017, ISSN: 15407489. DOI: `10.1016/j.proci.2016.07.037`. [Online]. Available: `https://linkinghub.elsevier.com/retrieve/pii/S1540748916302954`.

[56] V. Gerber, S. Baab, F. J. Förster, H. Mandler, B. Weigand, and G. Lamanna, "Fluid injection with supercritical reservoir conditions: Overview on morphology and mixing," *The Journal of Supercritical Fluids*, vol. 169, p. 105 097, Feb. 2021, ISSN: 08968446. DOI: `10.1016/j.supflu.2020.105097`. [Online]. Available: `https://linkinghub.elsevier.com/retrieve/pii/S089684462030348X`.

[57] T. C. Klima, A. Peter, S. Riess, M. Wensing, and A. S. Braeuer, "Quantification of mixture composition, liquid-phase fraction and - temperature in transcritical sprays," *The Journal of Supercritical Fluids*, vol. 159, p. 104 777, May 2020, ISSN: 08968446. DOI: `10.1016/j.supflu.2020.104777`. [Online]. Available: `https://linkinghub.elsevier.com/retrieve/pii/S0896844620300280`.

[58] G. G. Simeoni *et al.*, "The Widom line as the crossover between liquid-like and gas-like behaviour in supercritical fluids," *Nature Physics*, vol. 6, no. 7, pp. 503–507, Jul. 2010, ISSN: 1745-2473. DOI: `10.1038/nphys1683`. [Online]. Available: `https://www.nature.com/articles/nphys1683`.

[59] V. V. Brazhkin, Y. D. Fomin, A. G. Lyapin, V. N. Ryzhov, and K. Trachenko, "Two liquid states of matter: A dynamic line on a phase diagram," *Physical Review E*, vol. 85, no. 3, p. 031 203, Mar. 2012, ISSN: 1539-3755. DOI: `10.1103/PhysRevE.85.031203`. [Online]. Available: `https://link.aps.org/doi/10.1103/PhysRevE.85.031203`.

[60] D. Bolmatov, V. V. Brazhkin, and K. Trachenko, "Thermodynamic behaviour of supercritical matter," *Nature Communications*, vol. 4, pp. 1–7, 2013, ISSN: 20411723. DOI: `10.1038/ncomms3331`. [Online]. Available: `http://dx.doi.org/10.1038/ncomms3331`.

[61] W. C. Reynolds and P. Colonna, *Thermodynamics. Fundamentals and engineering applications / William C. Reynolds, Piero Colonna.* Cambridge: Cambridge University Press, 2018, ISBN: 9781139050616.

[62] P. H. Van Konynenburg and R. L. Scott, "Critical lines and phase equilibria in binary van der Waals mixtures," *Philosophical Transactions of the Royal Society of London. Series A, Mathematical and Physical Sciences*, vol. 298, no. 1442, pp. 495–540, 1980, ISSN: 0080-4614.

[63] R. J. Sadus, "Calculating critical transitions of fluid mixtures: Theory vs. experiment," *AIChE Journal*, vol. 40, no. 8, pp. 1376–1403, Aug. 1994, ISSN: 0001-1541. DOI: `10.1002/aic.690400810`. [Online]. Available: `https://onlinelibrary.wiley.com/doi/10.1002/aic.690400810`.

[64] W. C. Reynolds and P. Colonna, "Thermodynamic Properties of Multicomponent Fluids," in *Thermodynamics*, Cambridge University Press, Sep. 2018, ch. 8, pp. 194–232. DOI: `10.1017/9781139050616.010`. [Online]. Available: `https://www.cambridge.org/highereducation/books/thermodynamics/4F53402087B26F32BC8DC00DEE5ED068?chapterId=CBO9781139050616A089#contents`.

[65] M. Linnemann and J. Vrabec, "Vapor-Liquid Equilibria of Nitrogen + Diethyl Ether and Nitrogen + 1,1,1,2,2,4,5,5,5- Nonafluoro-4-(trifluoromethyl)-3-pentanone by Experiment, Peng-Robinson and PC-SAFT Equations of State," Lehrstuhl für Thermodynamik und Energietechnik, Universität Paderborn, Tech. Rep., pp. 1–16. [Online]. Available: `https://www.thermodynamik.tu-berlin.de/fileadmin/fg103/Publikationen/2017_N2_Novec549-1.pdf`.

[66] J. Gross and G. Sadowski, "Perturbed-Chain SAFT: An Equation of State Based on a Perturbation Theory for Chain Molecules," *Industrial & Engineering Chemistry Research*, vol. 58, no. 14, pp. 5744–5745, Apr. 2019, ISSN: 0888-5885. DOI: `10.1021/acs.iecr.9b01515`. [Online]. Available: `https://pubs.acs.org/doi/10.1021/acs.iecr.9b01515`.

[67] M. L. Michelsen and J. M. Mollerup, *Thermodynamic Models: Fundamentals & Computational Aspects*. Tie-Line Publications, 2007, ISBN: 9788798996132. [Online]. Available: `https://books.google.com.cy/books?id=qjme0gAACAAJ`.

[68] J. W. Gibbs, *On the Equilibrium of Heterogeneous Substances, Collected Works*, 1928.

[69] D.-y. Peng and D. B. Robinson, "A rigorous method for predicting the critical properties of multicomponent systems from an equation of state," *AIChE Journal*, vol. 23, no. 2, pp. 137–144, Mar. 1977, ISSN: 0001-1541. DOI: `10.1002/aic.690230202`. [Online]. Available: `https://onlinelibrary.wiley.com/doi/10.1002/aic.690230202`.

[70] T. M. Koller *et al.*, "Liquid Viscosity and Surface Tension of n -Dodecane, n -Octacosane, Their Mixtures, and a Wax between 323 and 573 K by Surface Light Scattering," *Journal of Chemical & Engineering Data*, vol. 62, no. 10, pp. 3319–3333, Oct. 2017, ISSN: 0021-9568. DOI: `10.1021/acs.jced.7b00363`. [Online]. Available: `https://pubs.acs.org/doi/10.1021/acs.jced.7b00363`.

[71] M. Linne, *Spectroscopic Measurement: an Introduction to the Fundamentals*. Amsterdam: Academic Press, 2002.

[72] A. Roy, "Subcritical and supercritical fuel injection and mixing in single and binary species systems," Ph.D. dissertation, University of Florida, Jan. 2012.

[73] S. J. Kline, "Describing uncertainty in single sample experiments," *Mech. Engineering*, vol. 75, pp. 3–8, 1953.

[74] M. O. McLinden, R. A. Perkins, E. W. Lemmon, and T. J. Fortin, "Thermodynamic properties of 1,1,1,2,2,4,5,5,5-nonafluoro-4-(trifluoromethyl)-3-pentanone: Vapor pressure, (p, ρ, T) behavior, and speed of sound measurements, and an equation of state," *Journal of Chemical and Engineering Data*, vol. 60, no. 12, pp. 3646–3659, 2015, ISSN: 15205134. DOI: `10.1021/acs.jced.5b00623`.

[75] B.-R. Fu and W.-J. Lin, "Supercritical heat transfer of NOVEC 649 refrigerant in horizontal minichannels," *International Communications in Heat and Mass Transfer*, vol. 117, p. 104 740, 2020.

[76] R. Ragucci, A. Cavaliere, and P. Massoli, "Drop Sizing by Laser Light Scattring Exploiting Intensity Angular Oscillation in the mie regime," *Particle & Particle Systems Characterization*, vol. 7, no. 1-4, pp. 221–225, 1990, ISSN: 09340866. DOI: `10.1002/ppsc.19900070136`. [Online]. Available: `https://onlinelibrary.wiley.com/doi/10.1002/ppsc.19900070136`.

[77] J. S. Huang and W. W. Webb, "Diffuse Interface in a Critical Fluid Mixture," *The Journal of Chemical Physics*, vol. 50, no. 9, pp. 3677–3693, May 1969, ISSN: 0021-9606. DOI: `10.1063/1.1671613`. [Online]. Available: `http://aip.scitation.org/doi/10.1063/1.1671613`.

[78] G. H. Gilmer, W. Gilmore, J. Huang, and W. W. Webb, "Diffuse Interface in a Critical Fluid Mixture," *Phys. Rev. Lett.*, vol. 14, no. 13, pp. 491–494, Mar. 1965. DOI: `10.1103/PhysRevLett.14.491`. [Online]. Available: `https://link.aps.org/doi/10.1103/PhysRevLett.14.491`.

[79] C. Eckart, "The Penetration of a Potential Barrier by Electrons," *Physical Review*, vol. 35, no. 11, pp. 1303–1309, Jun. 1930, ISSN: 0031-899X. DOI: `10.1103/PhysRev.35.1303`. [Online]. Available: `https://link.aps.org/doi/10.1103/PhysRev.35.1303`.

[80] J. D. Van der Waals, "Square gradient model," *Verhandel. Konink. Akad. Weten. Amsterdam*, vol. 1, no. 8, p. 56, 1893.

[81] J. W. Cahn and J. E. Hilliard, "Free Energy of a Nonuniform System. I. Interfacial Free Energy," *The Journal of Chemical Physics*, vol. 28, no. 2, pp. 258–267, Feb. 1958, ISSN: 0021-9606. DOI: `10.1063/1.1744102`. [Online]. Available: `http://aip.scitation.org/doi/10.1063/1.1744102`.

[82] J. Meunier and D. Langevin, "Optical reflectivity of a diffuse interface," *Journal de Physique Lettres*, vol. 43, no. 6, pp. 185–191, 1982, ISSN: 0302-072X. DOI: `10.1051/jphyslet:01982004306018500`. [Online]. Available: `http://www.edpsciences.org/10.1051/jphyslet:01982004306018500`.

[83] R. N. Dahms and J. C. Oefelein, "Non-equilibrium gas–liquid interface dynamics in high-pressure liquid injection systems," *Proceedings of the Combustion Institute*, vol. 35, no. 2, pp. 1587–1594, 2015, ISSN: 15407489. DOI: `10.1016/j.proci.2014.05.155`. [Online]. Available: `https://linkinghub.elsevier.com/retrieve/pii/S1540748914001588`.

[84] E. W. Lemmon, M. L. Huber, and M. O. McLinden, "NIST standard reference database 23," *Reference fluid thermodynamic and transport properties (REFPROP), version*, vol. 9, 2010.

[85] P. Colonna and T. P. Van der Stelt, *FluidProp:a program for the estimation of thermo physical properties of fluids*, Delft, 2004.

[86] C. Steinhausen, V. Gerber, A. Preusche, B. Weigand, A. Dreizler, and G. Lamanna, "On the potential and challenges of laser-induced thermal acoustics for experimental investigation of macroscopic fluid phenomena," *Experiments in Fluids*, vol. 62, no. 1, p. 2, Jan. 2021, ISSN: 0723-4864. DOI: `10.1007/s00348-020-03088-1`. [Online]. Available: `https://link.springer.com/10.1007/s00348-020-03088-1`.

Appendix A

Heat transfer to sphere of Novec

A simple heat transfer model was used to estimate the length needed for a sphere of Novec (about 1 mm in diameter) to be heated from a subcritical to a supercritical temperature. A Nusselt number relation is used in the following code to model heat transfer to a sphere of Novec that is free falling in an environment filled with high-pressure and temperature nitrogen. The MatLab script presented below was used simply for a sanity check, i.e. to ensure a reasonable rate of heat transfer to Novec could be expected and that a thermodynamic transition within the chamber used for the experiments of this thesis was possible. The drop was given an initial temperature that was subcritical and a final temperature above the critical temperature of the mixture.

```
%% Sphere heat transfer problem
close all;clear variables;clc;

%% Declaration of variables

%-----------NOVEC 649-----------

% Drop initial temperature in [K]
T_i = 433;
% Drop diameter in [m]
D = 0.001;
% Drop final temperature in [K]
T_f = 445;
% Drop density [kg/m^3]
rho_D = 1600;
% Specific heat capacity [J/kg-K]
c_D=1103;
% Thermal conductivity [W/m-K]
k_D=0.059;
%Dynamic viscosity in [Pa-s]
mhu_D=0.00064;

%-----------NITROGEN-----------

% Ambient temperature in [K]
T_N = 493;
% Ambient pressure in [bar]
```

```
P_N = 30;

% Nitrogen properties obtained at T and P given above
% Nitrogen density in [kg/m^3]
rho_N = 20.37555;
% Kinematic viscosity [m^2/s]
v_N=1.2897145e-6;
% Dynamic viscosity in [Pa-s]
mhu_N=26.000705e-6;
% Thermal diffusivity in [m^2/s]
alpha_N = 17.94055e-7;
% Specific heat capacity at constant pressure in [J/kg-K]
Cp_N=1070.382;
% Thermal conductivity in [W/m-K]
k_N = alpha_N*Cp_N*rho_N;
% Prandtl number [-]
Pr_N = 0.71851685;

%Dynamic viscosity at sphere surface temperature
mhu_N_D = 23.79036e-6;

%--------OTHER CONSTANTS--------

% Gravitational acceleration constant in []
g=9.81;

%% Velocity of droplet

% [kg/s]
maximum_liquid_mass_flowrate = 30 ...
    /3600;

% [-]Percentage of max flowrate
mass_flowrate_percentage = 0.03;

 % [kg/s]
liquid_mass_flowrate = ...
    mass_flowrate_percentage * maximum_liquid_mass_flowrate;

% [m] Liquid injector radius
r_f = D/2;

% [m^2]
injector_area = pi.*r_f^(2);

% [mm/s]
u_D = ...
    liquid_mass_flowrate/(rho_D * injector_area);

%% Reynolds, Nusselt number and heat transfer coefficient

% Reynold's number
Re_D = (u_D*D)/(v_N);

% Nusselt number
Nu_D = ...
```

```
    2+((0.4*(Re_D)^(0.5)+0.06*(Re_D)^(2/3))*((Pr_N)^(0.4))*(...
    mhu_N/mhu_N_D)^(1/4));

% % Nusselt number 2 - sphere in convective flow
% Nu_D = 2+0.4*((Re_D)^(0.5))*((Pr_N)^(1/3));

% Heat transfer coefficient
 h = (Nu_D*k_N)/(D);

%% Lumped capacitance method for time of flight calculation

t = ((rho_D*c_D*D)/(6*h))*(log((T_i-T_N)/(T_f-T_N)));

L = u_D*t;

%% Check validity of lumped capacitance method

Bi=(h*(D/6))/k_D;
```

Appendix B

Chamber drawings

In the following pages drawings of the chamber have included that provide more detail into it design. The drawings included are for:

1. The main vessel body
2. The removable metal flange that houses the windows and metal blank
3. The metal blank with thermocouple feedthroughs
4. The vessel Lid
5. The fused silica window

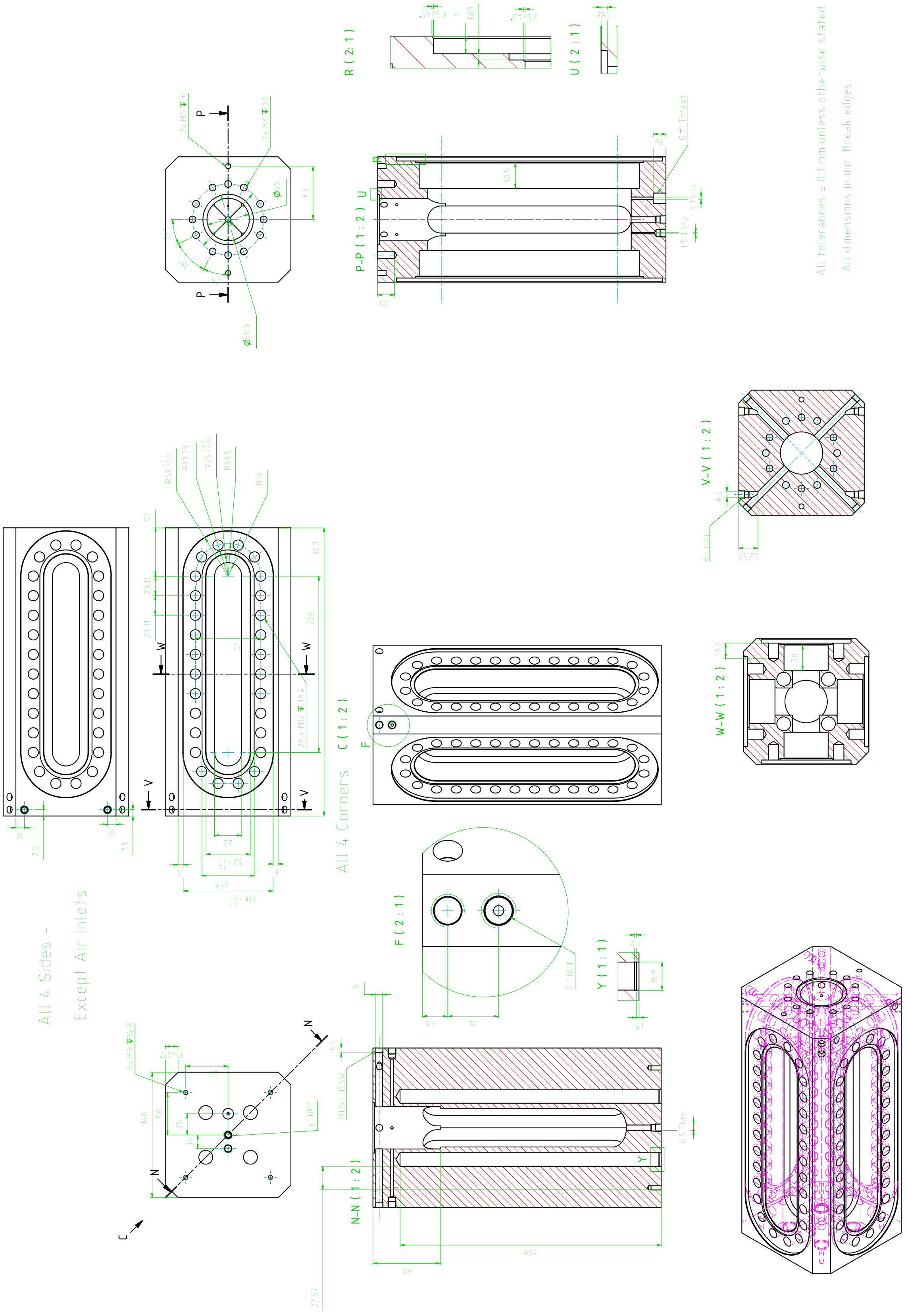
R (2 : 1)
U (2 : 1)
P–P (1 : 2)
U
P
P
V–V (1 : 2)
W–W (1 : 2)
C (1 : 2)
F
All 4 Corners
F (2 : 1)
Y (1 : 1)
N–N (1 : 2)
N
N
C
W
W
V
V
All 4 Sides -
Except Air Inlets
All tolerances ± 0.1 mm unless otherwise stated
All dimensions in mm. Break edges
NPT
Thread
Thru
808
80

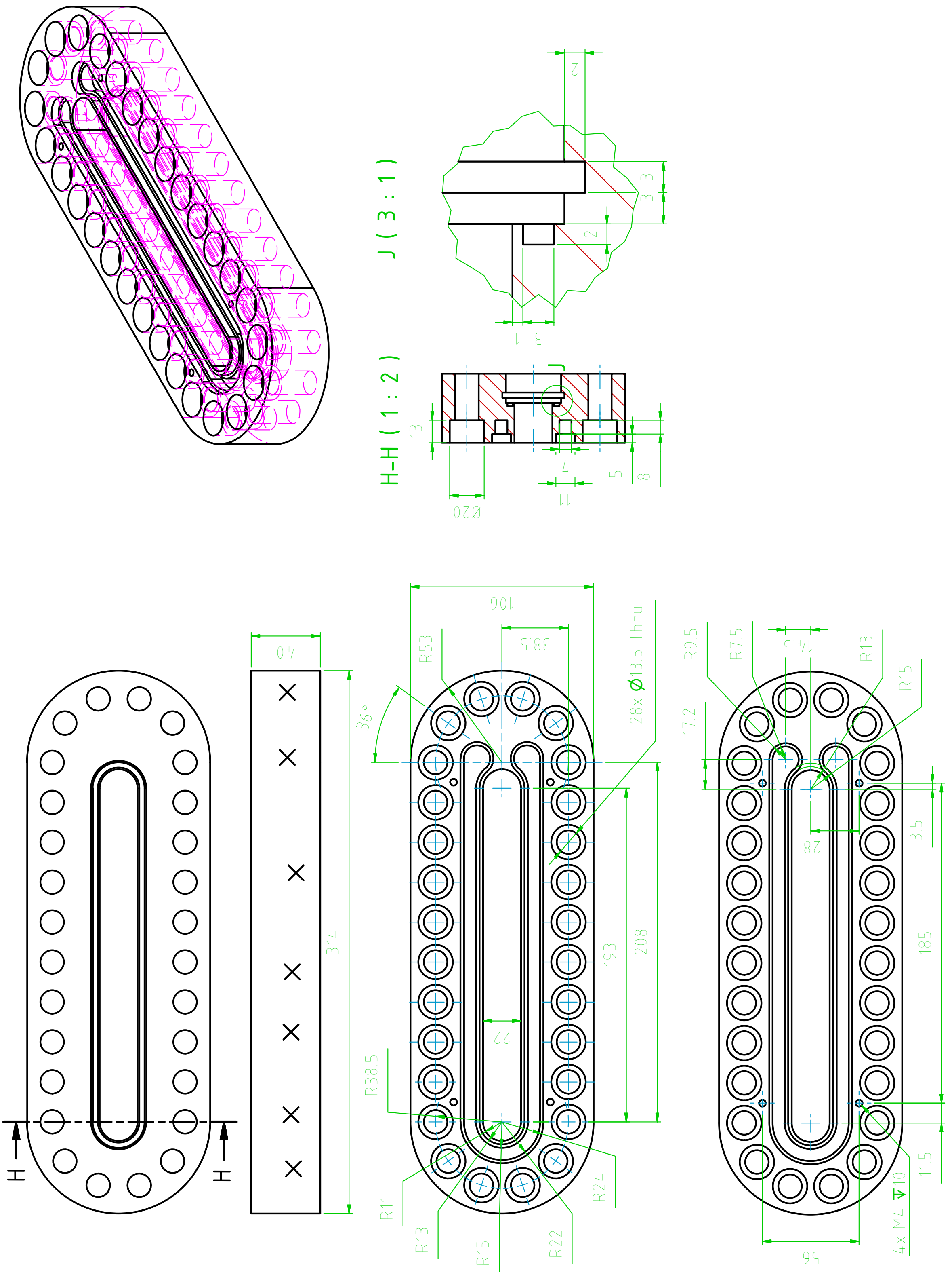
J (3 : 1)
2
3
3
2
1
3
H-H (1 : 2)
J
13
7
5
8
11
Ø20
106
38.5
R53
36°
28x Ø13.5 Thru
40
314
193
208
22
R38.5
R11
R13
R15
R22
R24
R9.5
R7.5
14.5
R13
R15
17.2
28
3.5
185
11.5
56
4x M4 ↧10
H
H

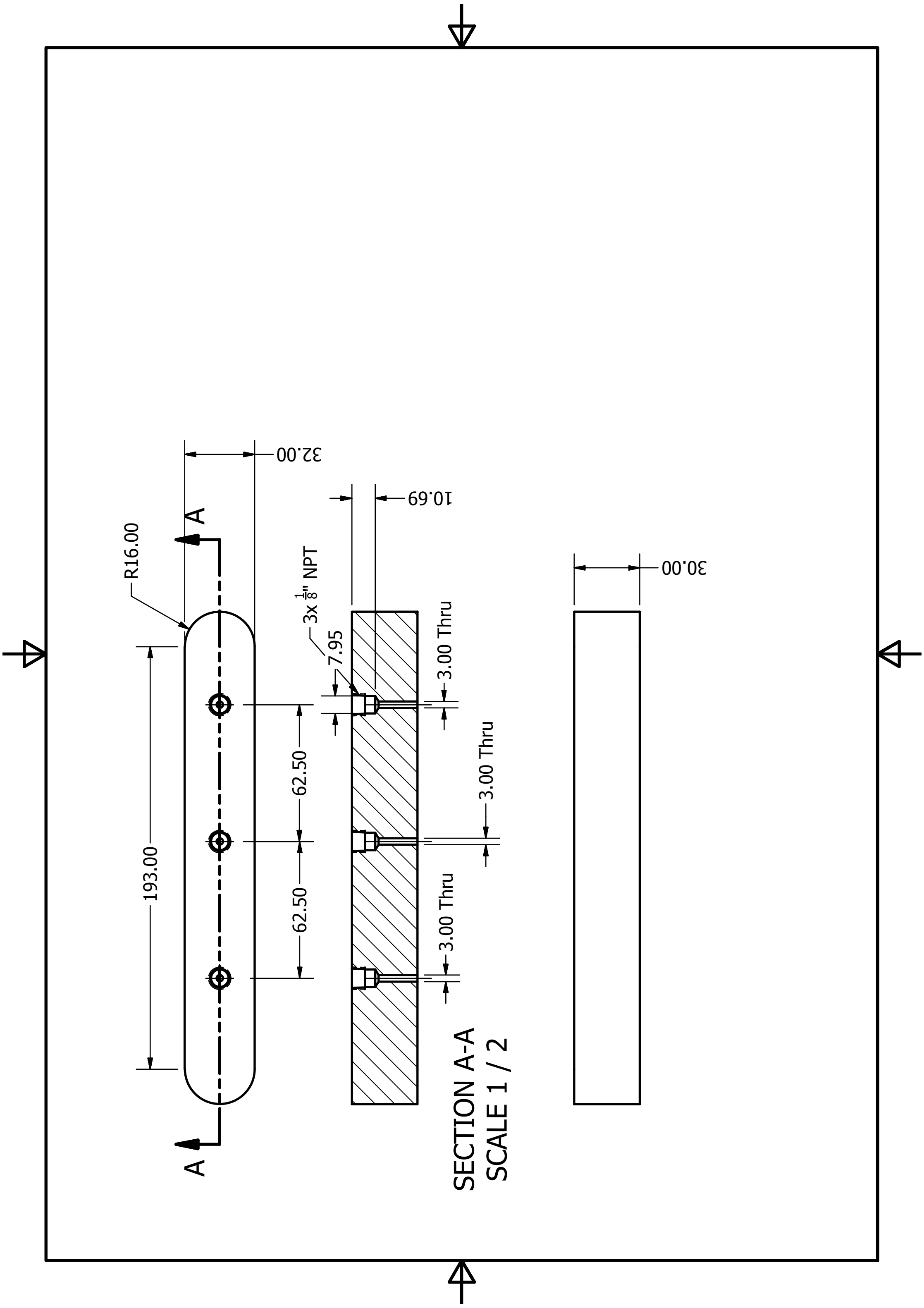
32.00
10.69
30.00
R16.00
A
A
3x $\frac{1}{8}$" NPT
7.95
3.00 Thru
3.00 Thru
3.00 Thru
62.50
62.50
193.00
SECTION A-A
SCALE 1 / 2

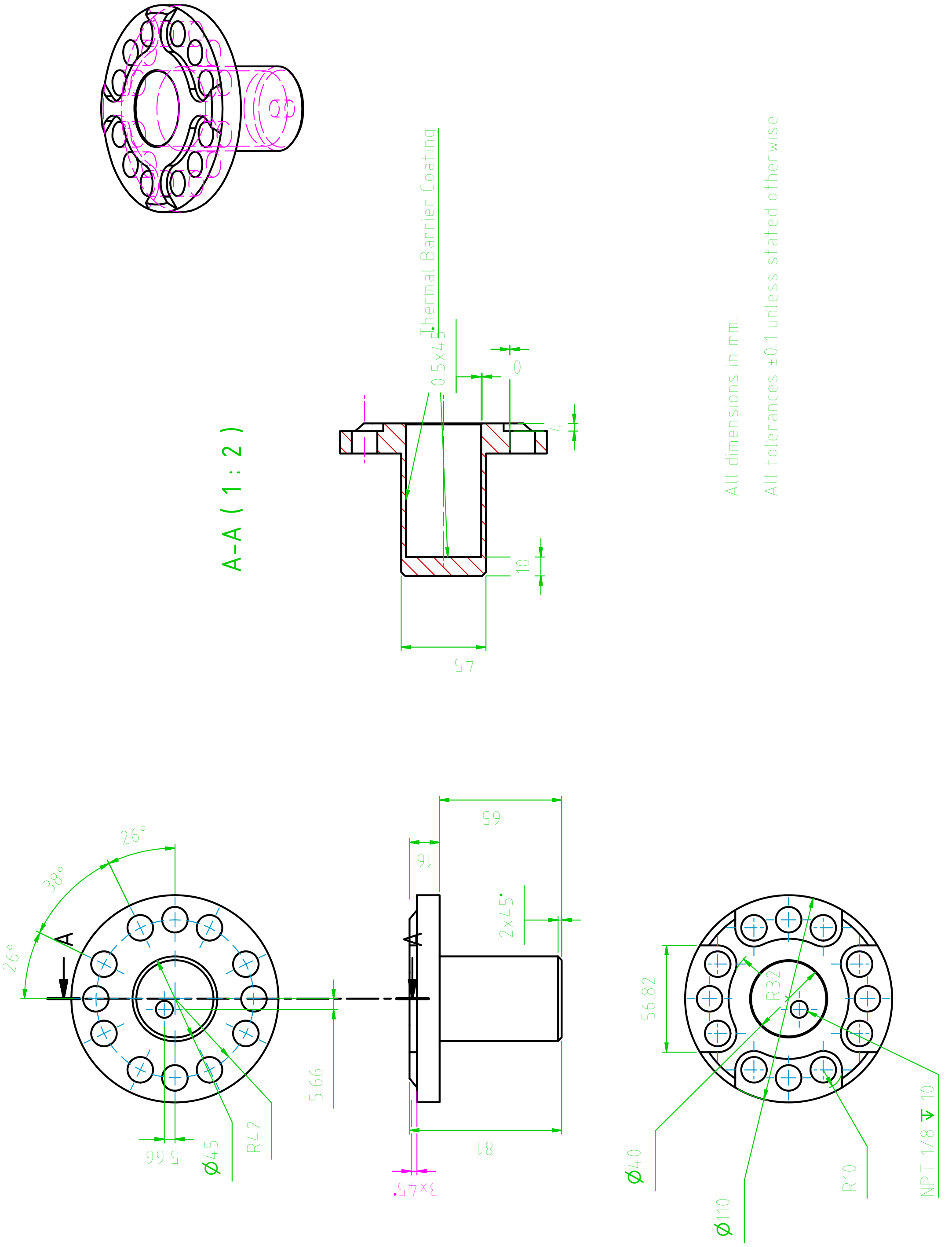
A-A (1 : 2)
Thermal Barrier Coating
0.5x45°
10
4
10
45
All dimensions in mm
All tolerances ±0.1 unless stated otherwise
26°
38°
26°
A
5.66
Ø45
R42
5.66
A
16
65
2x45°
81
3x45°
56.82
R32
Ø40
Ø110
R10
NPT 1/8 ⊽ 10

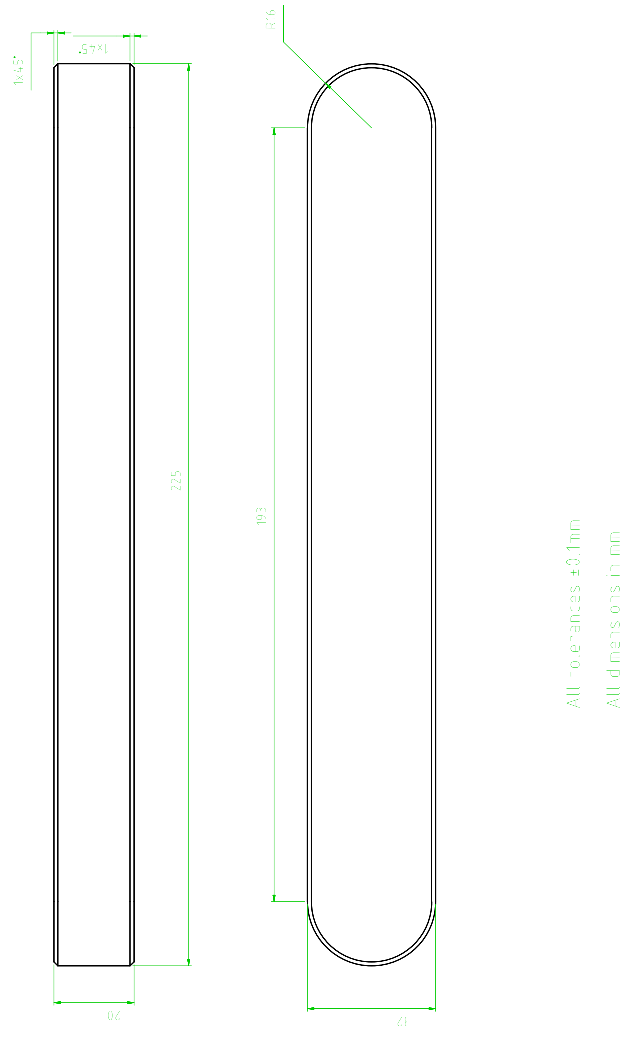
1x45°
1x45°
225
20
R16
193
32
All tolerances ±0.1mm
All dimensions in mm

Appendix C

PLIF Analysis code

```
%% Overview

% Written by Georgios Kasapis and Shangze Yang
% Last updated 01/12/2021
% Contact at s1450150@sms.ed.ac.uk

%% Sections


%% CLEAN

clear variables;close all; clc;

%% Core code

% Store code directory
code_directory = pwd;

% Load folder structure where data is saved
load('folderStructure.mat');

% False color (RGB MAP)
load('LIFColormap.mat','LIFColormap');

% Load the laser beam profile. This was taken from a ...
    different camera with
% different field of view. It therefore has to be ...
    subsequently truncated.
load('beam_profile_PIMAX.mat','beam_profile_PIMAX');

% Save number of test conditions
conditions = length(fieldnames(folderStructure));

% Save test conditions
testConditions = fieldnames(folderStructure);

% Loop over all test conditions
for i = 1: conditions

```

```
% Define number of experiments for given condition
experiments = length(folderStructure.(testConditions{i}...
).experimentDates);

% Loop over each experiment in each test condition
for j = 1:experiments

% Define the directory for where the data is stored
data_directory = strcat(code_directory, '\', ...
folderStructure.(testConditions{i}).name,...
'\', folderStructure.(testConditions{i}).experimentDates(j),...
'\Data and results');

% Define nozzle pixel locations stored in the folder structure
originX=folderStructure.(testConditions{i}).originX;
originY=folderStructure.(testConditions{i}).originY;

% Define the offsets from moving the chamber for Z1 and Z2
Z1offset=folderStructure.(testConditions{i}).Z1offset;
Z2offset=folderStructure.(testConditions{i}).Z2offset;

% Move directory to where data is kept
cd(data_directory)

% Create directory for saving data
write_directory = strcat(data_directory,'\Results\PI-MAX');

% Create structure that contains all background files
% with the extension *b.spe*
background_files = dir(fullfile(pwd,'*b.spe'));

% Create structure that contains all background files
% with the extension *m.spe*
measurement_files = dir(fullfile(pwd,'*m.spe'));

% Store the number of measurment files present in directory
number_of_measurements = length(measurement_files);

% Create empty vector to store background file names
[backgrounds, error] = prepareBackgrounds(background_files);

% Check if error occurred
if error == "Error occurred"
disp('Error occurred')
return
else % No problem
end

% Loop over number of measurements
for k = 1:number_of_measurements

% If measurement on axis, choose on axis background
if strcmp(measurement_files(k).name(22:23),'Y0') == 1
    background_name = backgrounds {1,1};
% If measurement off axis, choose off axis background
elseif strcmp(measurement_files(k).name(22:23),'Y1') == 1
```

```
    background_name = backgrounds {1,2};
else % Something wrong with license plate
    disp('Error in measurement file license plate')
    disp(['Error found in ' data_directory])
    disp(['Error concerns file ' measurement_files(k).name])
end

% Check that measurement file and background file gain are the
% same

if measurement_files(k).name(13:15) == background_name(13:15)
    % Camera gain matches. All good
else
    % Camera gain does not match. Throw error.
    disp('Measurement and background file gain do not match')
    return
end

% Store measurement name as cell data type
measurementcell{1,1} = measurement_files(k).name;
% Convert to characters
measurement_name = measurementcell{1,1};

% Go back to code_directory
cd(code_directory)

% Now measurement file and background file are chosen. Proceed
% with analyzing the data.
analyzePLIFdata(background_name, measurement_name,...
code_directory, data_directory,write_directory,originX,...
originY,Z1offset,Z2offset,LIFColormap,beam_profile_PIMAX)

end
end
end

%% Function to choose background files

function [backgrounds, error] = ...
   prepareBackgrounds(background_files)

% Check if there is a single, overall background or if there are
% two (one for jet-axis-centred measurements and one for off-axis
% measurements

backgrounds = {'',''};

% Single background file
if length(background_files)==1

% Assign the background name to both on axis and off axis
backgrounds{1,1} = background_files.name;
backgrounds{1,2} = background_files.name;
error = "No errors";

% Two background files. Choose based on Y location.
```

```
elseif length(background_files) == 2
if strcmp(background_files(1).name(22:23), 'Y0')==1
    % On axis background
    backgrounds{1,1} = background_files(1).name;
    % Off axis background
    backgrounds{1,2} = background_files(2).name;
    error = "No errors";

elseif strcmp(background_files(1).name(22:23),'Y1')==1
    % On axis background
    backgrounds{1,1} = background_files(2).name;
    % Off axis background
    backgrounds{1,2} = background_files(1).name;
    error = "No errors";
else % Something wrong with the file license plate
    disp('Error found in the bg file license plate')
    disp(['Error found in ' data_directory])
    error = "Error occurred";
end

else % Something wrong with the number of background files
disp('Incorrect number of background files')
disp(['Mistake found in ' data_directory])
error = "Error occurred";
end
end

%% Main function that analyzes the data

function analyzePLIFdata(background_name, measurement_name,...
code_directory, ...
    data_directory,write_directory,originX,originY,...
Z1offset,Z2offset,LIFColormap,beam_profile_PIMAX)

% Check if measurement is near nozzle. This is needed to ...
    choose figure
% formatting later on

if strcmp(measurement_name(20:21), 'Z0') == 1
% Near-nozzle measurement
near_nozzle = 1;
intensity_integral_cutoff = originY; % Nozzle tip
elseif strcmp(measurement_name(20:21), 'Z1') == 1
% Away from nozzle
near_nozzle = 2;
intensity_integral_cutoff=1;
else % must be a Z2 measurement
near_nozzle = 3;
intensity_integral_cutoff=1;
end

% Store camera gain
camera_gain = measurement_name(14:15);

% Store laser power
laser_power = measurement_name(32:35);
```

```

% Load data from background file
background=loadSPE(strcat(data_directory,'\',background_name));
% Rotate to correct orientation
background=rot90(background,3);

% Load data from measurement file
PLIF_images=loadSPE(strcat(data_directory,'\',measurement_name));
% Rotate to correct orientation
PLIF_images=rot90(PLIF_images,3);
% Get first background frame
PLIFbg=background(:,:,1);

% Store number of frames
[number_of_frames]=size(PLIF_images,3);

% Define name of new folder based on location that will be ...
    used to save the
% data
location_folder = measurement_name(20:23);

% Sometime multiple measurements are taken at same location. ...
    Differentiate
% between these based on liquid injection temperature
liquid_temp_folder = measurement_name(16:19);

% Change directory where analyzed data is to be saved
cd(write_directory);

%Check if folder was created in previous run
if ¬exist(location_folder, 'dir')
% If not create it now
mkdir(location_folder)
end

cd(location_folder);

%Check if folder was created in previous run
if ¬exist(liquid_temp_folder, 'dir')
% If not create it now
mkdir(liquid_temp_folder)
end

% Come back to code directory
cd (code_directory);

% Remove bottom part of profile as this is never illuminated ...
    by the laser
% source. 824 is the pixel index identified by looking at the ...
    PI-MAX image.
% Adjust accordingly if necessary.

% Update 21/02/2022 - Beam profile re-calculated. Useful data ...
    up to pixel
% 760. Hence, variable below goes to 760.

```

```
truncated_beam_profile(1:760,1) = beam_profile_PIMAX(1:760,1);

% Pixel index where correction from beam profile stops
intensity_integral_cutoff_2=length(truncated_beam_profile);

% Needed for upcoming loop
xlimit1=originX - 150;
xlimit2=originX+150;
ylimit1=1;
ylimit2=length(truncated_beam_profile);

originX = originX-xlimit1+1;
originY = originY-ylimit1+1;

PLIFfinal= ...
    zeros(ylimit2-ylimit1+1,xlimit2-xlimit1+1,number_of_frames);

% Loop over number of frames
for j=1:number_of_frames

% Store first frame
PLIF_original_frame=PLIF_images(:,:,j);

% Background subtraction
PLIFsignal=PLIF_original_frame-PLIFbg;

% Convert to double
PLIFsignal=double(PLIFsignal);

% Correct for beam profile, gain and laser power
PLIFsignal_corrected = ...
    applyCorrections(PLIFsignal,truncated_beam_profile,...
camera_gain,laser_power,xlimit1, xlimit2,...
intensity_integral_cutoff, intensity_integral_cutoff_2);

% Pre-allocate variable size
PLIFsignal_corrected_cropped = ...
    zeros(ylimit2-ylimit1+1,xlimit2-xlimit1+1);

% Select only necessary portion of image
for x=xlimit1:xlimit2
for y=ylimit1:ylimit2
    PLIFsignal_corrected_cropped(y-(ylimit1-1),x-(xlimit1-1))...
        =PLIFsignal_corrected(y,x);
end
end


% Store liquid injection temperature. License plate index 17 ...
    to 19
liquid_temperature=[measurement_name(17:19),'C'];

% Store the analyzed image
PLIFfinal(:,:,j)=PLIFsignal_corrected_cropped;

% Display image
```

```
imshow(PLIFsignal_corrected_cropped,[1,12000])

% Empty this variable so that it is redefined in the next loop
% iteration. (used to get an error if this was not done)
clear PLIFsignal_corrected_cropped

% Get figure handle to pass it on to the formatting function
current_figure = gcf;

% Call function to format current figure
formatCurrentFigure(current_figure,near_nozzle,...
        LIFColormap,liquid_temperature,originX,...
        originY,Z1offset,Z2offset)

% Capture the current axes as it appears on the screen as a movie
% frame. Fig is a structure containing the image data. getframe
% captures the axes at the same size that it appears on the ...
    screen.

Fig=getframe();

% Define save name for image
imagename=[num2str(j,'%0.3g'),'.jpg'];

% Change directory where analyzed data is to be saved
cd(strcat(write_directory ,'\', location_folder,...
'\', liquid_temp_folder));

%Save a single frame with all formatting
if j==1
saveas(current_figure,'Single_Frame_1.fig')
else
end

% Add frame to file
imwrite(Fig.cdata, imagename, 'quality', 100);

% Back to code
cd(code_directory)

end

% Compute average image
PLIFave=mean(PLIFfinal,3);

% Change directory where analyzed data is to be saved
cd(strcat(write_directory ,'\', location_folder,...
'\', liquid_temp_folder));

% Approximate limit of jet' edges (pixel indices)
left_limit=originX-5;
right_limit = originX+5;

% Calculate average intensity
LifSignal=mean(squeeze(PLIFave(:,left_limit:right_limit)),2);
StdIntensityAve=std(PLIFave(:,left_limit:right_limit),0,2);
```

```

% Save data in excel file
Average = LifSignal;
StandardDeviation=StdIntensityAve;
Table = table(Average, StandardDeviation);
datafile = "LIFcal.xlsx";
writetable(Table,datafile)

% LifSignal=flip(LifSignal);
% StdIntensityAve=flip(StdIntensityAve);

% Create string for saving average image
ave_name='ave.jpg';

% Display the image
imshow(PLIFave,[1,12000])

% Get figure handle to pass it on to the formatting function
current_figure = gcf;

% Call function to format current figure
formatCurrentFigure(current_figure,near_nozzle,...
        LIFColormap,liquid_temperature,originX,...
        originY,Z1offset,Z2offset)

% Save average image with all formatting
saveas(gcf,'Average_Image.fig')

Fig=getframe();

imwrite(Fig.cdata, ave_name, 'quality', 100);

video_name='Video';

Video=VideoWriter(video_name,'MPEG-4');

Video.FrameRate=2;

open(Video);

for movie=1: number_of_frames

moviename=[num2str(movie,'%0.3g'),'.jpg'];

I=imread(moviename);

writeVideo(Video,I);
end

close(Video);

end

function formatCurrentFigure(current_figure,near_nozzle,...
LIFColormap, liquid_temperature,originX,originY,...
Z1offset,Z2offset)
```

```

liquid_temperature = strcat('T_{fluid} =',liquid_temperature);

% Millimetres per pixel
spatial_resolution = 0.045;

% Maximize figure window to fullscreen size
current_figure.WindowState = 'maximized';

% Set figure colourmap
current_figure.Colormap = LIFColormap;

% Keep figure on for formatting
hold on

% Display x-axis and y-axis
axis on

% Format image based on the fact that the nozzle appears in the
% image plane
if near_nozzle == 1

ymarkers = [1,100,200,300,400,500,600,700,800,900,950];
ylabels = strings(1,length(ymarkers));
for i = 1:length(ymarkers)
    ylabels(1,i) =  num2str(round(((ymarkers(1,i)-originY).*...
    spatial_resolution),1));
end
yticks(ymarkers)
yticklabels(ylabels)

xmarkers = [1,100,200,300,400,500,600];
xlabels = strings(1,length(xmarkers));
for i = 1:length(xmarkers)
    xlabels(1,i) =  num2str(round(((xmarkers(1,i)-originX).*...
    spatial_resolution),1));
end
xticks(xmarkers)
xticklabels(xlabels)


% Plot various lines and texts
line([(originX-2),(originX+2)],[originY,originY],'color',...
'k','linewidth',3);
text ((originX), originY-15,'Nozzle ...
    tip','Color','black','FontSize',10);
ylabel('Distance from nozzle / mm')
xlabel('Distance from nozzle / mm')
text(1, 200,liquid_temperature,'Color','black','FontSize',10);

% Format the images differently
else

if near_nozzle==2
    zOffset= Z1offset;
else
```

```
    zOffset=Z2offset;
end

ymarkers = [1,100,200,300,400,500,600,700,800,900,950];
ylabels = strings(1,length(ymarkers));
for i = 1:length(ymarkers)
ylabels(1,i) =  ...
   num2str(round(((ymarkers(1,i).*spatial_resolution)+...
zOffset),1));
end
yticks(ymarkers)
yticklabels(ylabels)

xmarkers = [1,100,200,300,400,500,600];
xlabels = strings(1,length(xmarkers));
for i = 1:length(xmarkers)
xlabels(1,i) =  num2str(round(((xmarkers(1,i)-originX).*...
spatial_resolution),1));
end
xticks(xmarkers)
xticklabels(xlabels)

% Plot various lines and texts
ylabel('Distance from nozzle / mm')
xlabel('Distance from nozzle / mm')
text(1, 200,liquid_temperature,'Color','black','FontSize',10);
% Format the images differently if at Z2
end

hold off

current_figure.WindowState = 'minimized';

end
```

Appendix D

PELS Analysis code

```
%% Overview

% Written by Georgios Kasapis and Shangze Yang
% Last updated 26/10/2021
% Contact at s1450150@sms.ed.ac.uk

%% CLEAN
clear variables;close all; clc;

%% Main script

% Store code directory
code_directory = pwd;

% Load folder structure where data is saved
load('folderStructure.mat');

% Save number of test conditions
conditions = length(fieldnames(folderStructure));

% Save test conditions
testConditions = fieldnames(folderStructure);

% Loop over all test conditions
for i = 1: conditions

% Define number of experiments for given condition
experiments = length(folderStructure.(testConditions{i}...
).experimentDates);

% Loop over each experiment in each test condition
for j = 1:experiments

% Define the directory for where the data is stored
data_directory = strcat(code_directory, '\', ...
folderStructure.(testConditions{i}).name,...
'\', folderStructure.(testConditions{i}).experimentDates(j),...
'\Data and results');

```

```
% Move directory to where data is kept
cd(data_directory)

% Create directory for saving data
write_directory = strcat(data_directory,'\Results\Andor');

% Create structure that contains all background files
% with the extension *b.sif*
background_files = dir(fullfile(pwd,'*b.sif'));

% Create structure that contains all background files
% with the extension *m.sif*
measurement_files = dir(fullfile(pwd,'*m.sif'));

% Store the number of measurment files present in directory
number_of_measurements = length(measurement_files);

% Loop over number of measurements
for k = 1:number_of_measurements

% Characters at indeces 13:15 contain camera gain info
if measurement_files(k).name(13:15) == ...
    background_files(k).name(13:15)
% Camera gain matches. All good
else
% Camera gain does not match. Throw error.
disp('Measurement and background files do not match')
return
end

% Characters at indeces 20:21 contain location info
if measurement_files(k).name(20:21) == ...
    background_files(k).name(20:21)
% Location matches. All good
else
% Location does not match. Throw error.
disp('Measurement and background files do not match')
return
end

% Store measurement and background names
background_name = background_files(k).name;
measurement_name = measurement_files(k).name;

% Go back to code_directory
cd(code_directory)

% Now measurement file and background file are chosen. Proceed
% with analyzing the data.
analyzeESdata(background_name, measurement_name,...
code_directory, data_directory,write_directory)
end
end
end

%% Post processing data
```

```
function analyzeESdata(background_name, measurement_name,...
code_directory, data_directory,write_directory)

% Check if measurement is near nozzle. This is needed to ...
    choose figure
% formatting later on

if strcmp(measurement_name(20:21), 'Z0') == 1
% Near-nozzle measurement
near_nozzle = 1;
else
% Away from nozzle
near_nozzle = 0;
end

% Store camera gain
camera_gain = measurement_name(14:15);

% Store laser power
laser_power = measurement_name(32:35);

% False color (RGB MAP)
load('LIFColormap.mat','LIFColormap');

% Create file path and then convert to characters data type. ...
    This is needed
% for the function that opens '.sif' files.
file_path_background = strcat(data_directory, "\", ...
    background_name);
file_path_background = char(file_path_background);

% Define if program should read all, or headers only
atsif_setfileaccessmode(0);

% Attempt to open file located at the provided directory, and ...
    save the
% function return code
rc=atsif_readfromfile(file_path_background);

% Pre-allocate size of variable
All_Framesback = zeros(1024,1024,200);

% Check that the file has been succesfully loaded
if (rc == 22002)
% The enumeration corresponding to signal is the number 0. ...
    Set it here.
signal=0;
% Check that there is a signal present
[¬,present]=atsif_isdatasourcepresent(signal);
if present
% Retrieve number of frames
[¬,no_frames]=atsif_getnumberframes(signal);
%Check that there is at least one frame
if (no_frames > 0)
% Retrieve the size of each frame
[¬,size]=atsif_getframesize(signal);
```

```
% Get information of each sub-image in the .sif file
[¬,left,bottom,right,top,hBin,vBin]=atsif_getsubimageinfo(signal,0);
for i = 0: no_frames-1
[¬,data]=atsif_getframe(signal,i,size);
width = ((right - left)+1)/hBin;
height = ((top-bottom)+1)/vBin;
BCnewdata=reshape(data,width,height);
All_Framesback(:,:,i+1)= BCnewdata;
end
end
end
atsif_closefile;
else
disp('Could not load file.  ERROR - ');
disp(rc);
end

% Calculate averaged backgroundimage
Average_Imagebc = mean(All_Framesback,3);

% Define name of new folder based on location that will be ...
    used to save the
% data
location_folder = measurement_name(20:23);

% Sometimes multiple measurements are taken at same location. ...
    Differentiate
% between these based on liquid injection temperature
liquid_temp_folder = measurement_name(16:19);

% Change directory where analyzed data is to be saved
cd(write_directory);

%Check if folder was created in previous run
if ¬exist(location_folder, 'dir')
% If not create it now
mkdir(location_folder)
end

cd(location_folder);

%Check if folder was created in previous run
if ¬exist(liquid_temp_folder, 'dir')
% If not create it now
mkdir(liquid_temp_folder)
end


% % Create the new folders
% mkdir(location_folder); cd(location_folder); ...
    mkdir(liquid_temp_folder);

% Back to code directory
cd (code_directory);

% Load laser sheet intensity variation profile
```

```
load('beam_profile_andor.mat','beam_profile');

% % Normalize it so that it varies from 0 to 1
% beam_profile=mat2gray(beam_profile);

% Truncate intensity integral to avoid dividing by very small ...
    numbers
intensity_integral_cutoff = 110;

% Pixel index correspondng to window end (upper)
window_upper_limit = 280;

% Pixel index correspondng to window end (lower)
window_lower_limit = 840;

if near_nozzle ==1 % Near nozzle measurement
intensity_integral_cutoff_2 = 820; % Approximate nozzle tip pixel
else
intensity_integral_cutoff_2=940; % Cut-off a bit higher
end

% Not sure if the next line is necessary, but the Andor ...
    toolbox example
% sets it to 0
atsif_setfileaccessmode(0);

% Create file path and then convert to characters data type. ...
    This is needed
% for the function that opens '.sif' files.
file_path_measurement = ...
    strcat(data_directory,'\',measurement_name);
file_path_measurement = char(file_path_measurement);

% Attempt to open the file
Im=atsif_readfromfile(file_path_measurement);

% Check that the file has been succesfully loaded
if (Im == 22002)
% The enumeration corresponding to signal is the number 0. ...
    Set it here.
signal=0;
% Check that there is a signal present
[¬,present]=atsif_isdatasourcepresent(signal);
if present
% Retrieve number of frames
[¬,no_frames]=atsif_getnumberframes(signal);
%Check that there is at least one frame
if (no_frames > 0)
% Retrieve the size of each frame
[¬,size]=atsif_getframesize(signal);
% Get information of each sub-image in the .sif file
[¬,left,bottom,right,top,hBin,vBin]=atsif_getsubimageinfo(signal,0);
%xaxis=0;

All_ESimgBCLC = zeros(801,461,no_frames);

```

```
% Pre-allocate variable size
allIntensityAve = zeros(1024,no_frames-1);

for j = 0:no_frames-1
[¬,data]=atsif_getframe(signal,j,size);
width = ((right - left)+1)/hBin;
height = ((top-bottom)+1)/vBin;
ESimg=reshape(data,width,height);

% Subtract background
ESimgBC=ESimg-Average_Imagebc;

% Correct for beam_profile, laser power and camera
% gain
ESimgBCLC=applyCorrections(ESimgBC,beam_profile,...
camera_gain,laser_power,window_upper_limit,...
window_lower_limit,intensity_integral_cutoff,...
intensity_integral_cutoff_2);

% Rotate to correct orientation
ESimgBCLCR=rot90(ESimgBCLC);

% Pre-allocate variable size
CESimgBCLC = zeros(801,461);

% Save portion of image actually of interest
for y=300:760
for x=150:950
CESimgBCLC(x-149,y-299)=ESimgBCLCR(x,y);
end
end

% Collect final frame in 3d array of frames
All_ESimgBCLC(:,:,j+1)= CESimgBCLC;

cd(write_directory); cd(location_folder); cd(liquid_temp_folder);

imagename=[num2str(j+1,'%0.3g'),'.jpg'];

% Display image
imshow(CESimgBCLC,[1,2000])

% Get figure handle to pass it on to the formatting function
current_figure = gcf;

% Store liquid injection temperature. License plate index 17 ...
    to 19
liquid_temperature=[measurement_name(17:19),'C'];

% Call function to format current figure
formatCurrentFigure(current_figure,near_nozzle,...
LIFColormap,liquid_temperature)

% Capture frame information in a variable
Fig=getframe();

```

```
% Use that varible to save the frame
imwrite(Fig.cdata, imagename, 'quality', 100);

% Approximate limit of caustics' edges (pixel indices)
limit_one=500;
limit_two = 540;

% Calculate average intensity
IntensityAve= mean(ESimgBCLC(limit_one:limit_two,:));

% Take the inverse
CCIntensityAve=IntensityAve';

% Store it
allIntensityAve(:,j+1)=CCIntensityAve;
end

% Take total average and standard deviation and then flip
% vectors
AveIntensityAve=mean(allIntensityAve,2);
StdIntensityAve=std(allIntensityAve,0,2);
AveIntensityAve=flip(AveIntensityAve);
StdIntensityAve=flip(StdIntensityAve);

AveIntensityAveC = zeros(721,1);
StdIntensityAveC = zeros(721,1);

for q=180:900
AveIntensityAveC(q-179,1)=AveIntensityAve(q,1);
StdIntensityAveC(q-179,1)=StdIntensityAve(q,1);
end

AveESimgBCLC=mean(All_ESimgBCLC,3);

cd(write_directory); cd(location_folder); cd(liquid_temp_folder);

% Save data in excel file
Average = AveIntensityAveC;
StandardDeviation=StdIntensityAveC;
Table = table(Average, StandardDeviation);
datafile = "EScal.xlsx";
writetable(Table,datafile)

% Name for the averaged image
avename='ave.jpg';

% Display image
imshow(AveESimgBCLC,[1,2000])

% Get figure handle to pass it on to the formatting function
current_figure = gcf;

% Store liquid injection temperature. License plate index 17 ...
    to 19
liquid_temperature=[measurement_name(17:19),'C'];

```

```
% Call function to format current figure
formatCurrentFigure(current_figure,near_nozzle,...
LIFColormap,liquid_temperature)

Fig=getframe();

imwrite(Fig.cdata, avename, 'quality', 100);

%% Make video

video_name='Video';

Video=VideoWriter(video_name,'MPEG-4');

Video.FrameRate=2;

open(Video);

for movie=1:no_frames-1
moviename=[num2str(movie,'%0.3g'),'.jpg'];
I=imread(moviename);
writeVideo(Video,I);
end

close(Video);

cd(code_directory);
end
end
atsif_closefile;
else
disp('Could not load file. ERROR - ');
disp(Im);
end
end

%% Formatting current figure
function formatCurrentFigure(current_figure,near_nozzle,...
LIFColormap,liquid_temperature)

% Maximize figure window to fullscreen size
current_figure.WindowState = 'maximized';

% Set figure colourmap
current_figure.Colormap = LIFColormap;

% Keep figure on for formatting
hold on

% Format image based on the fact that the nozzle appears in the
% image plane
if near_nozzle == 1

% Plot various lines and texts
line([20,39],[50,50],'color','k','linewidth',2);
line([230,234],[40,40],'color','k','linewidth',3);
```

```
text(13, 35,'1 mm','Color','black','FontSize',10);
text (240, 30,'Nozzle tip','Color','black','FontSize',10);
text(1, 750,liquid_temperature,'Color','black','FontSize',14);

% Format the images differently
elseif near_nozzle == 0

% Plot various lines and texts
line([20,39],[50,50],'color','k','linewidth',2);
text(13, 35,'1 mm','Color','black','FontSize',10);
text(1, 750,liquid_temperature,'Color','black','FontSize',14);
end

hold off

current_figure.WindowState = 'minimized';

end

%% Correcting signal intensity
function [ESimgBCLC] = applyCorrections(ESimgBC,beam_profile,...
camera_gain,laser_power,window_upper_limit,...
window_lower_limit,intensity_integral_cutoff,...
intensity_integral_cutoff_2)

ESimgBCLC=ESimgBC;

% Apply beam profile correction
for p=window_upper_limit:window_lower_limit
ESimgBCLC(p,intensity_integral_cutoff:...
            intensity_integral_cutoff_2)=...
ESimgBCLC(p,intensity_integral_cutoff:...
            intensity_integral_cutoff_2)./...
beam_profile(intensity_integral_cutoff:...
             intensity_integral_cutoff_2);
end

% Baseline of laser power to be used for calculating correction
% factor.
laser_power_baseline = 600;

% Convert laser power to string and then to
laser_power=str2double(convertCharsToStrings(laser_power));

% Calculate laser power correction factor
laser_power_correction_factor = laser_power/laser_power_baseline;

% Remove effect of laser power variation
ESimgBCLC = ESimgBCLC./laser_power_correction_factor;

% Convert laser power to string and then to
camera_gain=str2double(convertCharsToStrings(camera_gain));

if camera_gain == 0
% no gain was used for the measurement. Hence, no correction.
else
```

```
% Gain was used. Correct for this
ESimgBCLC =ESimgBCLC./camera_gain;
end

end
```

Appendix E

FluidProp code

```
%% Clean up
clear variables; close all; clc;
%% Initialize FluidProp

%Call "Init_FluidProp" script to create COM server instance
Init_FluidProp

%% Define fluid mixture parameters and other quantities

% Specify model type
Model = "PCP-SAFT";

% Specify number of components
nCmp = 2;

% Specify components in text format, either full name or ...
    chemical formula
strComp1="nitrogen";
strComp2="Novec649";

% A separator is required. Use '-' for long names or ',' for ...
    formulae
separator=',';

% Concatenate strings to prepare full argument to be passed ...
    to the setfluid
% function
Comp = strcat(strComp1,separator,strComp2);

% Set number of points
n=100;

% Set number of equal concentration calculations
n_of_conc = 6;

% Pressure (bubble point) vector
P_bubble=ones(n_of_conc,n+1);

% Pressure (dew point) vector
```

```
P_dew=ones(n_of_conc,n+1);

% Create concentration array
Conc_array = ones(2,n_of_conc);

% Auxiliary variable to increment concentration
lowest_concentration = 0;
highest_concentration = 0.9;
conc_step = ...
    (highest_concentration-lowest_concentration)/(n_of_conc-1);

for j = 1 : n_of_conc
Conc_array(1,j)= lowest_concentration + (j-1)*conc_step;
Conc_array(2,j)= 1-Conc_array(1,j);
end

% Define range of temperatures
T = linspace(60,175,n+1);

% VLE is impossible after a certain concentration, depending ...
    on the
% mixture. Define a cutoff composition to keep steps and ...
    calculations in
% therelevant region. Value can vary from 0 to 1.

x_cutoff = 1;

% Mole fraction of component 1
x1 = linspace(0.1, x_cutoff,n+1);
% Mole fraction of component 2
x2 = 1-x1;


%% Perform bubble point and dew point calculations

for i =1:n_of_conc

%Prepare separate concentration array to pass as argument
Conc =[Conc_array(1,i),0;Conc_array(2,i),0];

% Define the working fluid each time with new composition
ErrorMsg = invoke(FP,'SetFluid_M',Model,nCmp,Comp,Conc);
if ¬ismember(ErrorMsg,{'No errors'})
disp('Invoke function failure')
%return
end
for j = 0:n

% Calculate bubble point pressure at constant composition, ...
    varying
% temperature and vapor quality 0
[P_bubble(i,j+1),ErrorMsg] = invoke(FP,'Pressure','Tq', ...
    T(j+1), 0);

% Calculate dew point pressure at constant temperature and ...
    vapor quality 1
```

```
% (vary only composition)
[P_dew(i,j+1),ErrorMsg] = invoke(FP,'Pressure','Tq', T(j+1), 1);

end
end

%% Determine index of critical point to exclude erroneous ...
    points when
%  plotting

% Determine critical pressure at each composition and take index

x_bubble=x1;
for i=1:n_of_conc
positive_counter =0;
for j = 1:n+1
if P_bubble(i,j)>0
positive_counter=positive_counter+1;
P_bubble_positive(i,positive_counter)=P_bubble(i,j);
T_bubble_positive(i,positive_counter)=T(j);
cut_off_index_bubble(i,1)=positive_counter;
else
end
end
end
positive_counter=0;
x_dew=x1;
for i=1:n_of_conc
positive_counter =0;
for j = 1:n+1
if P_dew(i,j)>0
positive_counter=positive_counter+1;
P_dew_positive(i,positive_counter)=P_dew(i,j);
T_dew_positive(i,positive_counter)=T(j);
cut_off_index_dew(i,1)=positive_counter;
else
end
end
end

%% Plot PT diagram

figure
hold on
grid on
legend on
string1='PT chart for';
string2 = strcat(string1, {' '}, Comp);
title(string2);

% P_bubble_positive(2,724:800)=0;
% cut_off_index_bubble(2) =723;

% for i=1:n_of_conc
% plot(T_bubble_positive(i,1:cut_off_index_bubble(i,1)),...
P_bubble_positive(i,1:cut_off_index_bubble(i,1)))
```

```
% plot(T_dew_positive(i,1:cut_off_index_dew(i,1)),...
P_dew_positive(i,1:cut_off_index_dew(i,1)))
% end

for i=1:n_of_conc
plot(T_bubble_positive(i,1:cut_off_index_bubble(i,1)),...
P_bubble_positive(i,1:cut_off_index_bubble(i,1)))
plot(T_dew_positive(i,1:cut_off_index_dew(i,1)),...
P_dew_positive(i,1:cut_off_index_dew(i,1)))
end

xlabel 'T / Celsius'
ylabel 'P / bar'
% ylim([0 10])
```